THE INFLUENCE OF PHYSICAL PROCESSES IN GALAXY CLUSTERS ON OBSERVABLE CLUSTER SCALING RELATIONS

BY

HSIANG-YI YANG

DISSERTATION

Submitted in partial fulfillment of the requirements
for the degree of Doctor of Philosophy in Astronomy
in the Graduate College of the
University of Illinois at Urbana-Champaign, 2011

Urbana, Illinois

Doctoral Committee:

Associate Professor Paul M. Ricker, Chair, Director of Research
Professor Charles Gammie
Associate Professor Brian Fields
Adjunct Professor Joseph Mohr

Abstract

Clusters of galaxies, which occupy a unique position in hierarchical structure formation, are invaluable cosmological probes and laboratories for astrophysical processes. Cluster scaling relations, which connect their masses and observable properties, provide the link between these two roles. Cosmological constraints derived from cluster abundances often rely on calibrations or functional forms of these relations. On the other hand, the form and evolution of the mass-observable relations are affected by astrophysical processes during cluster formation. Understanding these processes not only provides insights into cluster physics but also has important implications for cluster cosmology.

In this thesis, we use numerical simulations to study the influence of important physical mechanisms, including gravity, radiative cooling, and heating from active galactic nuclei (AGN), on cluster mass-observable relations. In particular, we investigate the physical origin of the intrinsic scatter around the best-fit relations by correlating it with measures of cluster structure, dynamical state, and AGN activity. Using a cosmological N-body plus hydrodynamic simulation produced using the FLASH code, we study the impact of cluster structure and dynamical state on the distribution of scatter in the X-ray temperature and Sunyaev-Zel'dovich (SZ) scaling relations. We also examine possible systematic biases in cluster cosmology, such as sample selection in cluster surveys, assumptions in self-calibration studies, and correlated errors in combining X-ray and SZ mass estimates.

Correctly simulating cluster properties, especially inside cluster cores, requires additional baryonic physics, including radiative cooling and some heating mechanisms such as AGN feedback. However, because of the extreme dynamic range required to capture the rich physics involved in accretion onto and feedback by the supermassive black holes (SMBH) in AGN, current modeling of AGN in cosmological simulations is highly phenomenological and relies on heterogeneous parameterizations. We perform a systematic sensitivity study on a variety of these models and parameters and quantify the current theoretical uncertainties in the predicted cluster global quantities. This study is an important step toward the development of more robust AGN models within a cosmological framework.

To my family.

Acknowledgments

I would like to express my gratitude to my advisor, Prof. Paul Ricker, for being my mentor both professionally and personally, for his constant guidance, support, kindness, patience, and encouragement.

I would like to thank Prof. Joe Mohr and Dr. Joanne Cohn for helpful discussions and their patience and friendly support for my job applications. I thank Prof. Charles Gammie and Prof. Brian Fields for helpful lectures and instructions. I am also grateful for Prof. You-Hua Chu, who has been supportive and taken care of me as a mother.

I thank my collaborators, Paul Sutter, Suman Bhattacharya, John Zuhone and Rene Fassbender for many insightful ideas, discussions, and contributions to this thesis work.

I would like to thank Jeeseon Song, my officemate and dearest friend, who is always supportive, understanding, and trustworthy that I can share any thoughts with. It is precious to have her friendship and companionship during my life in graduate school.

Thanks to Rosie Chen, Katherine Lee, Shiya Wang, Hsin-Fang Chiang, and Amy Lien for their fellowship that lightens up my days. Also thanks to our group members, Zarija Lukic, Chao-Chin Yang, Kuo-Chuan Pan, and Gary Foreman, for brainstorming and various suggestions, to Jeri Cochran, Sandie Osterbur, and Mary Margaret O'Connor for their assistance on administrative issues, and also to Salman Habib, Katrin Heitmann, Savvas Koushiappas, Min Sun, Douglas Rudd, Eric Hallman, August Evrard and many others for useful conversations, discussions, questions, and comments.

I am also grateful for being a part of the Vineyard small group, within the big family I have received a lot of friendship and love.

Finally, my lovely family, whose unconditional support, care, and love have been my main motivation. I am forever grateful for my parents, who are full of love, wisdom, generosity, and characters that I admire to. And Yen-Hsiang, my husband, my best friend, for sharing lifes, ups and downs, creative ideas, faiths, and passions. Without all of you I would not be able to experience the beautiful creation and love of God.

Table of Contents

List of Tables . . . . . **viii**

List of Figures . . . . . **ix**

List of Abbreviations . . . . . **xi**

List of Symbols . . . . . **xiii**

Chapter 1 Introduction **1**
1.1 Galaxy clusters 1
1.1.1 As cosmological probes 1
1.1.2 Mass-observable relations 4
1.1.3 Scatter in the scaling relations & systematics in cluster cosmology . . 7
1.2 Astrophysical processes in the intracluster medium 9
1.2.1 Gravitational - environment & mergers 9
1.2.2 Radiative cooling & stellar feedback 10
1.2.3 Feedback from active galactic nuclei 11
1.2.4 Other processes 11
1.3 Simulating cluster formation 12
1.3.1 Dark matter 13
1.3.2 Hydrodynamics 13
1.3.3 Radiative cooling, star formation and stellar feedback 14
1.3.4 Subgrid AGN models 15
1.3.5 The FLASH code 17
1.4 This work 18

Chapter 2 Influence of concentration and dynamical state on scatter in the X-ray temperature - mass relation **20**
2.1 Introduction 20
2.2 Cosmological simulation 22
2.2.1 Numerical methods 22
2.2.2 Simulation details 22
2.3 Analysis of the simulation 23
2.3.1 Merger tree analysis 23
2.3.2 Simulated X-ray observations 24

2.3.3 Substructure measures . . . 26
2.4 Results . . . 28
2.4.1 Distribution of intrinsic scatter . . . 29
2.4.2 Intrinsic scatter vs. halo concentration . . . 31
2.4.3 Intrinsic scatter vs. recent mergers . . . 36
2.5 Discussion . . . 41
2.5.1 Effect of dynamical state . . . 41
2.5.2 Effectiveness of substructure indicators . . . 42
2.5.3 Comparison with previous work . . . 45
2.6 Conclusions . . . 47

Chapter 3 Impact of structure and dynamical state on scatter in the SZ flux - mass relation . . . 50
3.1 Introduction . . . 50
3.2 Method . . . 53
3.2.1 Sunyaev-Zel'dovich effect . . . 53
3.2.2 Idealized Cluster Samples . . . 54
3.3 The Y–M scaling relation . . . 55
3.3.1 Normalization and Slope . . . 55
3.3.2 Scatter in the Y–M relation . . . 57
3.3.3 Non-lognormal scatter . . . 57
3.4 Sources of scatter . . . 60
3.4.1 Concentration . . . 60
3.4.2 Dynamical state . . . 64
3.4.3 Morphology . . . 66
3.4.4 Projection effects due to large-scale structure . . . 68
3.4.5 Insights from idealized samples . . . 68
3.5 Combining X-ray and SZ scaling relations . . . 69
3.6 Discussion and conclusions . . . 72

Chapter 4 Sensitivity test of AGN subgrid models . . . 75
4.1 Introduction . . . 75
4.2 Methodology . . . 77
4.2.1 Simulation setup . . . 77
4.2.2 AGN subgrid models . . . 77
4.2.3 Model and parameter variations . . . 81
4.3 Sensitivity study . . . 82
4.3.1 The fiducial run . . . 82
4.3.2 Numerical parameters . . . 86
4.3.3 Physical parameters . . . 89
4.4 Summary . . . 100

Chapter 5 Impact of AGN feedback on global ICM properties 102
5.1 Introduction 102
5.2 Robustness of integrated properties 103
5.2.1 Consistency with observations 103
5.2.2 Model uncertainties 104
5.3 Impact of AGN feedback on the scaling relations 108
5.3.1 Correlations between observables and AGN activity 108
5.3.2 Scatter in the L_X–T_X relation 110
5.4 Summary 112

Chapter 6 Conclusions 114

References 116

List of Tables

2.1 Best-fit parameters in the M–T_X relation. 29
2.2 Significant tests on scatter distributions for merging and relaxed clusters. . . 31
2.3 Significance tests after removing the effect of concentration. 41
2.4 Effectiveness of substructure measures. 46

3.1 Summary of models used for constructing the idealized cluster samples. . . . 55

4.1 Survey of numerical parameters in the bubble model. 82
4.2 Survey of numerical parameters in the jet model. 84
4.3 Survey of physical parameters. 85

5.1 Model uncertainties for observables measured within various overdensity radii. 106

List of Figures

1.1 Latest cosmological constraints from clusters. 3
1.2 Illustration of the Malmquist bias. 7

2.1 Comparison between emission-weighted and spectroscopic temperature. . . . 26
2.2 Simulated M–T_X relation. 28
2.3 Distributions of scatter for merging and relaxed clusters. 30
2.4 M–T_X scatter vs. concentration. 32
2.5 M–T_X scatter vs. formation time. 35
2.6 M–T_X relation corrected for concentration. 35
2.7 Distributions of concentration for merging and relaxed clusters. 36
2.8 M–T_X scatter vs. time since last merger. 38
2.9 Time history of a minor merger. 39
2.10 M–T_X scatter vs. substructure measures. 40
2.11 Distributions of scatter after correcting for concentration. 40
2.12 Time history of a major merger. 43
2.13 Effectiveness of substructure measures. 44

3.1 Normalization and slope of the Y–M relation. 56
3.2 Y–M scatter vs. cluster mass. 58
3.3 Non-gaussianity vs. limiting mass and redshift. 59
3.4 Y–M scatter vs. concentration and formation time. 60
3.5 Y–M relation before and after correcting for concentration. 63
3.6 Y–M scatter vs. dynamical state. 65
3.7 Distributions of scatter for merging and relaxed clusters. 66
3.8 Scatter vs. cluster morphology. 67
3.9 Scatter for idealized samples. 69
3.10 Study of correlated error between SZ and X-ray mass estimates. 71

4.1 Evolution for the fiducial run. 83
4.2 Resolution study for bubble and jet models. 87
4.3 Effects of jet sizes and radii for accretion and depletion. 88
4.4 Effects of accretion strength. 90
4.5 Effects of mechanical heating efficiency. 92
4.6 Effects of feedback frequency. 94
4.7 Effects of feedback region. 95

4.8 Effects of ratio between thermal and kinetic energy. 97
4.9 Comparison of the bubble and jet models. 98

5.1 Trajectories on the planes of scaling relations. 105
5.2 Model uncertainties in cluster integrated properties. 107
5.3 Evolution and correlations among AGN power and cluster observables. . . . 109
5.4 Correlations among observables. 110
5.5 Correlation between scatter and AGN power. 111
5.6 Correlation between scatter and cooling time. 112

List of Abbreviations

AGN	Active galactic nuclei
AMR	Adaptive mesh refinement
BAO	Baryon acoustic oscillation
BH	Black hole
BHAR	Black hole accretion rate
CC	Cool core
CDM	Cold dark matter
CMB	Cosmic microwave background
DES	Dark Energy Survey
ICM	Intracluster medium
FOF	Friends-of-friends
LOFAR	LO Frequency Array
LSST	Large Synoptic Survey Telescope
NFW	Navarro-Frenk-White
PPM	Piecewise-parabolic method
SDSS	Sloan Digital Sky Survey
SKA	Square Kilometer Array
SMBH	Supermassive black hole
SN	Supernova
SO	Spherical overdensity

SPH	Smoothed particle hydrodynamics
SPT	South Pole Telescope
SZ	Sunyaev-Zel'dovich
WMAP	Wilkinson Microwave Anisotropy Probe

List of Symbols

c	Speed of light
d_A	Angular diameter distance
h	Hubble parameter
k_B	Boltzmann constant
ρ	Density
p	Pressure
$M_\odot$	Solar mass
m_e	Electron mass
n_e	Electron number density
T	Temperature
z	Redshift

Chapter 1

Introduction

1.1 Galaxy clusters

1.1.1 As cosmological probes

The universe as we observe today, including the existence and structure of the cosmic microwave background (CMB) (e.g. Komatsu et al., 2011), the large scale structure of galaxies (e.g. Percival et al., 2001), and the accelerating expansion discovered by Type Ia supernovae measurements (e.g. Perlmutter et al., 1999), is well described by the *concordance* ΛCDM *model*, in which the universe started its expansion about 13 billion years ago and currently consists of roughly 70% dark energy, 20% non-relativistic cold dark matter (CDM), and 5% baryonic matter. In this framework, larger structures grow via gravitational instabilities from small initial perturbations in the density field. At the top of the hierarchy are clusters of galaxies, which are the largest virialized systems with masses around $10^{14} - 10^{15} \mathrm{M}_{\odot}$ and sizes of a few Mpc. Because they are massive and have just been detached from the cosmic expansion recently, a number of statistics, including their number counts (e.g. Mantz et al., 2010a), fraction of baryonic matter (e.g. Allen et al., 2008), and contribution to the high-multipole CMB power spectrum (e.g. Lueker et al., 2010), are excellent cosmological probes. Here we explain the logistics of cluster counting in more detail, since it is most relevant to this work.

Astrophysical structures tend to form from local maxima of the density field. When the amplitude of density perturbation reaches a critical value, a halo is born (see Cooray & Sheth (2002) for a review of halo model). In this picture, the number density of collapsed objects, $n(M, z)$, commonly referred to as the *mass function*, can be expressed in a differential function of mass

$$\frac{dn}{d\ln M} = \frac{\bar{\rho}_{\mathrm{m}}}{M} \left| \frac{d\ln\sigma}{d\ln M} \right| f(\sigma), \tag{1.1}$$

where $\bar{\rho}_{\mathrm{m}}$ is the comoving mean matter density and $f(\sigma)$ is a model-dependent function of

the variance of linearly-evolved CDM fluctuations,

$$\sigma^2(M,z) = \int \frac{d^2k}{(2\pi)^3} W^2(kR) P_{\rm m}(k,z), \tag{1.2}$$

filtered by a top-hat window function $W(y) = 3[\sin(y)/y^3 - \cos(y)/y^2]$ within radius $R = (3M/4\pi\rho_{crit})^{1/3}$, where $\rho_{crit} = 3H_0^2/8\pi G$ is the critical density of the universe. The cosmological parameter σ_8 measures the amplitude of perturbation with a conventional choice of $R = 8h^{-1}$Mpc. The matter power spectrum, $P_{\rm m}$, in the ΛCDM model is set by the present energy densities, $\Omega_X \equiv \rho_X/\rho_{crit}$, where X represents different components: 'b' for baryons, 'm' for matter, and 'DE' for dark energy. When the dark energy is a vacuum energy with equation of state $w = p/(\rho c^2) = -1$, Ω_Λ is used. For a given survey, the expected number of halos in a mass bin a and redshift bin i with solid angle $\Delta\Omega_i$ is

$$N(M_a, z_i) = \frac{\Delta\Omega_i}{4\pi} \int_{z_i}^{z_{i+1}} dz \frac{dV}{dz} \int_{\ln M_a}^{\ln M_{n+1}} d\ln M \frac{dn}{d\ln M}, \tag{1.3}$$

where the cosmological dependence comes in from the mass function and the volume element, dV/dz.

Analytical forms for $f(\sigma)$ were proposed (Press & Schechter, 1974; Sheth & Tormen, 1999); however, in order to capture the full non-linear growth of structures, numerical simulations have been used to provide a precise fit (Jenkins et al., 2001; Tinker et al., 2008). Thanks to advances in the computational power, the mass function now can be characterized with 5% statistical precision at $z = 0$ for a ΛCDM cosmology (Tinker et al., 2008). One subtlety to keep in mind is the definition of halo masses in the simulations. Two common conventions have emerged. The *friends-of-friends* (FOF) method identifies particles with separations smaller than a certain linking length, b, as friends, and then merges groups with shared friends. The *spherical overdensity* (SO) approach grows sphere around density peaks until the average enclosed density reaches a threshold, $\Delta\rho_{crit} = 3M(< r_\Delta)/(4\pi r_\Delta^3)$. Typical parameters adopted in the literature are $b = 0.2$ and $\Delta = 200$. Comparisons of these two approaches and choices of parameters are discussed in several studies (Cole & Lacey, 1996; Lukić et al., 2009; Knebe et al., 2011).

Mass determination for observations is another difficult task, since cluster masses are dominated by the invisible dark matter ($\sim 85\%$), while baryonic matter contributes to only $\sim 15\%$ in the form of hot, diffuse intracluster medium (ICM) (e.g. Allen et al., 2008) and $\sim 1\%$ in the stars (e.g. Lin & Mohr, 2004). Only for a fraction of clusters can the dark matter component be probed using gravitational lensing. In most cases the total mass can

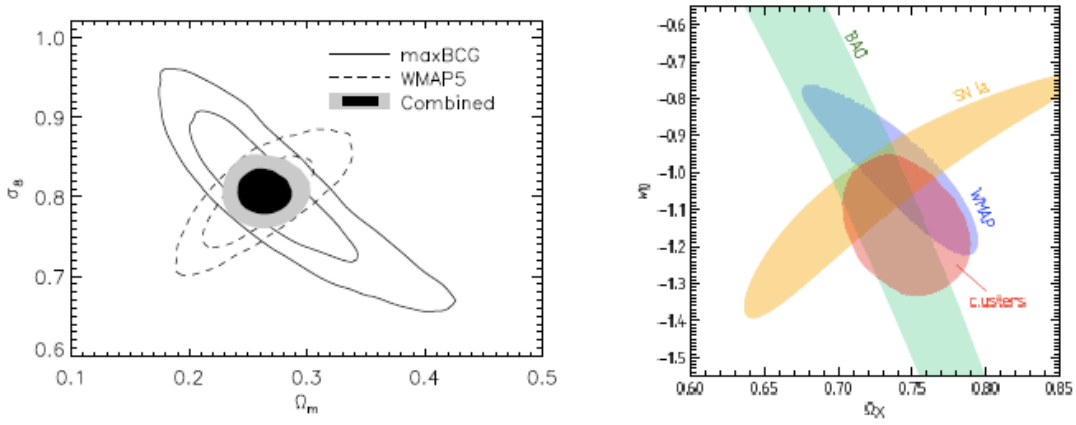

Figure 1.1: *Left*: Constraints for the mean matter density $\Omega_{\rm m}$ and the perturbation amplitude σ_8 from cluster abundance in the maxBCG sample compared with WMAP data for the ΛCDM model (Rozo et al., 2010). Right: Constraints on the dark energy density Ω_{DE} and equation of state w from clusters compared to WMAP, SNIa, and BAO for flat, constant w model (Vikhlinin et al., 2009).

only be inferred from some observable signals, such as starlight in optical and near-infrared, X-ray bremsstrahlung emission, or the thermal Sunyaev-Zel'dovich (SZ) effect (i.e. inverse Compton scattering of CMB photos by the ICM).

Fortunately, many integrated observable signals are found to correlate with cluster masses, including optical richness (e.g. Johnston et al., 2007), X-ray luminosity (e.g. Mantz et al., 2010a), X-ray temperature (e.g. Popesso et al., 2005), and the SZ decrement at mm wavelengths (e.g. Andersson et al., 2010). These empirical mass-observable relations can in principle be used to transform between distributions of observed signals and the mass function to derive cosmological constraints. However, these constraints are often subject to systematic biases in the calibrations of the scaling relations due to astrophysical uncertainties (see § 1.1.2 and also Borgani (2006) for a review).

An alternative approach is *self-calibration* (Majumdar & Mohr, 2004; Lima & Hu, 2004). The idea is to parametrize the scaling relations, including the mean, intrinsic scatter, and their evolution, and then fit them to the data to constrain these scaling relation parameters together with the cosmological parameters simultaneously. This method is especially powerful when large statistical samples of clusters are available. In fact, several recent studies have applied this technique to tens to hundreds of X-ray selected clusters (Mantz et al., 2010b; Vikhlinin et al., 2009) and roughly ten thousand optical-selected clusters (Rozo et al., 2010), and independently obtained constraints that are consistent with each other and also com-

petitive to other probes (see Figure 1.1). Existing and forthcoming cluster surveys at mm (SPT, ACT and Planck), optical (DES, LSST), and X-ray (eRosita) wavebands, are going to bring enormous data to further enhance the constraining power using clusters.

In order to achieve the promised precision of these large surveys, any systematics need to be carefully examined. For example, one important factor is to quantify the *selection function* of the observations. Failing to account for selection effects (e.g. Malmquist bias, see § 1.1.2) would bias the calibrations of scaling relations. Another key component is to properly parametrize the scaling relations in self-calibration studies. Tight cosmological constraints may arise from simplified but not necessarily physical assumptions about the scaling relations. On the other hand, allowing too many degrees of freedom for scaling relation parameters would yield uninteresting constraints. Therefore the efficacy of self-calibration demands the knowledge of the functional form of the *normalization, slope, intrinsic scatter*, and their *evolution*, which will need to be informed by theoretical models or numerical simulations. Common assumptions in the analyses to date are lognormal distribution of the scatter, and negligible evolution relative to the self-similar prediction (see § 1.1.2 for more detailed discussion). In this work we will explicitly examine the adequacy of these assumptions and possible systematics. Only when the systematics are fully understood can we maximize the merits of cluster cosmology.

1.1.2 Mass-observable relations

Despite the wish from the perspective of cosmology to consider clusters as simple 'spherical cows,' the formation of clusters actually involves various intricate physical mechanisms. Details in these processes are what shape the observable properties of clusters. Therefore one important question to ask is how well we understand the mass-observable relations. Here we will give a brief review.

The simplest model assumes cluster properties are governed by gravity alone and clusters are in virial equilibrium (Kaiser, 1986). Since gravity has no preferred scales, clusters are expected to be *self-similar*, i.e., clusters of different masses are just scaled version of each other and their mass is the only variable that determines the other properties. In the flat ΛCDM model, the critical density of the universe scales with redshift as $\rho_{crit}(z) = \rho_{crit,0}E^2(z)$, where

$$E(z) \equiv H(z)/H_0 = [(1+z)^3\Omega_{\rm m} + \Omega_\Lambda]^{1/2}, \tag{1.4}$$

given the evolution of the Hubble parameter $H(z)$. Together with the mass definition $M \propto \Delta\rho_{crit}(z)R^3$, the cluster size evolves as $R \propto M^{1/3}E^{-2/3}(z)$. Assuming cluster gas is heated and in equilibrium with the gravitational potential of the cluster, the virial theorem gives

$T \propto M/R$. Similar power-law relations can be derived for other thermodynamic quantities, such as the X-ray luminosity based on the assumption of bremsstrahlung emission, $L_X \propto n_e^2 T^{1/2} R^3$, the 'entropy' often invoked in cluster studies, $K \equiv T n_e^{-2/3}$ (Voit, 2005), and the integrated SZ decrement (Sunyaev & Zeldovich, 1972),

$$Y \equiv \int y d\Omega = \frac{1}{d_A^2(z)} \left(\frac{k_B \sigma_T}{m_e c^2} \right) \int n_e T_e dV. \tag{1.5}$$

Plugging in the dependences on mass and redshift, the self-similar scaling relations can be summarized as

$$M \propto T^{3/2} E^{-1}(z) \tag{1.6}$$

$$L_X \propto T^2 E(z) \tag{1.7}$$

$$K \propto T E^{-4/3}(z) \tag{1.8}$$

$$Y \propto M^{5/3} E^{2/3}(z). \tag{1.9}$$

The self-similar model is very instructive and agrees well with gravity-only hydrodynamic simulations (Bryan & Norman, 1998). However it is at variance with a number of observations. In particular, the observed relation between X-ray luminosity and temperature (e.g. Allen & Fabian, 1998; Osmond & Ponman, 2004; Pratt et al., 2009) is steeper and the measured level of gas entropy is higher than expected (e.g. Ponman et al., 2003), especially for poor clusters and groups. The discrepancies between observations and the gravity-only model are attributed to the need to consider additional sources of entropy in the ICM, which provide valuable implications on the cooling and heating mechanisms that govern galaxy formation.

Various models have been proposed to remedy the discrepancies, including ICM preheating and energy injection from supernovae (SN) or galactic winds, removal of low-entropy gas via radiative cooling, and some combination of these models (see Voit (2005) for a review). To date hydrodynamic simulations with cooling, star formation, and SN feedback have been shown to be able to reproduce the X-ray properties of the ICM outside the core regions (Borgani et al., 2004; Kay et al., 2007; Nagai et al., 2007a). Although they succeed in bringing model predictions closer to observations, some issues remain.

One common difficulty in the simulations is to regulate overcooling. Although radiative cooling is unimportant throughout most of the volume of a galaxy cluster, many clusters have such high central ICM densities that their cooling timescales are shorter than the Hubble time, the so-called *cool-core* (CC) clusters. In the absence of heating sources, the ICM gas

would lose its pressure support against gravity and slump inward as originally suggested by the cooling flow model (Fabian, 1994). Simulations with only radiative cooling thus produce great amounts of cold gas that are not observed in soft X-ray spectra (Peterson et al., 2003). Another consequence is that too large a stellar-to-gas fraction is predicted. While observations indicate that only about $\sim 10\%$ of the baryon content of a cluster is in the stellar phase (Dai et al., 2010), radiative simulations generally produce stars up to $\sim 50\%$ of the gas (Borgani et al., 2004; Nagai et al., 2007a).

Resolving all these issues requires the right amount of heating to balance radiative cooling. Feedback from active galactic nuclei (AGN) is the most popular candidate, as the observed power output from AGN seems to be sufficient to counteract radiative cooling losses (Dunn & Fabian, 2008), and it is potentially a self-regulating mechanism (Churazov et al., 2005). Considerable effort has been made toward investigating detailed mechanisms to heat the ICM efficiently in isolated cluster simulations; for example, hydrodynamic simulations (e.g. Churazov et al., 2001; Omma et al., 2004) have included more sophisticated treatments of turbulence (Scannapieco & Brüggen, 2008), viscosity (Reynolds et al., 2005) and magnetic fields (Brüggen & Kaiser, 2001; Robinson et al., 2004). Only recently has AGN feedback been included in the cosmological context using subgrid modeling (Sijacki et al., 2007; Booth & Schaye, 2009; Gaspari et al., 2011b; Dubois et al., 2010). Some of these simulations have successfully suppressed the stellar fraction to one third and matched the observed slope of the L_X–T_X relation (Puchwein et al., 2008).

However, so far these AGN subgrid models are highly phenomenological due to incomplete knowledge of the detailed accretion and feedback processes across scales from the supermassive black hole (SMBH) to the galaxy clusters. Besides, there has been a great diversity in the modeling details, but systematic parameter studies and comparisons among different models are lacking. In order for numerical simulations to provide meaningful information for observational calibrations, as mentioned in the previous section, the theoretical uncertainties in the modeling of AGN feedback must be addressed, as we will discuss in Chapter 5.

In summary, over the last decade there has been substantial improvement in the understanding of the mass-observable relations. Though modeling cluster cores is still a challenging subject, pursuit in this direction will provide invaluable information for both cluster astrophysics and cosmology.

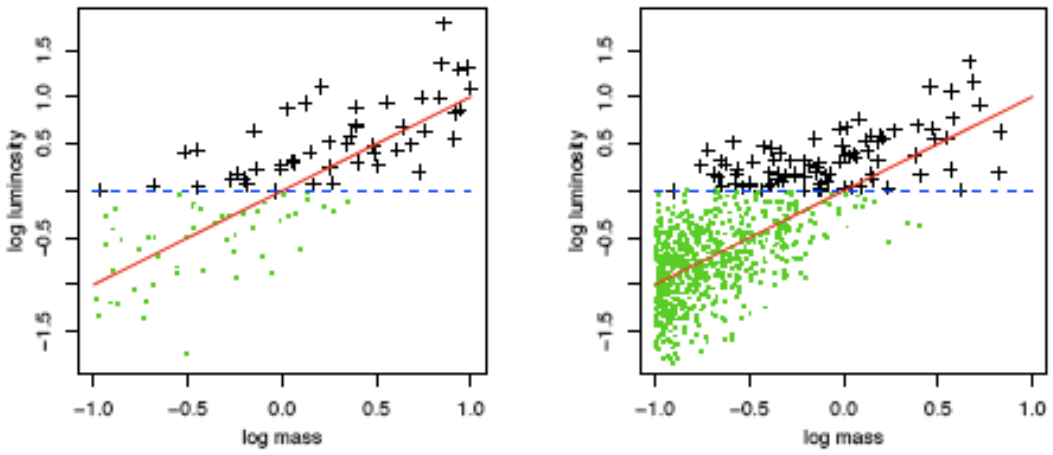

Figure 1.2: Illustration of the Malmquist bias resulting from the selection effects of a luminosity-limited observation, where the detected distribution (black) does not reflect the true scaling relations (red). The steepness of the mass function cause a even larger bias (right) compared to a unrealistic uniform distribution (left).

1.1.3 Scatter in the scaling relations & systematics in cluster cosmology

The empirical mass-observable relations indicate that clusters are fairly regular and close to equilibrium. However, understanding the systematics regarding not only the mean relations but also their *scatter* is crucial in cosmological studies. In this section we will emphasize the possible systematic biases that are caused by incomplete knowledge of the intrinsic scatter in the scaling relations.

The discrepancies between theory and observations in the mean relations have been alleviated by discoveries of several systematic effects. For example, masses determined under the common assumption of hydrostatic equilibrium in X-ray analyses in general underestimate the true mass by $\sim 20\%$ (Rasia et al., 2006; Nagai et al., 2007a). The emission-weighted temperature commonly used in numerical simulations is also found to be biased toward high values with respect to the X-ray spectroscopic temperature (Mazzotta et al., 2004; Rasia et al., 2005). Taking these two effects into account greatly resolves the mismatch in the normalization of the M–T_X relation. This underlines the importance of mock-observation tools to make direct comparison between results from numerical simulations and observational data. Since X-ray observables are the most well-studied mass proxies, in the investigation of X-ray scaling relations (Chapter § 2), we have created a tool to make mock Chandra X-ray images and extracted X-ray observables as if they were real observations.

The origin of scatter in these relations needs to be studied too. Due to the exponential slope of the mass function at high mass end, as the overall number of lower-mass clusters scattering to higher values of an observable 'O' far exceeds the number of high-mass clusters scattering in the opposite direction, significant scatter in the M–O relation would boost the number density of clusters observed in logarithmic bins of the observable O (also known as the *Eddington bias*). Underestimating this scatter can lead to an overestimate of σ_8, for instance.

Another observational bias associated with sample selections is the *Malmquist bias*, as illustrated in Figure 1.2. For a signal-limited survey (e.g. the luminosity threshold shown as the blue lines in this example), the observed scaling relation derived from the detected sample would be distorted from the true relation of the underlying distribution (red lines). The situation is even worse for a steepened mass function as in the realistic case (right panel). These biases have to be corrected in the analyses to recover the true scaling (Mantz et al., 2010a).

Efforts have been made to reduce the observed scatter to get better constraints on cluster masses. Such attempts include using core-excised quantities to remove the large dispersions inside cluster cores (O'Hara et al., 2006; Pratt et al., 2009; Mantz et al., 2010a) and the invention of the X-ray counterpart of the Compton-y parameter, $Y_X \equiv M_{gas}T_X$, to obtain a very tight $M - Y_X$ correlation (Kravtsov et al., 2006). These successful examples illustrate the possibility of obtaining better mass estimates if our knowledge of the physical origin of scatter is improved.

Even in the self-calibration technique (Majumdar & Mohr, 2004; Lima & Hu, 2004), where the scaling relations are fitted together with the cosmological parameters, the assumption of the functional form, mass and redshift dependence of the scatter in these relations can lead to misinterpretation of the obtained constraints (Lima & Hu, 2005). In particular, Shaw et al. (2010a) have shown that invalidity of the common assumption of lognormal scatter for an intrinsically non-lognormal distribution would cause a bias in the derived cosmological constraints.

Studying the physical sources of intrinsic scatter in the mass-observables relations can not only improve our understanding of cluster formation, but also help identify systematic uncertainties in cosmological studies. Therefore, the goal of our work is to use numerical simulations to examine the influence of cluster structure, dynamical state, radiative cooling, and AGN feedback on mass-observable relations and their scatter and evolution. We will give a brief review on the astrophysical processes in the ICM in § 1.2 and the numerical techniques for simulating cluster formation in § 1.3. We will then summarize the structure of this work in § 1.4.

1.2 Astrophysical processes in the intracluster medium

The observable properties of galaxy clusters are closely connected to the underlying physical processes in operation. As mentioned in § 1.1.2, the details in the ICM cannot be fully described by gravitational effects alone, but involve a complex of additional baryonic physics. This makes clusters not only powerful cosmological probes, but also great astrophysical laboratories. Since the goal of our work is to understand the influence of these mechanisms on cluster observables, here we will outline the important processes taking place in the ICM.

1.2.1 Gravitational - environment & mergers

In the hierarchical structure formation, objects form via a series of accretions and mergers of smaller building blocks. To the first order, the baryonic matter traces the evolution of the dark matter by gravitational attractions. Small dark matter halos first collapsed at the nodes of the filamentary structure of the cosmic web, then merge into bigger halos as the filaments accrete more matter. At the intersections of these filaments galaxy clusters are assembled, as seen in simulations of large scale structures (e.g. the Millennium Simulation (Springel et al., 2005)).

It is likely that the large-scale environment has left some imprints on the observable properties of clusters. For one, the filamentary structures, when aligned along the line of sight, may be confused with the signal from the cluster itself and cause a projection effect. Furthermore, internal structures of the dark matter halos also retain some memory of the surroundings. For example, the halos are not spherical, as treated in the analytical halo model, but mostly prolate (sometimes oblate or triaxial) (e.g. Shaw et al., 2006), which may have resulted from the surrounding tidal fields (e.g. Wang et al., 2011). Their spherically-averaged densities can be well approximated by a universal Navarro-Frenk-White (NFW) profile (Navarro et al., 1995)

$$\rho(r) = \frac{\rho_{crit}(z) A_c}{(r/r_s)(1 + r/r_s)^2}, \tag{1.10}$$

where r_s is the scale radius, $c \equiv r_{200}/r_s$ is the concentration parameter, and $A_c = 200c^3/3[\ln(1+c) - c/(1+c)]$. Tracking the assembly histories of halos in numerical simulations, Wechsler et al. (2002) find that the concentration parameter strongly correlates with the formation epoch.

Due to the large masses of clusters, the merger and accretion processes during their formation are particularly energetic. Strong gravitational pull can accelerate the collapsing

matter to $\sim 10^3$ km/s, generating shocks that convert tremendous amounts of energy into the thermal energy that heats the ICM. The Mach number of the shocks ranges from a few in the inner regions, to $10 - 1000$ at the edge of clusters where the low-density gas is cold (e.g. Pfrommer et al., 2006). A number of merger shocks have been detected with sensitive observations by the Chandra X-ray Observatory (see a review by Markevitch & Vikhlinin (2007)). The shocks and turbulence generated by mergers can drive clusters out of virial equilibrium as well as significantly affect their thermodynamic properties (Ricker & Sarazin, 2001; Poole et al., 2007).

1.2.2 Radiative cooling & stellar feedback

The baryons inside the halos are allowed to cool by radiation loss since the intracluster plasma is optically thin at most wavelengths. The cooling time for massive clusters is typically longer than the Hubble time, except a subset of clusters which have high-density cores in the inner $50 - 100$ kpc. These cool-core (CC) clusters are featured with high X-ray surface brightnesses and usually a temperature drop toward the center (Fabian, 1994). Cold gas implied by the ICM cooling rate far exceeds the observed limit by high-resolution X-ray spectroscopy (Peterson et al., 2003) (i.e. the 'cooling-flow' problem). Additionally, the observed scaling relations show self-similarity breaking due to excess entropy in lower-mass systems (as discussed in § 1.1.2). To match all the observed trends requires an intricate balance between cooling and some extra heating mechanisms.

One of the first proposed mechanisms is 'pre-heating' (Evrard & Henry, 1991), i.e., a significant injection of energy into the ICM at early times ($z > 1$), possibly by galactic winds or AGN. In this model, the gas entropy is elevated at high redshift *uniformly*, so lower-mass objects would be affected more than rich clusters, steepening the L_X–T_X relation as the increase in entropy reduces the density and X-ray emissivity. By adjusting the amount and redshift of the entropy injection, simulations with preheating have been able to match observed slopes of scaling relations (Bialek et al., 2001). However, large isentropic cores in smaller systems predicted by the preheating model disagree with observational data (e.g. Donahue et al., 2006). Moreover, observations of Lyα absorption lines in quasar spectra require that preheating cannot be global at $z > 2$ (Shang et al., 2007).

Another natural solution is star formation and feedback from supernovae (SN), as hinted by the metals detected in the ICM (Werner et al., 2008). Star formation resulting from gas cooling removes low-entropy gas from the hot phase so effectively raises the entropy level of the ICM (Voit & Bryan, 2001). Models including supernova-driven winds also helps to match the L_X–T_X slope (e.g. Borgani et al., 2004), although SN feedback alone cannot compensate

cooling with realistic heating efficiencies. Current simulations incorporating these two effects have brought significant improvements outside the cores (e.g. Nagai et al., 2007a). However, they are still insufficient to reproduce the detailed properties in the cool cores, such as the observed temperature decline, and the low stellar fractions (see Borgani & Kravtsov (2009) for a review).

1.2.3 Feedback from active galactic nuclei

Observational evidence has revealed that many galaxies in the local universe harbor supermassive black holes (SMBH) with masses $10^6 - 10^9$ $M_\odot$ at their centers (Ho, 1999). At redshifts as high as $z = 7$, these active galactic nuclei (AGN) hosting SMBH of mass $\sim 10^9$ $M_\odot$ already exist, as shown by Sloan Digital Sky Survey (SDSS) studies (Fan, 2006). The growth of SMBH occurs via mergers and accretion in galactic cores, and is believed to power the luminous quasars (Hopkins et al., 2005), as well as the relativistic jets observed in radio (e.g. Koide et al., 1999). The energetic input from SMBH can self-regulate its own growth (Di Matteo et al., 2005). Such feedback process is thought to be responsible for the observed correlation between the SMBH masses and host galaxies properties (e.g. stellar velocity dispersions) (Di Matteo et al., 2005), and also the size limits and star formation quenching in massive galaxies (Croton et al., 2006).

The AGN is one of the most promising solutions to the cooling flow problem for a few reasons. First, many observed X-ray cavities in the ICM are associated with radio-emitting medium from the relativistic jets of the SMBH (McNamara & Nulsen, 2007). The enormous jet power estimated from the enthalpy of these large 'bubbles' ($\sim 50 - 100$ kpc) is shown to be sufficient to offset cooling in many CC clusters (Dunn & Fabian, 2008). The AGN can also drive weak shocks and sound waves that carry significant amount of energy to heat cluster cores (e.g. McNamara et al., 2005; Fabian et al., 2006). Furthermore, observations find that large cavities are found only in clusters with short cooling times (Dunn & Fabian, 2008), strongly supporting the link between radiative cooling and AGN feedback.

1.2.4 Other processes

So far we have only considered the processes generating the thermal emission of the ICM. However, magnetic fields and cosmic rays are needed to explain the observed non-thermal diffuse and linear radio emissions (i.e. the radio 'halos' and 'relics', respectively). These non-thermal processes, though poorly understood, can potentially play a role in altering cluster observables. Although studying their effects is not the focus of this work (see Sutter (2011)

for investigation of magnetic fields), the relevant non-thermal effects are summarized here for completeness.

Magnetic fields in clusters have strengths of a few μG in general and sometimes up to $10 - 20$ μG in cluster cores, inferred from radio observations and rotation measures of background polarized sources. The fields appear to be tangled with auto-correlation lengths of 1-10 kpc (see Carilli & Taylor (2002) for a review). Magnetic fields can provide up to $0 - 20\%$ non-thermal pressure in the ICM (Dolag & Schindler, 2000). The cosmic rays also contribute to additional source of pressure support (Pfrommer et al., 2007). X-ray hydrostatic mass estimates may become biased if these non-thermal pressure components are not taken into account.

More importantly, the transport and dissipation processes in the ICM are closely related to the magnetic fields. In the absence of magnetic fields, the Coulomb mean free path is on the order of tens of kpc, making it incorrect to treat the ICM as a collisional fluid (see § 1.3.2 for more detailed discussion). But the mean free path can be greatly suppressed by the magnetic fields, at least orthogonal to the field lines. Consequently, anisotropic heat conduction and viscosity need to be considered, and their effective values may be suppressed, depending on the topology of magnetic fields.

If the viscosity of the ICM is non-negligible, it would provide extra entropy due to viscous dissipation during mergers and accretion, make ram pressure stripping of infalling galaxies more efficient, and change the morphology of the AGN-inflated bubbles (e.g. Reynolds et al., 2005). Heat conduction is another important transport process to consider. Many studies have shown that isotropic conduction is unlikely to be a stable heating source to overcome cooling since it requires fine-tuning (e.g. Conroy & Ostriker, 2008). Anisotropic conduction further worsen the situation, since it can rearrange the magnetic fields perpendicular to temperature gradients in the CC and shut down heat conduction into the cores completely, due to the heat-flux-driven buoyancy instability (HBI; Parrish & Quataert (2008)). The actual amplitude of these effects are all tied to the strength and configuration of the magnetic fields. More observational data from radio surveys (e.g. LOFAR, SKA) will be crucial to pin down the uncertainties.

1.3 Simulating cluster formation

Cosmological simulations of galaxy cluster formation are central to our work. We will summarize the numerical techniques employed for different components, including the dark matter (§ 1.3.1), hydrodynamics (§ 1.3.2), and AGN (§ 1.3.4). Finally, the simulation code *FLASH*

is introduced in § 1.3.5.

1.3.1 Dark matter

The dynamics of collisionless dark matter is described by the collisionless Boltzmann equation, which is the continuity equation of the phase space density in a six-dimensional space of coordinates and velocities. These equations can be integrated and simplified into a set of characteristic equations that are equivalent to the standard Newtonian equations of motions. In cosmological simulations the initial phase space is discretized and sampled by N particles (thus the name 'N-body') and their equations of motions are solved in a collective gravitational field.

The gravitational forces acting on the particles (and baryons) are computed in several different ways. Directly computing the force among each pair of particles is the most accurate, but also the most expensive as the number of operations scales as the square of number of particles. Alternative schemes include the particle-mesh method (Hockney & Eastwood, 1988), the tree method where forces are computed by multipole expansion (Barnes & Hut, 1986), or a hybrid of the two (Bagla, 2002). In the particle-mesh scheme, the particle densities are mapped onto a grid for solving the Poisson equations. The positions and velocities of particles are then updated using the force calculated by differencing the potential produced by the Poisson equations.

The dark matter particles are typically initialized on a uniform grid and given small perturbations of positions and velocities. Given the starting redshift of the simulation, the density perturbations are calculated by evolving the primordial Gaussian density field with power spectrum computed by an assumed cosmological model (e.g. CMBFAST, Seljak & Zaldarriaga (1996)) using the Zel'dovich approximation (Zel'Dovich, 1970).

1.3.2 Hydrodynamics

In cosmological simulations, the intracluster plasma are typically treated as an ideal fluid and thus solved by the hydrodynamic equations. One can ask whether the fluid approximation is applicable to the ICM. On the one hand, the Debye length in the ICM is short ($\lambda \sim 10^7$cm), so on resolvable scales in cosmological simulations ($\sim$ kpc), the plasma can be treated as a neutral, continuous field. On the other hand, the Coulomb mean free path in the absence of magnetic field is $\lambda \sim 23$ kpc$(T_e/10^8\mathrm{K})^2(n_e/10^{-3}\mathrm{cm}^{-3})^{-1}$ (Spitzer, 1962). For cluster outskirts, $T \sim 10^7$ K and $n_e \sim 10^{-4}\mathrm{cm}^{-3}$, the mean free path can be as large as ~ 100 kpc, which may pose a problem for the assumption of collisional gas. Fortunately, the magnetic

field observed in clusters (Carilli & Taylor, 2002), while being dynamically sub-dominant in most cases (Dolag et al., 2001), is likely to shorten the mean free path significantly, at least perpendicular to the field lines. Though the actual level of suppression is unclear (related to the topology of magnetic field lines), in general the hydrodynamic treatment is justified.

Numerical approaches of hydrodynamics can be divided into two categories: smoothed particle hydrodynamics (SPH; Lucy (1977)) and grid-based methods. In the SPH, fluid elements are represented by particles with a smoothing kernel, and the hydrodynamic equations are solved in the Lagrangian form. The main advantage of SPH is its Lagrangian nature so that the spatial resolution and geometry of the system are not limited by a grid. However, SPH has a limited ability to describe strong gradients. In addition, to prevent particles from penetrating shock regions, SPH introduced an artificial viscosity, which leads to suppression of shear motions and fluid instabilities.

On the other hand, grid-based codes, which solves the hydrodynamic variables defined on a grid by calculating fluxes at the cell boundaries, are shown to perform well in capturing shocks and contact discontinuities (Laney, 1998). Reaching high resolution with minimum computational costs is an issue for early Eulerian simulations using a uniform grid, until the adaptive mesh refinement (AMR) technique was developed to save resources by putting finer mesh only on regions of interest and keeping coarse meshes otherwise. Popular cosmological AMR codes include FLASH (Fryxell et al., 2000; Dubey et al., 2008), Enzo (O'Shea et al., 2004), and ART (Kravtsov et al., 1997).

Simulating clusters with SPH and AMR have been compared in the "Santa Barbara Comparison Project" (Frenk et al., 1999). Profiles of the ICM agree remarkably well outside cluster cores. In the core region, however, the entropy profiles have a flattened core in the AMR simulations, whereas for SPH the entropy continues to drop toward to center, owing to the suppression of mixing in SPH codes (Mitchell et al., 2009). By enhancement of the mixing in SPH simulations, such as decreasing the artificial viscosity (Dolag et al., 2005), or adding a dissipation term in the hydrodynamic equations (Wadsley et al., 2008), the predictions by SPH and grid-based Eulerian codes can be brought into better agreement.

1.3.3 Radiative cooling, star formation and stellar feedback

Radiative cooling (and other sources of thermal feedback) is included as a source term in the energy equation of hydrodynamics. At every timestep, the amount of energy radiated from each cell during that step is calculated and removed from the ICM gas. The cooling rates are calculated using local values of gas density, temperature, and metallicity using either a cooling model of ionized plasma or pre-calculated tables (e.g. FLASH interpolates cooling

rates from the tables of Sutherland & Dopita (1993)).

Since detailed processes of star formation from molecular clouds are not resolved with the maximum resolution in cosmological simulations ($\sim$ kpc), sub-resolution models are needed to treat star formation and stellar feedback. As stars form in the simulations, gas density is decreased and new collisionless star particles are created. The star formation rate is often parametrized as a power law function of the local gas density, such as the Schmidt law (Kennicutt, 1998). Note that any star particle in the simulation does not really represent a star but just a sample of the stellar distribution, just like dark matter particles in the simulations do not represent individual DM particles. Thus each star particle is treated as a population with mass distribution described by an initial mass function (IMF). SN feedback is modeled accordingly by assuming massive stars turn into supernovae and eject certain amounts of thermal energy and metals. The continuity equations for different species (e.g. hydrogen, helium and metals) are solved separately, and the abundances are used to compute the cooling rate self-consistently. Other types of feedback can also be implemented, such as UV heating, stellar winds, and secular mass loss by stars.

1.3.4 Subgrid AGN models

The accretion and feedback processes of the AGN are of great complexity in terms of physics and involve a dynamical range of $\sim 10^{10}$ from the accretion disks around the SMBH to galaxy clusters on Mpc scale. Cosmological simulations with AGN directly is thus beyond current computational power and must rely on sub-resolution modeling, which links the accretion and feedback on resolvable scales ($\sim$ kpc) to properties of the SMBH.

The modeling of accretion in cosmological simulations has commonly assumed the Bondi accretion rate (Bondi, 1952)

$$\dot{M}_{\rm Bondi} = 4\pi G^2 M_{\rm BH}^2 \rho / c_s^3, \tag{1.11}$$

where $M_{\rm BH}$ is the mass of the SMBH, ρ and c_s are the gas density and sound speed, respectively, estimated at the Bondi radius, $r_{\rm Bondi} = 2GM_{\rm BH}/c_s^2$. Because the Bondi radii are typically sub-kpc and not generally resolved in cosmological simulations, previous works have adopted a boosting factor (either a constant as in Sijacki et al. (2007) or density-dependent as in Booth & Schaye (2009)) in the above equation to account for the underestimation of accretion rates due to low resolution.

While the Bondi accretion rate appears sufficient in powering the observed AGN jets for many cases (Allen et al., 2006), for some systems other mechanisms seem to be required (McNamara et al., 2011). Furthermore, the original Bondi accretion rate is based on simplified assumptions such as spherical-symmetric, steady flow with zero velocities at the Bondi

radius. These criteria may not be applicable to all systems, especially those with radial infall due to rapid cooling, or with non-negligible angular momentum (e.g. Power et al., 2011). Alternative schemes have been proposed, including stochastic accretion (Pope, 2007), cold gas accretion (Pizzolato & Soker, 2005), accretion by gravitational instabilities in galaxies (Hopkins & Quataert, 2010), SMBH spins (McNamara et al., 2009), etc. These models are not yet integrated into cosmological simulations (except a cold-accretion-like scheme used in Gaspari et al. (2011b)). Clearly more detailed investigations and comparisons are necessary for further improvement in this area.

Motivated by the observed correlation between the jet power estimated from X-ray cavities and the Bondi accretion rate (Allen et al., 2006), it is generally assumed that a fixed fraction of the accreted rest mass energy goes into feedback in the surrounding ICM. Depending on the accretion rate in terms of the Eddington rate, $\dot{M}_{\rm Edd} = (4\pi G M_{\rm BH} m_{\rm p})/\epsilon_{\rm r}\sigma_T c$ ($\epsilon_{\rm r}$ is the radiative efficiency), the energy feedback from AGN may be radiatively efficient, like quasars at high redshifts, or mechanically efficient, as observed in clusters with X-ray bubbles (e.g. Churazov et al., 2005). The feedback energy is then thermally coupled to the surrounding gas with efficiencies motivated from observational constraints.

For mechanical feedback, one can either inject kinetic energy as bipolar jets (Cattaneo & Teyssier, 2007), or input thermal energy as already-inflated bubbles (Sijacki et al., 2007). Numerically, the jet simulations have higher resolution requirement, while it is easier to resolve the size of bubbles in cosmological simulations. Parameters required in the jet models are jet velocities, size and shape; for bubble models the frequencies, positions and sizes of bubbles need to be specified. Since there is a great degree of freedom in these models and few systematic comparisons have been done, we will present a detailed study to access how sensitive the subgrid models are to these different choices of models and parameters in Chapter 4.

These AGN subgrid prescriptions, which link the feedback energy to the accretion self-consistently, have been able to stabilize cooling and self-regulate black hole growth (e.g. Sijacki et al., 2007; Cattaneo & Teyssier, 2007). However, they are only meant to be phenomenological representations of AGN feedback and serve as the first step toward understanding the gross properties of the ICM. Generating realistic-looking bubbles in numerical simulations is still a challenge since it may involve additional baryonic processes, such as magnetic fields (e.g. Ruszkowski et al., 2007), subgrid turbulence (Brüggen et al., 2009), or cosmic rays (Guo & Mathews, 2011). Progress in the detailed interactions between AGN and the ICM will be very helpful in making a more realistic subgrid model of AGN feedback.

1.3.5 The FLASH code

The simulations in our work are performed using the AMR hydrodynamic plus N-body code, FLASH (Fryxell et al., 2000; Dubey et al., 2008). FLASH was originally developed by the Flash Center at University of Chicago to simulate thermonuclear flashes on compact objects and has been applied to a variety of fluid problems, as well as cosmological simulations, demonstrating excellent agreement with six other codes in an extensive cosmological code comparison project (Heitmann et al., 2005). FLASH is freely available and its modular framework allows users to easily adapt the code to specific problems.

The AMR feature of FLASH allows one to achieve very large dynamic ranges, optimal for cosmological simulations with AGN. The block-structured AMR package PARAMESH (MacNeice et al., 2000) develops the mesh hierarchy by bisecting blocks in each coordinate direction and placing blocks at nodes of a tree. In this 'oct-tree' method, the spatial resolution changes by a factor of two between any two adjacent levels. The user-defined refinement criteria can be either logarithmic density thresholds, often used in cosmological simulations, or second-order derivative of temperature, in order to capture shocks in hydrodynamical simulations.

The hydrodynamics module in FLASH solves the Euler equations of hydrodynamics using the piecewise-parabolic method (PPM; Colella & Woodward (1984)), which is an algorithm optimized for shock capturing. PPM achieves near second-order convergence by analytically solving Riemann's shock tube problem at each cell interface. The initial conditions for each shock problem are determined by averaging fluid quantities over characteristic domains in each cell using parabolic interpolants. For multidimensional problems, FLASH uses second-order operator splitting (Strang, 1968).

For collisionless components, such as dark matter, FLASH uses an N-body solver based on the particle-mesh method. The Poisson equation for the gravitational potential is solved using either a multipole solver, which is appropriate for nearly spherically symmetric problems with isolated boundary conditions, or a multigrid solver (Trottenberg et al., 2001) for more general problems. Multigrid methods solve elliptic equations by accelerating the convergence of relaxation methods. The new multigrid solver in FLASH3 uses a direct method based on the algorithm of Huang & Greengard (2000), modified to suit FLASH's oct-tree finite-volume mesh (Ricker, 2008).

1.4 This work

In Chapter 2, we present a study of the sources of intrinsic scatter in the X-ray temperature-mass relation by correlating it with quantities that are closely related to cluster formation and merging histories. The analyses are based on a cosmological hydrodynamics plus N-body simulation of galaxy cluster formation. We developed mock Chandra X-ray observations to obtain the X-ray spectroscopic temperature to facilitate direct comparisons with observations. To quantify the dynamical states of clusters, we built an algorithm to trace cluster merger histories to identify mergers, in addition to using observation-motivated substructure measures. A detailed comparison of merging clusters identified by substructure measures and by halo merger trees is given in the discussion. We find that, when cooling-related effects are neglected, the variation in halo concentrations is a more important factor for driving the intrinsic scatter in the M–T_X relation, while the combined effects of shock heating plus departures from hydrostatic equilibrium due to cluster mergers have a minor effect.

Chapter 3 extends the analyses to the Sunyaev-Zel'dovich (SZ) flux-mass (Y_{SZ}–M) relation. The functional form, evolution, and physical origin of the Y_{SZ}–M scatter are explored. We examine the assumption of lognormal scatter and detect non-negligible positive skewness and kurtosis (> 0.5) for a wide range of limiting masses and redshifts. These higher-order moments should be included in the parametrization of scatter in order not to bias cosmological constraints. We investigate the sources of scatter by correlating it with measures of cluster morphology, halo concentration, and dynamical state, and we quantify the individual contribution from each source. We find that statistically the impact of dynamical state is weak, so the selection bias due to mergers is negligible. On the other hand, there is a strong correlation between the scatter and halo concentration, which can be used to reduce the scatter significantly (from 12.07% to 7.34% or by $\sim 40\%$ for clusters at $z = 0$). We also show that a cross-calibration by combining information from X-ray followups can be used to reduce the scatter in the flux-mass relation and also identify outliers in both X-ray and SZ cluster surveys.

In Chapter 4, we begin the study of AGN feedback in the ICM. We implemented a subgrid AGN model in FLASH with several accretion and feedback models commonly used in the literature. Since detailed parameter studies and comparisons among these subgrid models are not available, we performed a sensitivity test on the AGN model with varied formulations and parameters, using hydrodynamical simulations within an idealized cluster atmosphere. The evolution of AGN activity and cluster profiles are compared for different numerical parameters (e.g. resolution) and physical parameters, including the strength of accretion, feedback efficiencies, duty cycles, regions of feedback, and the ratio of thermal to

kinetic energy. Among these variations, we find that the results are most sensitive to the choices of accretion strength, feedback efficiencies, and the sizes of feedback.

Chapter 5 takes the outputs from the sensitivity test and investigates the impact of AGN on global cluster properties (e.g. $M_{\rm gas}$, T_X, L_X, Y_{SZ} and Y_X). We first verify that all the model variations produce scaling relations that are consistent with current observational limits. Next, we quantify the theoretical uncertainties of each observable computed within R_{2500}, R_{1000}, R_{500}, and R_{200}, due to these model and parameter assumptions. We find that quantities that are related to gas densities, such as $M_{\rm gas}$ and L_X, are the most uncertain, whereas T_X, Y_{SZ} and Y_X are more robust. Finally, we show how the trajectories on the L_X–T_X relation correlate with the AGN activities.

Chapter 2

Influence of concentration and dynamical state on scatter in the X-ray temperature - mass relation[1]

2.1 Introduction

Galaxy clusters are potentially valuable cosmological probes because of their unique position in the hierarchy of structure formation. They are the largest gravitationally bound objects, having just separated from the cosmic expansion and collapsed from density fluctuations in the past few billion years. Therefore, statistical measures of clusters, such as their mass distribution as a function of redshift, are sensitive to the cosmic matter density parameter Ω_m, the dark energy density parameter Ω_{de}, the normalization of the primordial fluctuation spectrum σ_8, and the dark energy equation of state parameter w (Haiman et al., 2005). Future cluster surveys will yield cosmological parameter constraints that are complementary to those from upcoming microwave background probes (e.g. Planck) and Type Ia supernova observations.

However, clusters present us with a dilemma: their masses are well-predicted by numerical simulations, but in the real world, 80–85% of their mass is in the form of invisible dark matter. In order to make contact with observations, observational mass proxies are needed. Fortunately, cluster masses correlate with many observable quantities, such as X-ray temperature T_X, X-ray luminosity L_X, optical richness, infrared luminosity, and the Sunyaev-Zel'dovich effect (Mohr et al., 1999; Lin et al., 2003; Popesso et al., 2005; Hansen et al., 2005; Stanek et al., 2006). These mass-observable relations indicate that clusters are fairly regular and close to equilibrium, despite having dynamical timescales of order 1/10 the age of the universe.

For clusters to provide meaningful constraints on the cosmological parameters, the systematic errors in mass estimates based on these relations must be well-understood. For example, masses determined under the assumption of hydrostatic equilibrium in general underestimate the spherical overdensity mass M_{200} by $\sim 20\%$ (Nagai et al., 2007b). The X-ray temperature determined through spectral fitting is also known to bias low with respect to

[1]This chapter is previously published in the Astrophysical Journal as Yang, H.-Y. K., Ricker, P. M., & Sutter, P. M. 2009, ApJ, 699, 315.

the emission-weighted temperature commonly used in numerical simulations (Rasia et al., 2005). The discrepancy in the normalization of the M–T_X relation between observations and numerical simulations has been alleviated only recently by taking these two effects into account. This emphasizes the importance of using mock-observation tools to make direct comparisons between results from numerical simulations and observational data.

The origin and distribution of scatter in these relations are also important. Due to the exponential shape of the mass function, scatter in the M–X relation (for observable X) boosts the number density of clusters observed in logarithmic bins of X, as the overall number of lower-mass clusters scattering to higher values of X far exceeds the number of high-mass clusters scattering in the opposite direction. Underestimating this scatter can lead to an overestimate of σ_8, for instance (Randall et al., 2002). Attempts have been made to reduce the observed scatter to get better constraints on cluster masses. Such attempts include the use of core-excised quantities to reduce the large scatter in the L_X–T_X relation due to the effects of cool cores (Allen & Fabian, 1998; O'Hara et al., 2006) and the invention of the X-ray counterpart of the Compton y-parameter, $Y_X \equiv M_{\rm gas}T_X$, to obtain a very tight M–Y_X correlation (Kravtsov et al., 2006). These successful examples illustrate the possibility of obtaining better mass estimates if our knowledge of the physical origin of scatter is improved. It is also possible to self-calibrate cluster surveys (Levine et al., 2002; Majumdar & Mohr, 2004; Lima & Hu, 2004), fitting the mass-observable relation as an unknown together with the cosmological parameters. However, this technique requires assumptions about the functional form and the mass and redshift dependence of the scatter, and errors in these assumptions can lead to misinterpretation of the obtained constraints (Lima & Hu, 2005).

In this work we begin a systematic study of the influence of internal cluster physics on the scatter in cluster mass-observable relations. We focus initially on X-ray observables, as they are less directly dependent on the uncertain details of galaxy formation than, for example, optical observables. Our aim in this study is to examine the effects of mergers and dynamical state in isolation from effects due to radiative cooling, feedback due to stars and black holes, and diffusive transport. Future papers will examine these other effects separately. Accordingly, the simulation described here includes only dark matter and gasdynamics. While we examine substructure-based measures of dynamical state to make contact with previous work, we extend this work by considering direct measurements of dynamical state that may not be observable but that can give us physical insight into the origin and form of the scatter. For example, we use halo merger histories derived from halo catalogs created every $100h^{-1}$ Myr to identify which clusters are merging at any given epoch. § 2.2 describes our numerical methods and simulation parameters. In § 2.3 we describe our merger tree and virial analysis procedures, our method for generating simulated X-ray observations, and the substructure

measures we employ. We present our results in § 2.4 and discuss them in § 2.5. Finally, we summarize our conclusions in § 3.6.

Throughout this study we have taken the Hubble constant to be $H_0 = 100h$ km s^{-1} Mpc^{-1}, with $h = 0.708$. When quoting masses or radii defined using an overdensity criterion (e.g., M_{200}, R_{200}), we refer to overdensities relative to the critical density at the relevant epoch.

2.2 Cosmological simulation

2.2.1 Numerical methods

The simulation described here was performed using FLASH, an Eulerian hydrodynamics plus N-body code originally developed for simulations of Type Ia supernovae and related phenomena (Fryxell et al., 2000). The flexibility of FLASH's application framework has enabled it to be applied to a wide range of problems. In the process it has been extensively validated, both for hydrodynamical (Calder et al., 2002) and cosmological N-body (Heitmann et al., 2005, 2008) applications. We used version 2.4 of FLASH together with the local transform-based multigrid Poisson solver described by Ricker (2008). The Euler equations describing the behavior of the intracluster medium (ICM) were solved using the Piecewise-Parabolic Method (PPM); extensive details of the FLASH implementation of PPM are given by Fryxell et al. (2000). The N-body component describing the behavior of the dark matter was handled using the particle-mesh technique with cloud-in-cell interpolation. Because we are concerned in this study only with the effect of gravity-driven variations in dynamical state on mass-observable relations, the calculation described here did not employ radiative cooling or feedback due to star formation or active galaxies.

2.2.2 Simulation details

The results presented here are based on a FLASH simulation of structure formation in the ΛCDM cosmology within a 3D cubical volume spanning $256h^{-1}$ Mpc. Initial conditions were generated for a starting redshift z of 66 using GRAFIC (Bertschinger, 2001) with an initial power spectrum generated using CMBFAST (Seljak & Zaldarriaga, 1996). The cosmological parameter values used were chosen to be consistent with the third-year WMAP results (Spergel et al., 2007): present-day matter density parameter $\Omega_{m0} = 0.262$, present-day baryonic density parameter $\Omega_{b0} = 0.0437$, present-day cosmological constant density parameter $\Omega_{\Lambda 0} = 0.738$, and matter power spectrum normalization $\sigma_8 = 0.74$. The simulation contains 1024^3 dark matter particles with a particle mass $m_p = 9.2 \times 10^8 h^{-1} M_\odot$. The mesh used for

the gasdynamics and potential solution was fully refined to 1024^3 zones, which corresponds to a zone spacing of $250h^{-1}$ kpc. Considering the effect of resolution on the computed abundances of halos of different mass (Lukić et al., 2007), with these parameters we are able to capture all halos containing more than 3150 particles (i.e. total mass $2.9 \times 10^{12}h^{-1}M_{\odot}$) and 1150 particles (i.e. $1.1 \times 10^{12}h^{-1}M_{\odot}$) at $z = 0$ and $z = 1$, respectively. The halos are identified using the friends-of-friends (FOF) algorithm. The overdensity mass and radius, M_{Δ} and R_{Δ}, are then found by growing spheres around each FOF center until the averaged total density is Δ times the critical density of the universe.

The simulation was carried out using 800 processors of the Cray XT4 system at Oak Ridge National Laboratory, requiring a total of 16,500 CPU-hours. Gas and particle snapshots were written to disk every $100h^{-1}$ Myr beginning at $z = 2$, yielding a total of 117 snapshots containing 15 TB of data.

2.3 Analysis of the simulation

2.3.1 Merger tree analysis

In order to directly quantify the dynamical state of clusters without relying on morphology, we generate merger trees for each cluster in our simulation and find the time since last merger. Here we summarize how the merger trees are extracted.

First, our simulation generates output files that contain particle tags and positions every $100h^{-1}$ Myr between $z = 2$ and $z = 0$. We run a FOF halo finder with linking length parameter $b = 0.2$ on the particle positions to find all the groups containing more than 10 particles. Although some of the very small groups are under our halo completeness limit, they have little effect on our results because we only look at minor or major mergers for which the mass of the smaller object is above our completeness limit. Thus all mergers for the objects we study are being counted. Between successive outputs at times $t = t_n$, we find the progenitors at time t_{n-1} for all the halos at t_n by tracing the particle tags, which are uniquely assigned to each particle in the beginning of the simulation. A halo A is identified as a progenitor of another halo B if A contains at least one particle that is also in B. For each halo we record the masses of its progenitors, their contributed masses, and the number of unbound particles. Then the merger trees are constructed by linking all the progenitors identified in the previous outputs for halos above our halo completeness limit at $z = 0$. Deriving the mass accretion histories is straightforwardly accomplished by following the mass of the most massive progenitor back in time.

To find the time since last merger for any given halo, we need to define what a 'merger' is.

There are many different ways to define mergers in cosmological simulations. In our analysis we adopt two definitions: the mass-jump definition, in which a merger is present if there is a mass jump in the halo's assembly history; and the mass-ratio definition, which identifies a merger if the ratio of contributed masses from the first- and second-ranked progenitors is less than a certain value (Cohn & White, 2005). To study the variations in cluster observables induced by different types of mergers, we use 1.2 and 1.33 as thresholds for the mass-jump definition and 10:1, 5:1, and 3:1 in the mass-ratio definition. For each of the five criteria, the time since last merger is found for all clusters at $z = 0$ and $z = 1$.

In the later discussions we refer by 'merging clusters' at a given lookback time to those identified by at least one of the five merger diagnostics in the preceding 3 Gyrs, the typical time for clusters to return to virial equilibrium within R_{500} (Poole et al., 2006). The mergers are 'major' if the mass jump is larger than 1.2 or if the mass ratio is less than 5:1; 'minor' mergers, on the other hand, have mass ratios between 10:1 and 5:1.

2.3.2 Simulated X-ray observations

The observational X-ray temperature of the ICM, T_X, usually refers to the spectroscopic temperature, obtained by fitting a single-temperature model to the integrated cluster spectrum. Using simulation-based temperature proxies, such as emission-weighted temperature, has been shown to overestimate T_X (Mathiesen & Evrard, 2001; Rasia et al., 2005). To directly compare simulated cluster properties with observations, we create mock Chandra images for our simulated clusters using the following procedure.

First, energy-dependent surface brightness maps are constructed by projecting X-ray emission from all the gas cells associated with each cluster along each of three orthogonal axes. The energy dependence is stored as the third dimension of the map between 0.04 and 10 keV with spacing $\Delta\mathrm{E} = 0.0498$ keV. With the gas density ρ and temperature T of each cell in each simulation output and an assumed metallicity Z, the X-ray emissivity, $\epsilon_E = \rho^2 \Lambda_E(T, Z, z)$, is computed using the single-temperature MEKAL model (Mewe et al., 1985; Kaastra & Mewe, 1993; Liedahl et al., 1995) implemented in the utility XSPEC (Arnaud, 1996).

With these energy-dependent surface brightness maps in hand for each cluster, we then use MARX[2] to simulate Chandra X-ray observations. Given the position and spectrum of a source, MARX can perform ray generation, apply built-in models for Chandra's aspect motion and mirror and detector responses, and output photon event files in FITS format for analysis with standard observational tools. The user-defined source model supported

[2]http://space.mit.edu/ASC/MARX

by MARX allows us to generate light rays from astronomical sources with arbitrary shape and spectrum. We assign the positions and energies of photons based on the probability distribution defined by our 3D surface brightness maps. Each cluster is "observed" with Chandra's CCD chip ACIS-S using an exposure time that ensures 2 million photons are collected, longer than typical deep observations. The particular long exposure time is chosen to minimize observational uncertainties since we are interested in the intrinsic scatter in cluster observables. The photon event files thus produced are processed with CIAO to extract the spectra within apertures of size R_{500} centered on each cluster's surface brightness peak. The spectroscopic temperatures T_X are obtained by using XSPEC to fit the spectra in the range 0.5 to 10 keV, the range often used by observers (e.g., Vikhlinin et al., 2006). We tested the above procedure using a set of isothermal clusters with β-model density profiles, varying the input temperature from 0.5 to 5 keV and using two different metallicities, $Z = 0$ and $Z = 0.3Z_{\odot}$. We have verified that for our chosen exposure time, the input temperatures are recovered within 1σ errors in all cases. For simplicity we assume zero metallicity in the following analysis. A detailed description and verification tests of the same X-ray simulator can be found in the appendix of Zu Hone et al. (2009).

The left panel in Figure 2.1 shows T_X versus the emission-weighted temperature T_{ew} measured within R_{500} for clusters with M_{500} above 2×10^{13} $M_{\odot}$ at $z = 0$. We find that T_{ew} is on average biased high with respect to T_X with a fractional bias of $(T_{ew} - T_X)/T_X \sim 23\%$, consistent with previous findings (Mathiesen & Evrard, 2001; Rasia et al., 2005). As pointed out by previous authors, this systematic shift is due to the superposition of cluster gas with different temperatures along the line of sight. To verify that this explains our result, we performed a test for a set of beta-model clusters whose gas is composed of two different temperatures, with varied cool-gas fractions. We found that T_{ew} is higher than T_X in all cases. We can understand this result by expressing these temperature measures in the following way: $T \equiv \int W(T) T dV / \int W(T) dV$, where $W(T)$ is a weighting function. For T_{ew}, $W(T) = \Lambda(T) \propto \sqrt{T}$ if dominated by bremsstrahlung emission. Assuming T_X can be approximated by the spectroscopic-like temperature, then $W(T) \sim T^{-3/4}$ (Rasia et al., 2005), that is, T_X tends to weight more on the cool gas in a cluster and thus is systematically lower than T_{ew} in general.

To see whether this systematic shift is dependent on merger types, we also plot in the right panel the normalized distributions of deviations from the best-fit relation for relaxed clusters, minor mergers, and major mergers. Comparing their distributions using the Wilcoxon Rank-Sum test shows that the systematic shift between T_X and T_{ew} is similar for relaxed clusters and minor mergers, but is larger at a statistically significant level for major mergers, based on our merger definitions. This is also in agreement with Mathiesen & Evrard (2001), who found

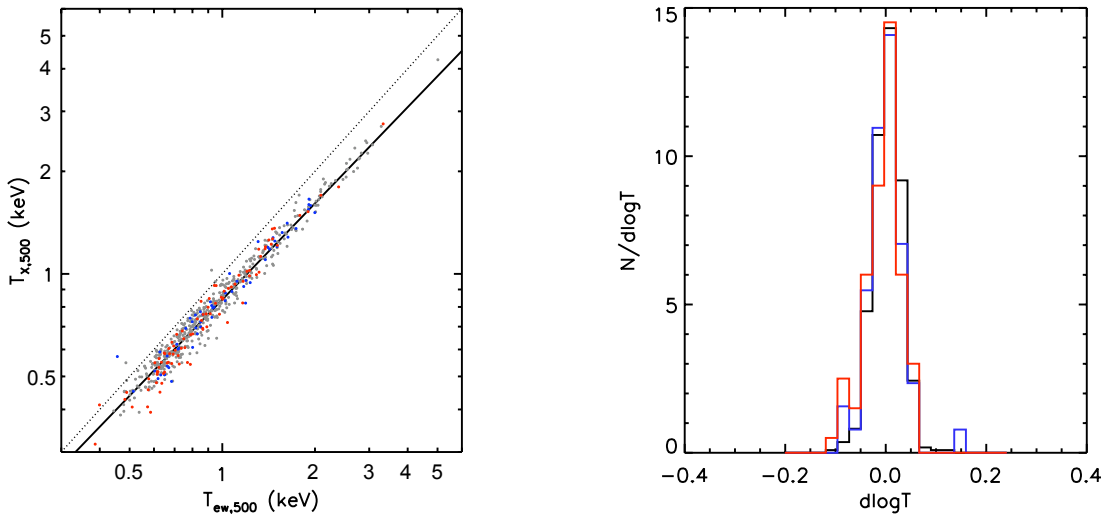

Figure 2.1: *Left*: $T_{X,500}$ vs. $T_{ew,500}$ for clusters with M_{500} above $2 \times 10^{13} M_{\odot}$ at $z = 0$. The relaxed clusters, minor mergers and major mergers are plotted using grey, blue, and red symbols, respectively. The solid line is the best-fit relation. Comparing to the dotted line with a slope of 1 shows that T_{ew} is biased high with respect to T_X. *Right*: Normalized distributions of deviations from the best-fit relation in $T_{X,500}$ vs. $T_{ew,500}$ scaling for relaxed clusters (black), minor mergers (blue), and major mergers (red).

that the difference between T_X and T_{ew} is larger for merging clusters because the spectral fit is largely contributed by X-ray photons from the bright and cool accreted subclumps.

2.3.3 Substructure measures

High-resolution X-ray images of clusters taken with Chandra and XMM-Newton have revealed disturbed ICM structures such as shocks, bubbles, and cold fronts (e.g. Bîrzan et al., 2004; Hallman & Markevitch, 2004). Various substructure measures have been used to quantify the irregularity, such as centroid offset (Mohr et al., 1995) and power ratios (Buote & Tsai, 1995, 1996). In previous work this irregularity is often assumed to be associated with mergers. To examine the effectiveness of the substructure measures and the adequacy of using them as indicators of dynamical state, we calculate the centroid offset and power ratios in addition to other theory-based definitions of cluster mergers in our simulation.

There are many ways to define the centroid offset. For observed clusters, it can be defined as the variance in the centroids of cluster regions above several surface-brightness isophotes (e.g., O'Hara et al., 2006). Since the offset is essentially a measure of the distance between the surface brightness peak and the cluster centroid, Kay et al. (2007) used a simpler definition

for their simulated clusters,

$$w = \frac{|\vec{R}_{\Sigma,max} - \vec{R}_{\Sigma,cen}|}{R_{500}}, \tag{2.1}$$

where $\vec{R}_{\Sigma,max}$ is the position of the surface brightness peak and $\vec{R}_{\Sigma,cen}$ is the surface-brightness centroid. We compared the centroid offsets calculated using both methods and found that these two definitions give similar results. We will use the latter definition hereafter since it is more strongly correlated with the power ratios for our simulated clusters.

Power ratios are the multipole moments of surface brightness measured within a circular aperture centered on the cluster's centroid. The moments, a_m and b_m (defined below), are sensitive to substructures in the surface brightness distribution. This method is motivated by the multipole expansion of the two-dimensional gravitational potential,

$$\Psi(R,\phi) = -2Ga_0 \ln\left(\frac{1}{R}\right) - 2G\sum_{m=1}^{\infty} \frac{1}{mR^m}(a_m \cos m\phi + b_m \sin m\phi) \ . \tag{2.2}$$

The moments a_m and b_m are

$$\begin{aligned} a_m(R) &= \int_{R'\leq R} \Sigma(\vec{x}')(R')^m \cos m\phi' d^2x', \\ b_m(R) &= \int_{R'\leq R} \Sigma(\vec{x}')(R')^m \sin m\phi' d^2x', \end{aligned} \tag{2.3}$$

where $\vec{x}' = (R', \phi')$, R is the aperture radius, and Σ is the surface mass density, or surface brightness in the case of X-ray observations.

The mth power P_m is the azimuthal average of the amplitude of Ψ_m, the mth term in the multipole expansion of the potential given in equation (2.2),

$$P_m(R) = \frac{1}{2\pi}\int_0^{2\pi} \Psi_m(R,\phi)\Psi_m(R,\phi)d\phi. \tag{2.4}$$

For $m = 0$ and $m > 0$, we have

$$\begin{aligned} P_0 &= [a_0 \ln(R)]^2 \\ P_m &= \frac{1}{2m^2R^{2m}}(a_m^2 + b_m^2), \end{aligned} \tag{2.5}$$

respectively. The power ratios are thus P_m/P_0, the mth power normalized by the flux within R.

For each cluster we compute P_2/P_0, P_3/P_0, and $P_{(1)}/P_0$. The quantities without parenthetical subscripts are evaluated about the surface brightness centroid (therefore P_1 vanishes

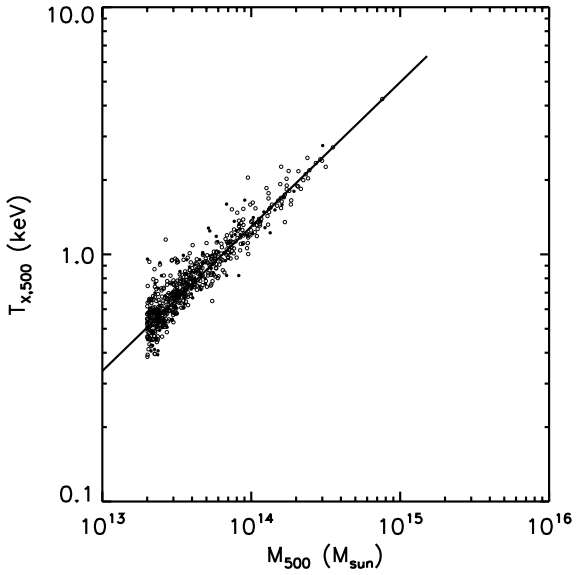

Figure 2.2: M_{500}–$T_{X,500}$ relation for clusters with M_{500} above $2 \times 10^{13} M_{\odot}$ at $z = 0$. Clusters identified by at least one of the five merger diagnostics are plotted using filled circles; relaxed clusters are plotted using open circles. The error bars in T_X ($< 0.5\%$) are smaller than the symbol size and are thus omitted. The solid line is the best-fit relation for all clusters.

by definition). The quadrupole power, P_2, is related to the degree of flattening or ellipticity. The next odd moment, P_3, is sensitive to unequal bimodal structures. $P_{(1)}/P_0$, which is calculated about the surface brightness peak, measures gas distribution around the peak and thus is similar to the centroid offset. Since the power ratios are sensitive to substructures at the scale of the aperture radius R, each of the power ratios is calculated using three different radii, R_{500}, R_{200}, and 1 Mpc, for each cluster.

2.4 Results

Figure 2.2 shows the M_{500}–$T_{X,500}$ relation for clusters with M_{500} above $2 \times 10^{13} M_{\odot}$ at $z = 0$. All quantities are viewed along the x-direction in the simulation box. The best-fit relations for all clusters as well as different subgroups are given in Table 2.1. Note that the best-fit slopes for relaxed and merging clusters are different. The difference in the slopes implies that there is variation in the slopes derived from observed clusters using different selected subsamples. This systematic uncertainty in the slope, which is $\sim 5\%$ by comparing the slopes of the merging and relaxed clusters in Table 2.1, will contribute to the uncertainties in cosmological parameters. For example, it will translate into a systematic uncertainty of

Table 2.1: Best-fit parameters in the mass-temperature relations, $\log(T_{X,500}) = a + b\log(M_{500})$, for clusters at $z = 0$. Errors in the parameters are the 1σ errors.

Subgroup	Count	a	b
All	619	-8.067 ± 0.004	0.5842 ± 0.0003
Relaxed	478	-7.981 ± 0.004	0.5780 ± 0.0003
Merging	141	-8.409 ± 0.008	0.6093 ± 0.0006
Minor	55	-8.379 ± 0.013	0.6068 ± 0.0009
Major	86	-8.050 ± 0.011	0.6163 ± 0.0008

$\sim 3\%$ in σ_8 when using observed cluster samples including and excluding merging clusters. This is relatively small compared to the current level of uncertainty ($\sim 10\%$) in determining the cosmological parameters, but as the constraints are improved to a few percent in the future, one has to keep it in mind when comparing results using different cluster selection criteria.

While we are able to reproduce the self-similar M_{200}–T_{ew} scaling relation (e.g., Bryan & Norman, 1998), the slope and normalization of the M_{500}–$T_{X,500}$ relation are both smaller compared to observed values. This deviation is mainly due to missing baryonic physics and the use of different mass estimates (e.g., Borgani et al., 2004; Nagai et al., 2007a). Matching the slope and normalization of the scaling relations with observed values is a subject of great interest on its own and will be investigated when we incorporate more realistic models for the baryonic component. For the purpose of this study, we will focus on the scatter in these relations and the relative importance of clusters of different merger histories.

2.4.1 Distribution of intrinsic scatter

Figure 2.3 shows the normalized distribution of the logarithmic deviations of temperature from the best-fit M_{500}–$T_{X,500}$ relation at $z = 0$. The RMS scatter for our whole sample is 6.10%, which is smaller than the values obtained by simulations with cooling and heating, such as 13.6% in Nagai et al. (2007a) and 20% in O'Hara et al. (2006), who also used the spectroscopic temperature and true mass. It is difficult to directly compare with observed values because the observationally-estimated intrinsic scatter is dependent on how the measurement errors are determined and thus displays a wide range in the literature, from 3.9% in (Arnaud et al., 2005) to 17% in (O'Hara et al., 2006).

In the left panel of Figure 2.3 we compare the distributions of merging (red) and relaxed (black) clusters, while the right panel plots for minor and major mergers individually. The

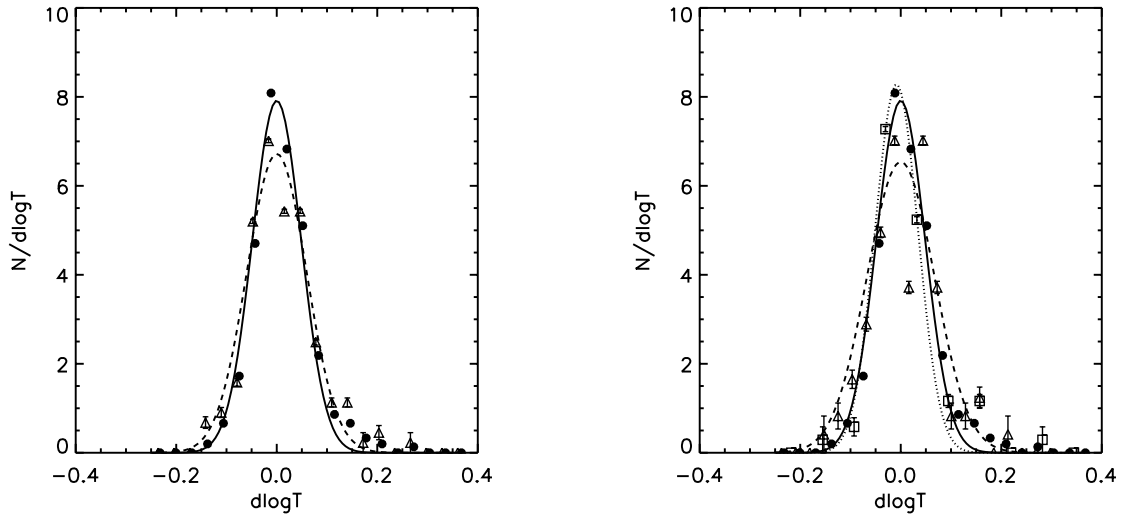

Figure 2.3: *Left*: Normalized distribution of log scatter in the M_{500}–$T_{X,500}$ relation at $z = 0$ for merging and relaxed clusters. The curves are the best-fit lognormal distributions. Merging clusters are plotted using open triangles and dashed lines; relaxed clusters are plotted using filled circles and solid lines. *Right*: Normalized distribution of log scatter and the best-fit curves for minor mergers (open squares and dotted lines), major mergers (open traiangles and dashed lines) and relaxed clusters (filled circles and solid lines).

two distributions on the left display no apparent difference in their mean values. The standard deviation for merging clusters appears to be larger than that of the relaxed clusters. To test the hypothesis that the merging and relaxed distributions differ, we performed the Wilcoxon Rank-Sum (R-S) test and the F-variance (F-V) test to see whether these two populations have significantly different mean values or variances, respectively. A small value (< 0.05 for a significance level of 5%) returned by the tests is often adopted to indicate a significant difference between these two populations. We performed the tests on different merging subgroups and summarize the results in Table 2.2.

The R-S test results show that the mean values do not differ significantly among all populations, which means that the intrinsic scatter is unbiased for merging and relaxed clusters at $z = 0$. The F-V tests for all mergers and minor mergers show that their standard deviations, or the amount of scatter, are significantly larger than that of the relaxed ones. For clusters at $z = 1$, there is also no bias between merging and relaxed populations. The amount of scatter for merging clusters also tends to be greater than relaxed clusters, although only major mergers show a significant result. We will discuss the possible reasons for this trend in the next two sections.

Since the form of scatter can affect the observed scaling relations, we also test the Gaus-

Table 2.2: Significance tests on the distribution of scatter for different populations at $z = 0$ and $z = 1$. The R-S and F-V test results for each subgroup are relative to the relaxed clusters.

Subgroup	z	N	Mean	R-S Test	$\sigma_{rms}(\%)$	F-V test	K-S test
Relaxed	0	478	1.31×10^{-2}	-	5.87	-	2.5×10^{-2}
Merging	0	141	8.67×10^{-3}	0.134	6.90	0.014	2.5×10^{-2}
Minor	0	55	1.11×10^{-2}	0.146	7.21	0.029	2.0×10^{-1}
Major	0	86	7.09×10^{-3}	0.253	6.72	0.086	2.5×10^{-2}
Relaxed	1	102	7.14×10^{-3}	-	4.85	-	2.6×10^{-4}
Merging	1	121	8.72×10^{-3}	0.493	5.71	0.091	6.5×10^{-3}
Minor	1	46	1.41×10^{-2}	0.230	5.25	0.504	8.0×10^{-2}
Major	1	75	5.45×10^{-3}	0.290	5.98	0.049	6.5×10^{-3}

sianity of the distribution of scatter in log space by fitting it with a Gaussian curve and using the Kolmogorov-Smirnov (K-S) test to see if the two distributions differ significantly. Again, a small value represents a significant deviation from the Gaussian distribution. The test results show that the distributions of scatter for all populations but minor mergers differ from a lognormal distribution at a significant level. There is an even stronger signature of deviation from lognormal at $z = 1$. We note that the deviation of the scatter from a lognormal distribution may affect results from some of the self-calibration studies assuming a lognormal distribution of scatter (e.g., Lima & Hu, 2005) and should be taken into account to correctly interpret the obtained constraints on the cosmological parameters.

2.4.2 Intrinsic scatter vs. halo concentration

In the following two sections we will investigate the physical origin of the M_{500}–$T_{X,500}$ scatter by correlating it with cluster properties that are related to how the clusters are formed. In particular, we first show that the intrinsic scatter depends strongly on halo concentration. Then we discuss the contribution of scatter from recent merging events in the following section.

Figure 2.4 shows a strong positive correlation between the scatter in the M_{500}–$T_{X,500}$ relation and the scatter in the M_{500}–(R_{200}/R_{500}) relation. The correlation coefficient is 0.64, with a probability of zero, given by the Spearman Rank-Order Correlation test (Press et al. 1992, §14.6; probability of one means no correlation). To ensure that this result is not biased by the lower-mass clusters whose R_{500} values are close to the resolution of the simulation, we raised the mass threshold to $M_{500} \geqslant 10^{14} M_{\odot}$ and repeated the analyses for these well-resolved

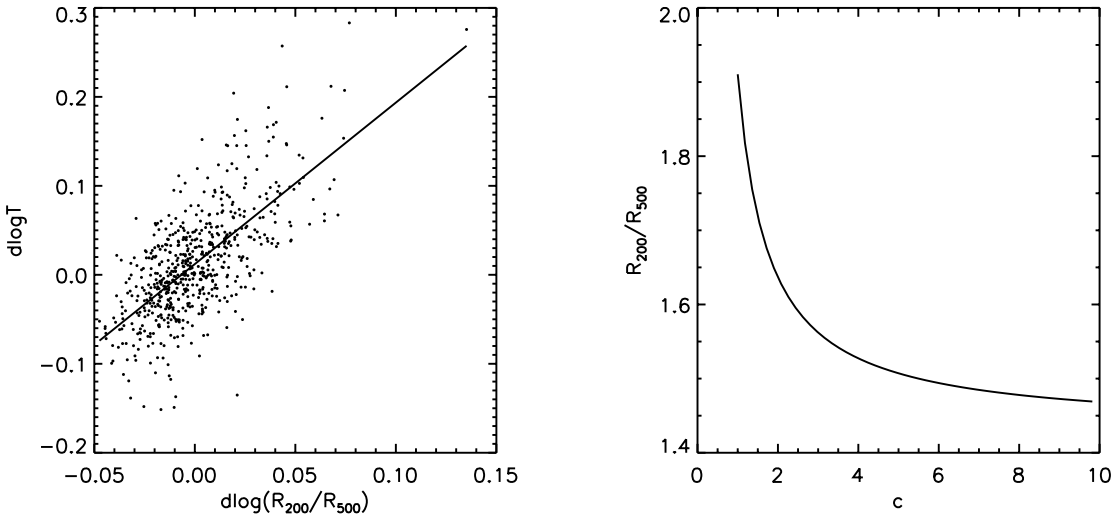

Figure 2.4: *Left:* M_{500}–$T_{X,500}$ scatter versus M_{500}–R_{200}/R_{500} scatter. There is a significant positive correlation, with correlation coefficient 0.64. The solid line is the best-fit relation $d\log T_X = 1.81 \times d\log(R_{200}/R_{500})$. *Right:* Relation between R_{200}/R_{500} and the halo concentration parameter, $c \equiv R_{200}/R_s$, for an NFW profile.

systems. We found that for the 67 selected massive clusters, the correlation still holds, with Spearman correlation coefficient 0.36 and probability 0.003. Note that we correlate with $d\log(R_{200}/R_{500})$ instead of the raw value of R_{200}/R_{500} because the latter is a function of cluster mass. By doing so we exclude the effect of different cluster masses, focusing on the variation in halo concentrations. R_{200}/R_{500} is a monotonically decreasing function of the halo concentration parameter, usually defined as $c \equiv R_{200}/R_s$, where R_s is the scale radius of a cluster. Therefore, for clusters with similar masses, more concentrated clusters tend to lie under the mean mass-temperature relation, while the puffier clusters tend to scatter high.

The relation between R_{200}/R_{500} and c is less obvious, so we derive their relation assuming an NFW profile (Navarro, Frenk, & White 1995; 1996, hereafter NFW) in the following. For a cluster that has an NFW density profile, the mass enclosed within a normalized radius of $x \equiv R/R_s$ is

$$\begin{aligned} M(<x) &= 4\pi\rho_s R_s^3 \left[\ln(1+x) - \frac{x}{1+x}\right] \\ &\equiv 4\pi\rho_s R_s^3 f(x), \end{aligned} \tag{2.6}$$

where ρ_s is the density at the scale radius R_s. Also, the mass in the spherical overdensity

definition is

$$M_\Delta = \frac{4\pi}{3}\Delta\rho_{crit}(x_\Delta R_s)^3, \tag{2.7}$$

where Δ is the overdensity and ρ_{crit} is the critical density of the universe. Equating equation (2.6) and (2.7) gives

$$\Delta\frac{x_\Delta^3}{f(x_\Delta)} = 3\frac{\rho_s}{\rho_{crit}}, \tag{2.8}$$

which is a constant for the cluster under consideration. Therefore, the relation between x_{500} and x_{200} (or c, recall $c \equiv R_{200}/R_s$) is

$$\frac{x_{500}^3}{f(x_{500})} = \frac{2}{5}\frac{c^3}{f(c)}. \tag{2.9}$$

We can use this relation to numerically solve for x_{500} as a function of c, and then the relation between R_{200}/R_{500} and c is simply

$$\frac{R_{200}}{R_{500}} = \frac{c}{x_{500}(c)}. \tag{2.10}$$

This relation is plotted in the right panel of Figure 2.4. We choose to use the parameter R_{200}/R_{500} instead of the original halo concentration parameter c because it has two advantages. The first is to avoid introducing the uncertainty in fitting an NFW profile, especially for less massive clusters, since the fitting is very sensitive to the resolution in the central region of the cluster. Moreover, our analyses involve not only relaxed clusters but also merging ones, for which R_{200}/R_{500} is actually more well-defined than c.

One can understand why the correlation between the M_{500}–$T_{X,500}$ scatter and the halo concentration exists using the virial theorem. Consider the simplest case for an isolated system: $2T + W = 0$, where T and W are the total kinetic and gravitational binding energy of the system, respectively. Then in general,

$$\frac{k_B T_{vir}}{\mu m_p} \propto \frac{GM_{vir}}{R_{vir}}, \tag{2.11}$$

where k_B is the Boltzmann constant, μ is the mean molecular mass of the gas, m_p is the mass of a proton, and T_{vir}, M_{vir}, and R_{vir} are the virial gas temperature, mass, and radius of the system. Since the relations between the virial quantities and the quantities in the overdensity definition depend on individual cluster profiles, or halo concentrations, the M_Δ–T_Δ relation derived from above would have a normalization which is a function of concentration. This is why we expect the scatter in the M_{500}–$T_{X,500}$ relation to correlate with the concentration

parameter.

Halo concentrations have been shown to be related to the epoch at which the halo formed (NFW 1997; Wechsler et al. 2002; Zhao et al. 2003; Neto et al. 2007). Since we have the mass assembly histories of all the simulated clusters, it is straightforward to derive the cluster formation time based on the definition that a cluster "forms" when it first exceeds a certain fraction of its final mass. The commonly-adopted thresholds include 10%, 25%, 50%, and 70%. Since more concentrated halos tend to form at higher redshift, a negative correlation between the M_{500}–$T_{X,500}$ scatter and the formation redshift is expected. Indeed we find significant negative correlations with the time when the cluster first reached one half, $t_{1/2}$, and one quarter, $t_{1/4}$, of its final mass (see Figure 2.5). These correlations are not as tight as the one with halo concentrations, probably due to the fact that the correlation between the halo concentration and the cluster formation time itself has a very large scatter, and also that the variation in halo concentrations cannot be fully accounted for by the variation in cluster formation time (Neto et al., 2007). But the significance of these correlations with cluster formation times supports our finding that the scatter correlates with halo concentrations. Therefore, we can say that cluster assembly histories leave imprints on the shapes of clusters at the present day that help to determine clusters' positions on the mass-observable scaling relation.

The strong correlation in Figure 2.4 suggests that the variation in halo concentrations contributes to a significant amount of the intrinsic scatter in the M_{500}–$T_{X,500}$ relation. It also implies that when we are provided the best-fit relation, $d\log T_X = 1.81 \times d\log(R_{200}/R_{500})$, it is possible to use $d\log(R_{200}/R_{500})$ as a third parameter to normalize T_X in the M_{500}–$T_{X,500}$ relation, and thus reduce the scatter. After removing the effect of halo concentrations, we find that the RMS scatter decreases from 6.10% to 4.49%, a reduction of $\sim 26\%$ of its original value. The corrected M_{500}–$T_{X,500}$ relation is shown in Figure 2.6.

We can explain the trend found in the previous section using this correlation too. Figure 2.7 shows the distributions of halo concentration for merging and relaxed clusters at $z = 0$ and $z = 1$. For both redshifts, the distribution of halo concentration for merging clusters is more dispersed than for relaxed clusters, as also found in Neto et al. (2007). If the variation in halo concentrations is important to the M_{500}–$T_{X,500}$ scatter, as the above correlation suggests, then it is reasonable that merging clusters have a greater amount of scatter than relaxed ones. One may try to relate this trend to the dynamical state of clusters because the temperature excursions during mergers could also drive the scatter. However, in the next section we will show that this is not the case.

In summary, we have found that the scatter in the M_{500}–$T_{X,500}$ relation partly originates from the variation in halo concentrations, with more concentrated or early-formed clusters

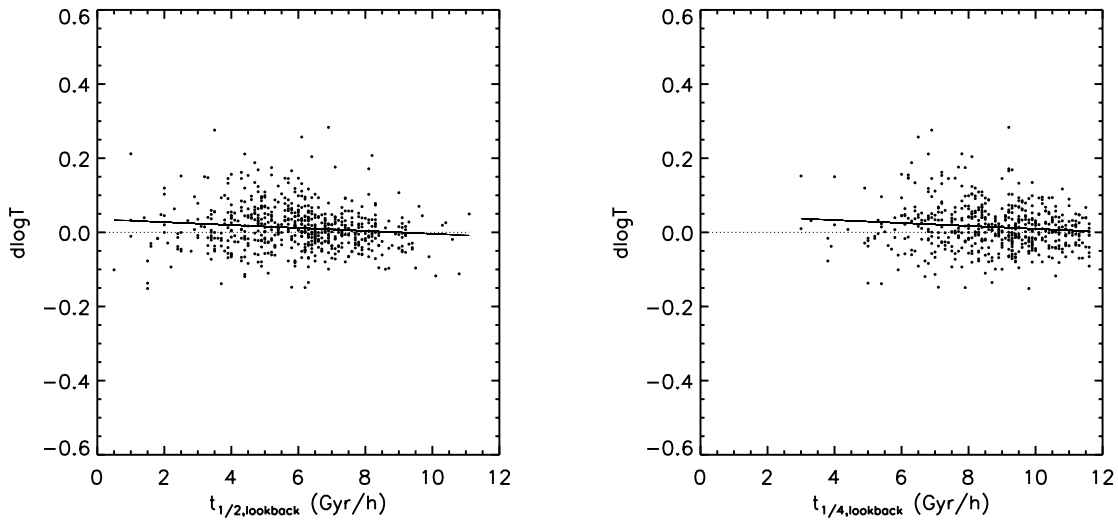

Figure 2.5: *Left:* M_{500}–$T_{X,500}$ scatter correlated with cluster formation time, defined as the time when a cluster first obtained half of its final mass. The Spearman correlation coefficient is -0.14, with a probability of 1.95×10^{-4} (probability of one means no correlation). *Right:* Same plot with x-axis being the time a cluster reached 1/4 of its final mass. The correlation coefficient is -0.11, with a probability of 9.4×10^{-3}. Both plots show that clusters that are formed at earlier/later times tend to scatter low/high.

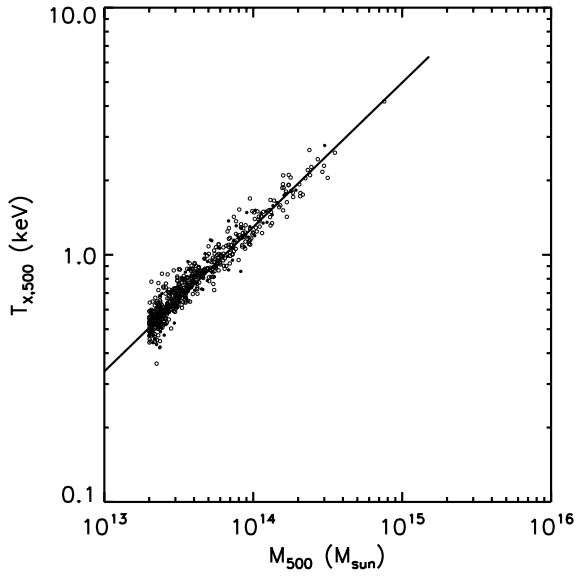

Figure 2.6: M_{500}–$T_{X,500}$ relation corrected for halo concentrations. Notations are the same as in Figure 2.2.

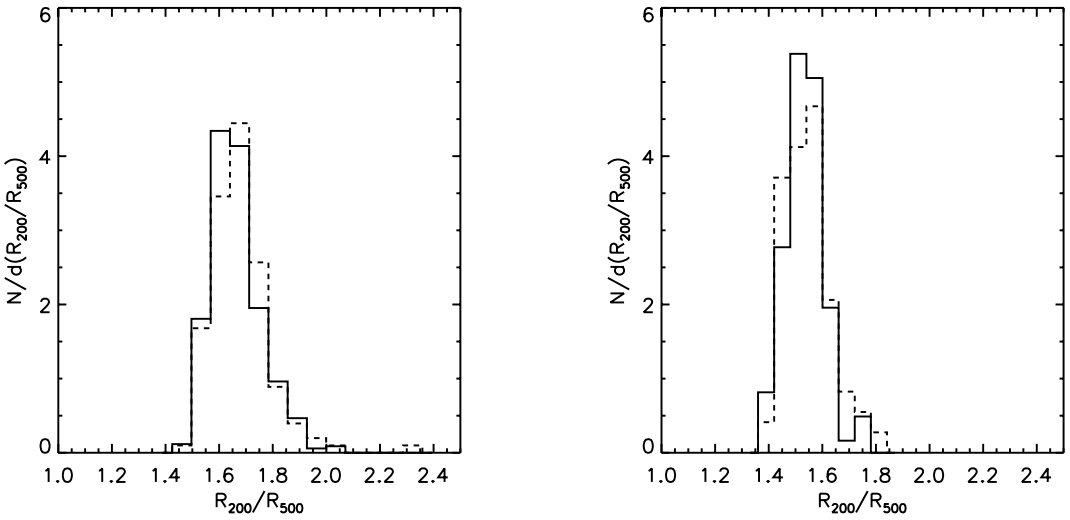

Figure 2.7: Distribution of R_{200}/R_{500} for relaxed (solid) and merging (dashed) clusters at $z = 0$ (left panel) and $z = 1$ (right panel). According to the F-V test, merging clusters have larger dispersions than relaxed clusters for both $z = 0$ and $z = 1$ datasets, with significance 0.0044 and 0.0367, respectively.

lying below the mean (they are cooler), while puffier clusters that are formed recently tend to be hotter than clusters with similar masses. Using the strong correlation between the scatter and halo concentrations, the scatter can be greatly reduced to get a much tighter relation to be used for cosmology. The correlation can also explain the trend seen in the previous section that merging clusters have a greater amount of scatter than relaxed ones. Note that our simulation adopted the value of $\sigma_8 = 0.74$ from WMAP3 results, which is smaller than $\sigma_8 = 0.796$ from WMAP5. Although choosing a smaller σ_8 would decrease the average concentration of clusters with a fixed mass (e.g. Duffy et al., 2008), it is the *variation* of concentration that correlates with the scatter. Therefore the correlation should still hold if a higher σ_8 is used.

2.4.3 Intrinsic scatter vs. recent mergers

The other possible origin of the scatter in our simulation is the departure from hydrostatic equilibrium due to cluster mergers. Cluster mergers are among the most energetic events in the universe. When two clusters merge, their gas is compressed and heated by merger shocks. This effect can boost the luminosity and temperature of the cluster a few times higher than its pre-merger value, as found in ideal merger simulations (Ricker & Sarazin, 2001; Poole et al., 2007). Therefore, our aim is to investigate how merger events statistically

influence the cluster scaling relations.

In order to see how merging events influence the observable quantities of clusters, we correlate their mass-temperature scatter with their dynamical state. Two different methods are used to quantify the dynamical state. The first is based on the actual cluster merger histories, where we use the time since last merger as an indicator. The second one is motivated by observations that unrelaxed clusters often have more substructures than relaxed clusters. We discuss results using both methods in the following.

First we correlate the M_{500}–$T_{X,500}$ scatter with the time since last merger, t_{last} (thus clusters that just underwent mergers would have $t_{last} = 0$). As shown in Figure 2.8, there is a trend for more recently merged clusters to lie below the mean relation, but only the correlation for major mergers has a high probability. Note that although the scatter here is uncorrected, this correlation is not due to the effect of halo concentrations because halo concentrations work in the opposite direction, as described in § 2.4.2. Therefore, this trend may be due to clusters that have just merged with a cool clump and are still on their way to virialization, as illustrated by the following example. Figure 2.9 is the time history constructed from our merger tree analysis for a cluster undergoing a minor merger. Here we plot the evolution of mass, temperature, and substructure measures versus lookback time ($t = 0$ for today). We can see that at $t = 1.3$ Gyr, a clump of cold gas merged into the primary cluster. The cold accreted gas caused a jump in mass and substructure measures, but it reduced the average temperature of the cluster. This behavior thus tends to make merging clusters lie below the M_{500}–$T_{X,500}$ relation when they have just merged and then gradually move up when they become virialized.

This trend is also seen when we correlate scatter with some of the substructure indicators, although the probabilities are not high. Figure 2.10 shows the correlation with the two substructure measures that give the highest probabilities, P_2/P_0 and P_3/P_0 measured with a fixed aperture radius 1 Mpc. Here we use a fixed aperture size because this gives power ratios that are weaker functions of cluster mass than substructures computed using R_{200} or R_{500}. This is to minimize covariance with halo concentrations through the mass dependence. This negative correlation between scatter and substructures again supports the idea that merging clusters tend to be cooler than clusters with similar masses.

But do recent mergers cause a problem statistically? Again we want to compare the distributions of scatter for the merging and relaxed populations in the same way as in § 2.4.1. But as discussed earlier, the trends are probably dominated by the effect of halo concentrations. Since we want to study the effect of recent mergers in isolation from other effects, we compute the statistics using the M_{500}–$T_{X,500}$ relation after correcting for halo concentrations (Figure 2.6) instead of the raw relation. In this way we can see whether the

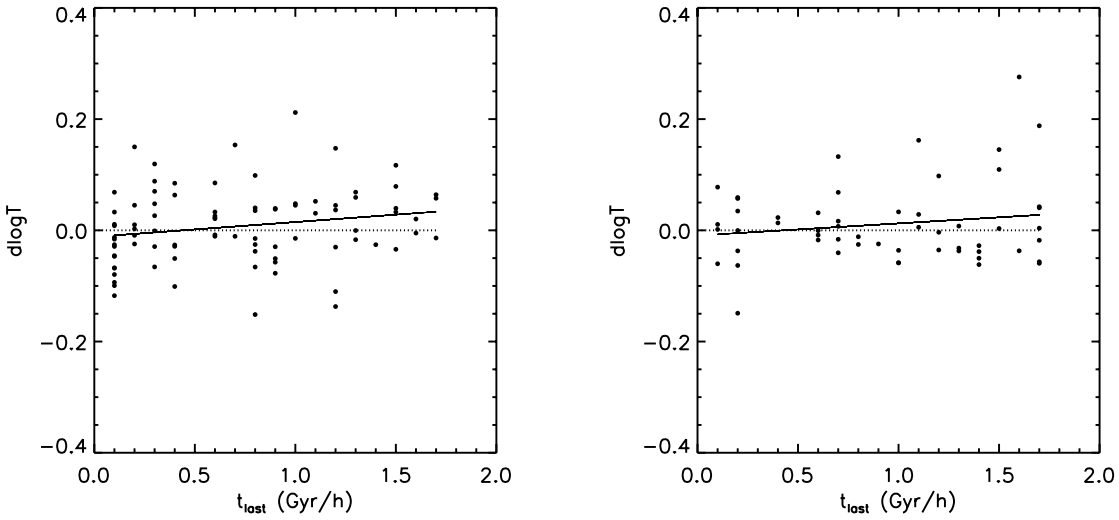

Figure 2.8: M_{500}–$T_{X,500}$ scatter versus the time since last merger for major mergers (left panel) and minor mergers (right panel) at $z = 0$. The Spearman correlation coefficients are 0.24 and 0.008, with probabilities of no correlation being 0.02 and 0.95 for major and minor mergers, respectively.

dynamical state of clusters is the second dominant factor in the scatter.

The distributions of the concentration-corrected scatter for merging and relaxed clusters at $z = 0$ are shown in Figure 2.11. Again we use the R-S test and F-V test to detect whether there is any difference in the mean values and variances of these two populations. The results are summarized in Table 2.3. We find that after removing the effect of halo concentration, the trend that merging clusters have a larger RMS scatter becomes insignificant. This supports our earlier statement that the behavior of the raw scatter is determined more by the distribution of halo concentrations than by the dynamical state of clusters. As for the mean values, there is a significant relative bias for merging clusters to have smaller means than relaxed clusters at $z = 0$. This bias can be due to the incomplete virialization of merging clusters we just described. However, it is also possible that we have over-corrected for the halo concentrations for merging clusters in comparison with relaxed clusters, because merging clusters are generally less concentrated (or have larger R_{200}/R_{500}, see Figure 2.7).

In summary, by correlating the scatter with the dynamical state of clusters using both merger tree and substructure analysis, we find a very weak trend that merging clusters tend to be cooler than relaxed clusters with similar masses. But this trend has a minor effect on the statistical properties of the scatter, i.e., the scatter for the merging clusters is neither biased nor wider spread compared to the relaxed ones at $z = 0$ and $z = 1$ (see Table

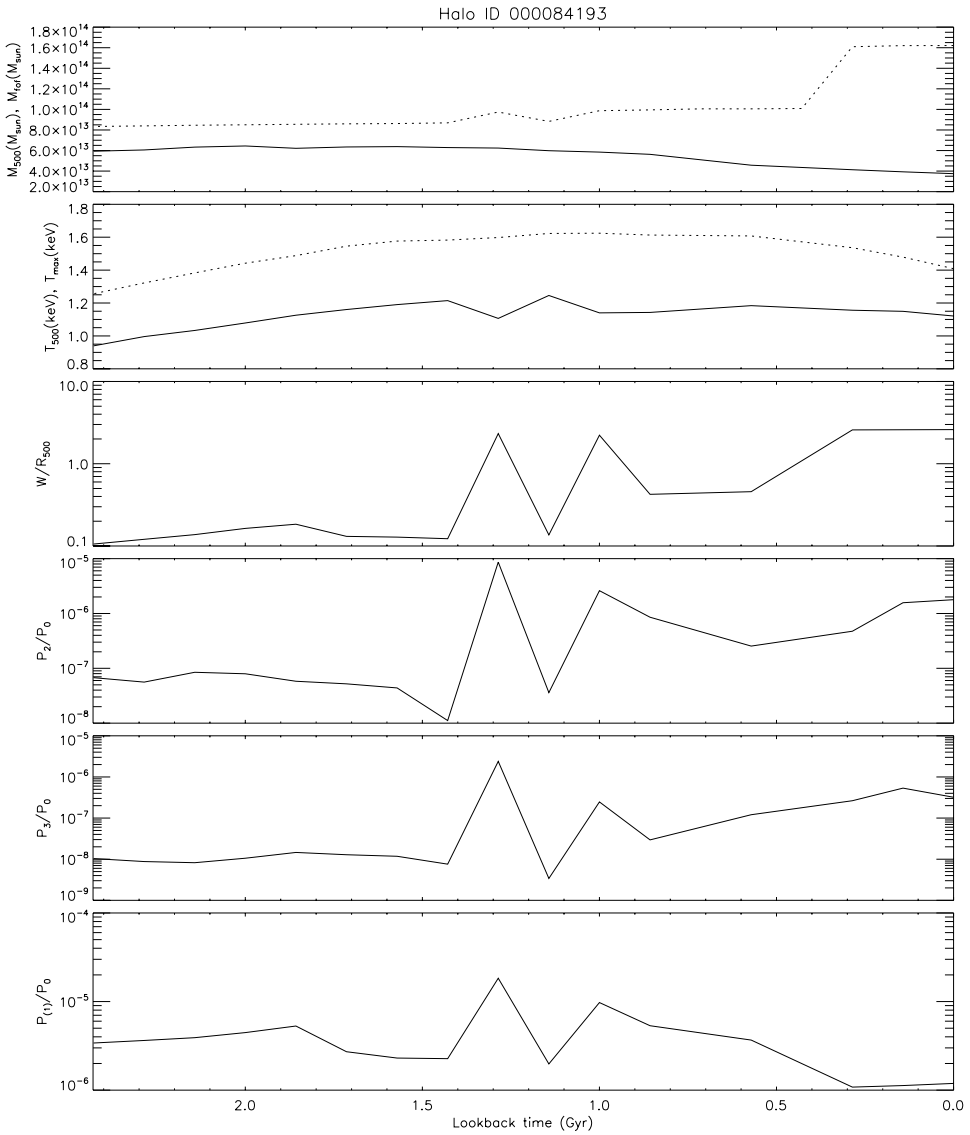

Figure 2.9: Example time history of a cluster that undergoes a minor merger. The solid (dashed) line is M_{500} (M_{fof}) in the first panel, T_{500} (T_{max}) in the second panel. The other panels show the evolution of the substructure measures.

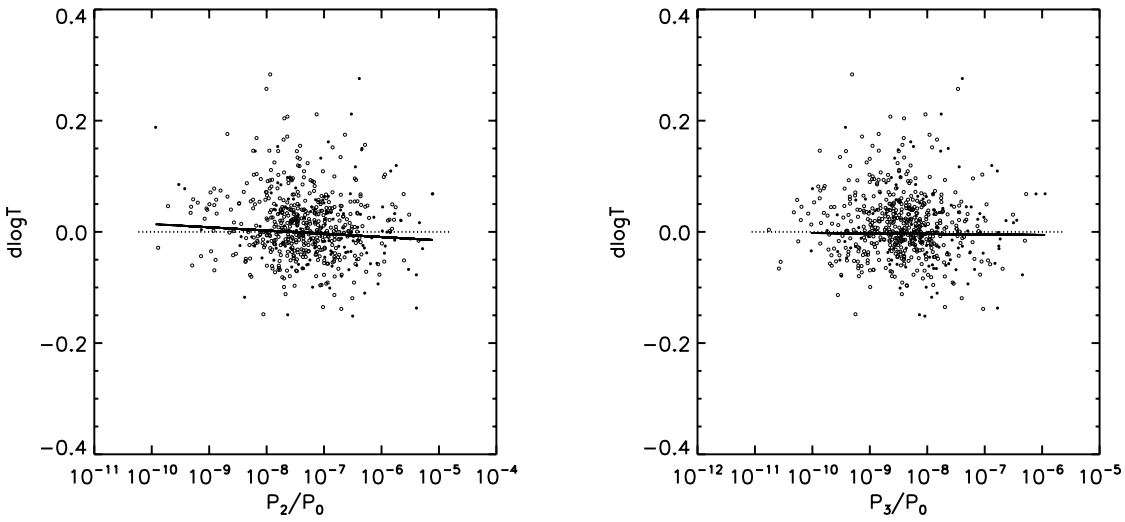

Figure 2.10: M_{500}–$T_{X,500}$ scatter versus substructure measures P_2/P_0 and P_3/P_0. Relaxed/merging clusters are plotted in open/filled circles. Weak negative correlations are found for merging clusters with probabilities of no correlation being 0.08 for P_2/P_0 and 0.34 for P_3/P_0.

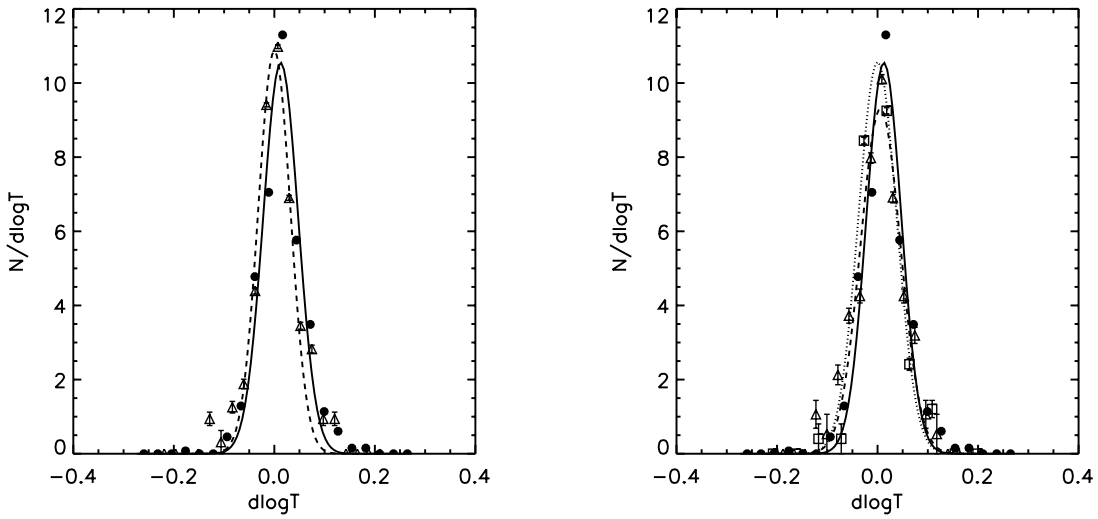

Figure 2.11: Distributions of scatter at $z = 0$ after correcting for the effect of halo concentrations. In the left panel, merging clusters are plotted using open triangles and dashed lines, and relaxed clusters are plotted using filled circles and solid lines. In the right panel, the merging clusters are separated into minor mergers (open squares and dotted lines) and major mergers (open traiangles and dashed lines).

Table 2.3: Significance tests on the distribution of scatter after removing the effect of halo concentrations for different populations at $z = 0$ and $z = 1$. The R-S and F-V test results for each subgroup are relative to the relaxed clusters.

Subgroup	z	N	Mean	R-S Test	$\sigma_{rms}(\%)$	F-V test
Relaxed	0	478	1.44×10^{-2}	-	4.42	-
Merging	0	141	4.27×10^{-3}	0.012	4.67	0.403
Minor	0	55	6.39×10^{-3}	0.058	4.63	0.612
Major	0	86	2.92×10^{-3}	0.034	4.72	0.406
Relaxed	1	102	1.03×10^{-2}	-	4.25	-
Merging	1	121	6.08×10^{-3}	0.329	4.88	0.151
Minor	1	46	1.30×10^{-2}	0.275	4.96	0.202
Major	1	75	1.86×10^{-3}	0.145	4.81	0.241

2.3). This implies that the dynamical state is not the second most important factor that contributes to the scatter, but that still other sources need to be found. However, the fact that the distributions of scatter for the merging and relaxed clusters are indistinguishable even out to higher redshift is good news for using cluster scaling relations in cosmology.

2.5 Discussion

2.5.1 Effect of dynamical state

In the previous section we have shown that the dynamical state of clusters has very little influence on the overall scatter in the M_{500}–$T_{X,500}$ relation. When we look at the merging population, there is even a tendency for merging clusters to be cooler than relaxed ones of similar masses. Although this can be explained by incomplete virialization of clusters merging with a cooler clump, it is still somewhat contrary to our intuition that merger shocks can heat the intracluster medium and raise the temperature of a merging cluster. We discuss the possible reasons for this result in the following.

One reason is that sometimes the merger shock is not captured by the projected R_{500} aperture. At the beginning of mergers, the shocks often occur in the outskirts of clusters. So in order for the shock to be captured inside R_{500}, either the shock has to propagate into the R_{500} region of the main cluster, or the two clusters have to merge roughly along the line of sight in order to affect $T_{X,500}$. The cluster history shown in Figure 2.12 is one example of such a case. At $t = 1.3$ Gyr, the substructure measures increase, indicating the start of the merger event. The maximum temperature in the cluster is increased by the merger shock,

but $T_{X,500}$ is unaffected because the shock-heated gas lies beyond the projected aperture radius R_{500}. Even if the merger shock is within R_{500}, the spectroscopic temperature is not as sensitive to shocks as the emission-weighted temperature because when the shock and other cooler gas in the cluster are projected along the line of sight, the spectral fit tends to put more weight on the cooler gas (Mazzotta et al., 2004).

Secondly, the duration of the temperature boost is typically only ~ 0.5 Gyr (Ricker & Sarazin, 2001; Poole et al., 2007), and hence only a fraction of the unrelaxed clusters are observed during the transient excursion period. Moreover, even for those clusters that have just undergone major mergers, the increase in mass and temperature are often comparable. For example, a 3:1 merger would have a mass jump of $M_f/M_i \sim 1.33$ and a temperature jump of $T_f/T_i \sim 2$ depending on the impact parameter of collision. Thus clusters tend to evolve roughly parallel to the scaling relation, as also suggested by previous works (e.g. Poole et al., 2007).

Finally, merging clusters are the minority population compared to relaxed clusters. The fraction of clusters that had a merger within the past 3 Gyr is $\sim 23\%$ at $z = 0$ and $\sim 54\%$ at $z = 1$, while major mergers are rarer. All these effects combined are responsible for diluting the influence of mergers on the scatter and making their distributions indistinguishable from relaxed clusters.

2.5.2 Effectiveness of substructure indicators

Substructure measures, such as centroid offsets and power ratios, have often been used in earlier studies to identify unrelaxed clusters (e.g. O'Hara et al., 2006; Kay et al., 2007; Jeltema et al., 2008). Observationally, they are quantities that link most effectively to the dynamical state of clusters (Mohr et al., 1993; Buote & Tsai, 1996). In simulations, they are easy to derive and to compare with observations. However, they still have some limitations, such as the projection effect.

In our study we have extended the analysis of the dynamical state of clusters by constructing cluster merging histories, because these provide more information about the true dynamics of clusters during mergers than morphology-based measures, which are subjected to observational limitations. This is the first time that these two approaches have been compared to see how effectively the substructure measures can recover the true merging population.

Figure 2.13 shows the negative correlations between two of the substructure measures as seen in the x projection of the simulation box and the time since the last $\leq 5:1$ merger for $z = 0$. The filled and open circles are merging and relaxed clusters identified by the merger

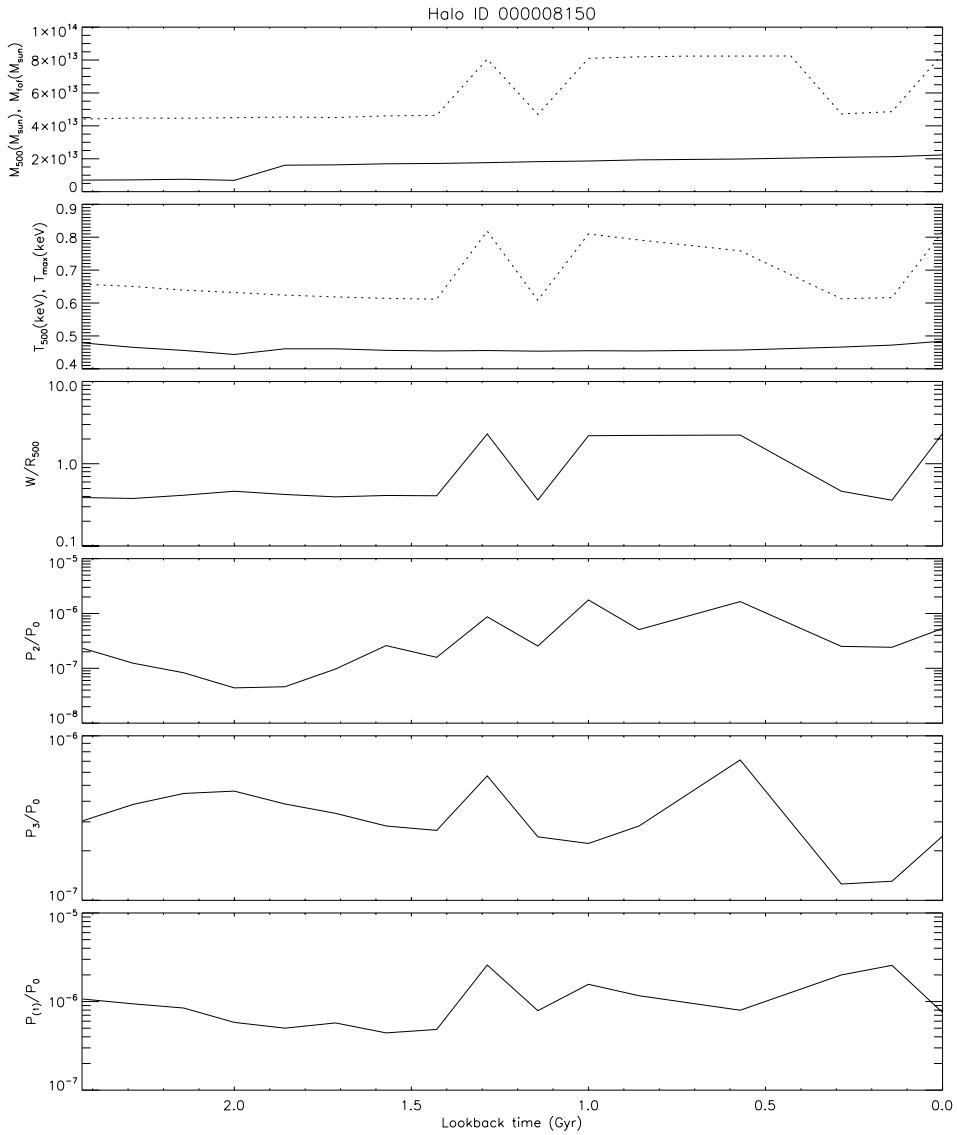

Figure 2.12: Example time history of a cluster that undergoes a major merger. The solid (dashed) line is M_{500} (M_{fof}) in the first panel, T_{500} (T_{max}) in the second panel. The other panels show the evolution of the substructure measures.

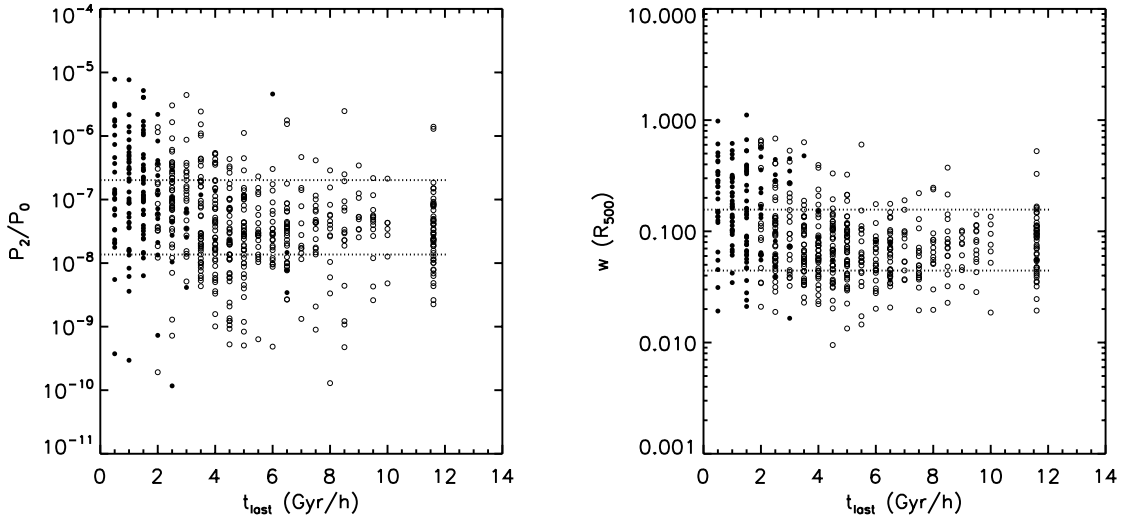

Figure 2.13: Substructure measures P_2/P_0 and w in x projection versus the time since the last $\leq 5:1$ merger. The filled and open circles are merging and relaxed clusters identified by the merger tree diagnostic, respectively. The two horizontal dashed lines mark the upper and lower 20% of all clusters that have the highest and lowest substructure values. The right most column in the figure are clusters that did not have any $\leq 5:1$ merger in their entire histories.

tree diagnostic, respectively. The two horizontal dashed lines mark the upper and lower 20% of all clusters that have the highest and lowest substructure values. We can see that, indeed, recently merged clusters tend to have more substructure than relaxed clusters. However, the merging and relaxed populations overlap over a wide range of substructure values because of the large variation in substructures even for clusters at the same dynamical state. Therefore, there is not a clean cut to separate these two populations using the substructure measures.

In order to facilitate future studies in this area, we compute the completeness and contamination of merging and relaxed clusters defined by the substructure measures, assuming those identified using the cluster merger histories represent the true populations. We refer by 'completeness' to the fraction of merging/relaxed clusters found using substructure among the true merging/relaxed population, while 'contamination' is the fraction of clusters that are detected as merging/relaxed but are actually relaxed/merging. In Table 2.4 we summarize the results for different substructure measures. In the definitions using substructures, clusters that lie above/below the 20% thresholds are defined as merging/relaxed. In order to see how much the results are affected by the projection effect, we list the values obtained using information from both one and all projections. In the latter case, we select clusters by comparing the maximum value among three projections to the selection thresholds. In other

words, clusters are identified as merging if the most disturbed value among three projections is above the 20% threshold, and relaxed clusters must have their most disturbed value below the lower 20% threshold.

By comparing the numbers in Table 2.4, we find that in general P_2/P_0 and P_3/P_0 give similar results, and $P_{(1)}/P_0$ is not as useful as the other two power ratios. The centroid offset, having the greatest completeness and the least contamination, is the most successful one among all measures. When different aperture sizes are compared for the power ratios, the results using aperture sizes of 1 Mpc and R_{200} are similar, while using R_{500} is generally a little worse than the others both in completeness and contamination. When all three projections are considered, merging and relaxed clusters are better distinguished for all measures, with the values of completeness and contamination changed by $\sim 10-20\%$. The centroid offset, w, improves the most when all projections are used.

According to the above analysis, the centroid offset does a better job in distinguishing merging and relaxed clusters than the power ratios. This is probably because each individual power ratio is only sensitive to a certain type of substructure. They are more powerful when combined to distinguish between different morphological types (Buote & Tsai, 1995, 1996). The centroid offset, on the other hand, is a more general feature of all disturbed clusters. However, all the substructure measures have limitations. Their effectiveness is influenced by the viewing projection. More importantly, their values have a large variation even for clusters at the same dynamical state, as shown in Figure 2.13. Thus only $\sim 40\%$ of the true merging clusters are detected, and $\sim 25\%$ of the relaxed clusters. Among the detected clusters, $\sim 50\%$ of the "merging" clusters are actually relaxed, and $\sim 15\%$ of the "relaxed" clusters are actually merging. Therefore, although substructure measures are useful in distinguishing the dynamical state of clusters, caution is still required to interpret the results correctly.

2.5.3 Comparison with previous work

Several studies have explored the effect of clusters with different dynamical states on the $M-T_X$ scaling relation. Most previous works used substructure measures such as the power ratios and the centroid offset to quantify the dynamical state. The main difference in our study is that we directly analyze cluster merging histories to identify the recently merged clusters, which provides another line of evidence for our results in addition to those derived from the substructure measures.

O'Hara et al. (2006) investigated the effect of mergers and core structure on the X-ray scaling relations for both observed and simulated clusters. For the observed sample, they found that cool core clusters and clusters with less substructure exhibit a larger amount of

Table 2.4: Completeness and contamination of merging and relaxed clusters identified using power ratios and centroid offsets. Clusters lying above/below the 20% thresholds are defined as merging/relaxed. For the upper half of the table, the selection is based on the values of substructure measures in one projection, while for the bottom half, clusters are found by comparing the maximum value among three projections to the thresholds. See the text for details on the definition of completeness and contamination.

	P_2/P_0			P_3/P_0			$P_{(1)}/P_0$			w
	(1Mpc)	(R_{200})	(R_{500})	(1Mpc)	(R_{200})	(R_{500})	(1Mpc)	(R_{200})	(R_{500})	(R_{500})
Comp. of m.	39.6	38.2	31.3	36.8	34.7	28.5	22.2	21.5	23.6	47.9
Cont. of m.	54.0	55.7	63.7	57.3	59.7	66.9	74.2	75.0	72.6	44.3
Comp. of r.	22.8	23.2	21.8	22.2	23.4	21.6	19.3	19.3	18.0	23.9
Cont. of r.	12.8	11.2	16.8	15.2	10.4	17.6	26.4	26.4	31.2	8.94
	$(P_2/P_0)_{max}$			$(P_3/P_0)_{max}$			$(P_{(1)}/P_0)_{max}$			w_{max}
Comp. of m.	40.3	44.4	33.3	42.4	37.5	29.9	25.7	25.0	22.9	54.9
Cont. of m.	53.2	48.4	61.3	50.8	56.5	65.3	70.2	71.0	73.4	36.1
Comp. of r.	21.6	23.2	22.0	22.8	22.8	22.2	20.1	19.5	21.6	25.0
Cont. of r.	17.6	11.2	16.0	12.8	12.8	15.2	23.2	25.6	17.6	4.9

scatter. Their simulated clusters, on the other hand, have a tendency to have a larger amount of scatter for clusters with more substructure, though they argued that the evidence is weak. Since their simulations also do not include radiative cooling, we can compare directly with their results without worrying about other baryonic effects. We also find the same trend that merging clusters, which we have shown to have more substructure, have a larger amount of scatter. However, we further explore the origin of the intrinsic scatter and find a strong correlation with the halo concentration of clusters. We also show that the trend seen above is due to the fact that merging clusters have a larger variation in their concentrations.

Jeltema et al. (2008) studied the correlation between cluster substructures and cluster observables using hydrodynamical simulations with non-gravitational heating and cooling. Despite the difference of input baryonic physics in the simulations and the definition of T_X, they found no dependence on cluster substructures in the $M - T_{ew}$ relation when the true mass is considered. Although we find negative correlations between the scatter and some of the substructure indicators, the probabilities are not high. The lack of correlation supports their result. However, they reported that there is a significant trend for the relaxed clusters to have lower temperatures for their masses in the $M - T_{ew}$ relation measured within R_{500}, whereas we do not find any significant bias, and an opposite trend is found by Kravtsov et al.

(2006), Nagai et al. (2007a) and Kay et al. (2007). Taking the average relations between T_{ew} and T_X for merging and relaxed clusters from Nagai et al. (2007b), Jeltema et al. (2008) argued that the discrepancy cannot be explained by using different temperature definitions. However, we find that the bias between T_{ew} and T_X is larger for merging clusters than relaxed ones (see § 3.5), in the direction that can alleviate this discrepancy. Therefore, the difference between the conclusions reached by Jeltema et al. (2008) and the others regarding the offset of merging and relaxed clusters may be due to the use of T_{ew} instead of the spectroscopic temperature T_X.

On the other hand, Ventimiglia et al. (2008) have recently found significant negative correlations between the substructure measures and the scatter in the mass-temperature relation for their simulated clusters, both for the emission-weighted temperature T_{ew} and the spectroscopic-like temperature T_{sl}. They also found relative offsets between merging and relaxed clusters in the mean scaling relation, that is, merging clusters tend to be cooler than relaxed clusters of similar masses. As discussed in their paper, the different conclusion than Jeltema et al. (2008) may come from different implementations of feedback mechanisms. Although the trends can be explained by incomplete relaxation of merging clusters, which we also observed, we do not find a significant separation in the normalization of the $M - T_X$ relation between merging and relaxed populations, especially when the intrinsic scatter without cooling is largely contributed by the effect of halo concentration. Therefore, the main reason resulting in the differences is probably due to radiative cooling, as is suggested by the fact that it is included in all the studies which observed the relative offset. Since current simulations with radiative cooling tend to produce relaxed clusters with steeper temperature profiles than real clusters, the average temperature of relaxed clusters can possibly be biased high. This can explain why they found relaxed clusters hotter than expected while our results do not show any significant offset between relaxed and merging clusters in the $M-T_X$ relation.

2.6 Conclusions

Galaxy clusters are invaluable cosmological probes. Accurate measurement of cluster masses is crucial and often relies on the mass-observable relations. However, to constrain the cosmological parameters to the few percent level, the systematics and scatter in these relations must be thoroughly understood. In this work we investigate the sources of intrinsic scatter in the $M - T_X$ relation using a hydrodynamics plus N-body simulation of galaxy clusters in a cosmological volume. In order to compare directly to observations without worrying about

different definitions or systematics, we produced mock Chandra X-ray images using MARX and extracted the spectroscopic temperature T_X as observers do. Also, all the quantities in our analysis and discussions are measured within R_{500}, which is usually used for X-ray data. Radiative cooling and heating mechanisms are not included, since we would like to disentangle the scatter driven by the gravitational effects from other baryonic physics. We chose to focus on the $M-T_X$ relation for several reasons. First, it is less sensitive to resolution and to cooling and heating mechanisms than other scaling relations, such as the $L_X - T_X$ relation. Therefore, our results are still representative of reality even though the input physics is not complete. Second, the relative insensitivity to additional baryonic physics provides a window into better understanding of the physical origin of the scatter, despite our incomplete knowledge regarding the cooling and feedback mechanisms. Moreover, the intrinsic scatter in the $M-T_X$ relation is among the smallest of all the observed scaling relations. If one can further reduce it based on the knowledge of its physical origin, the $M - T_X$ relation will be extremely useful for cluster cosmology.

Our aim is to find out what determines the positions of clusters in the M_{500}–$T_{X,500}$ relation, in particular whether the intrinsic scatter is driven by recent merging activity or the overall assembly histories of clusters. We split our simulated cluster samples into merging and relaxed subgroups based on our merger tree analysis, and then we compare the distributions of the intrinsic scatter for individual subgroups. We also correlate the scatter with quantities that are related to the recent merging activity or cumulative cluster assembly histories, including the time since last merger, substructure measures, and the halo concentration. Here we summarize our findings.

We find a strong correlation between the scatter in the M_{500}–$T_{X,500}$ relation and the halo concentration. More concentrated clusters tend to lie below (cooler than) the mean relation, while puffier clusters tend to be hotter than expected for their masses. This is confirmed by the negative correlation between scatter and the formation lookback time of clusters, since it is well known that more concentrated clusters tend to form at earlier times. We showed that using this correlation, the scatter can be effectively reduced from 6.10% to 4.49%.

There is no bias in the M_{500}–$T_{X,500}$ relation between merging and relaxed clusters, but the amount of scatter for merging clusters is larger than that for the relaxed ones. This trend can be explained by the fact that merging clusters have larger variations in their concentrations than relaxed clusters.

When we correlate the scatter with the dynamical state of clusters, either the time since last merger or the substructure measures, there is a weak trend for recently merged clusters to be cooler, probably due to incomplete virialization of clusters that have just merged with a cool clump. However, statistically the influence of departure from hydrostatic equilibrium

of merging clusters is negligible. Possible reasons are discussed in detail in § 2.5.1.

There are significant deviations from lognormality of the distributions of scatter for our simulated clusters at both $z = 0$ and $z = 1$. This effect should be taken into account in future self-calibration studies to correctly interpret the obtained constraints on the cosmological parameters. Future simulation studies of larger volumes are needed in order to accurately characterize the distribution of scatter, including the tails of the distribution.

In conclusion, we find that when radiative cooling and feedback mechanisms are neglected, the intrinsic scatter in the M_{500}–$T_{X,500}$ relation is driven more by the variation in halo concentrations, or the overall assembly histories of clusters, than the recent merging events. Using an analytic approach, Balogh et al. (2006) investigated whether the amount of scatter in the observed $M - T_X$ and $M - L_X$ relations can be explained by the variations in halo concentrations or different entropy floors. Although they focused more on the scatter in the $M - L_X$ relation and showed that it requires a wide range of entropy floors, a significant portion of the scatter in the $M-T_X$ relation is determined by the range of halo concentrations predicted in their model. This is confirmed by our results since we have explicitly shown the strong correlation between the $M-T_X$ scatter with the halo concentration using a numerical simulation.

The lack of dependence of the scatter on the dynamical state of clusters is also seen by O'Hara et al. (2006) for observed clusters. They suggested that the scatter in the mass-observable relations is not dominated by recent mergers, but by the cooling-related core properties or probably the overall assembly histories of clusters. The latter relationship is indeed found in our simulation. As for the effects of radiative cooling, it has been shown to be a main source of intrinsic scatter in the $L_X - T_X$ relation (Allen & Fabian, 1998). Therefore, our next step is to include cooling and feedback mechanisms in the simulation to examine their individual influence on the scatter in the mass-observable relations.

Exploring the intrinsic scatter in the cluster scaling relations not only provides physical insights into the formation of galaxy clusters, but also has important implications for using clusters in cosmology. For example, the strong correlation with halo concentrations can be used for observed clusters to reduce the scatter in the scaling relations. Also, the weak influence of merging clusters is good news for cluster cosmology, because it implies that when deriving the scaling relations from the observed clusters, it is unnecessary to worry much about whether to include the unrelaxed systems or not. This is good because it is much more difficult to separate out the unrelaxed systems at higher redshifts. We expect that detailed studies of the intrinsic scatter in the scaling relations, not only in X-rays but also at other wavelengths, will continue to yield invaluable information both for cluster physics and cluster cosmology.

Chapter 3

Impact of structure and dynamical state on scatter in the SZ flux - mass relation[1]

3.1 Introduction

The evolution of structure in the Universe is thought to be a hierarchical process driven by gravitational instability acting on primordial density fluctuations. In this dynamical process, smaller clumps of matter merge to form bigger ones within a "cosmic web" of spatial structure incorporating matter within tenuous sheets, higher-density filaments, and large matter concentrations at the nodal points of the web. Clusters of galaxies occupy the top of the mass hierarchy, being the largest objects that have had time to collapse and form due to their self-gravity. Therefore, they are the most recent structures to form. Clusters have two very important features: they are very massive ($10^{14-15} M_{\odot}$) and populate the exponential tail of the mass function, which is sensitive to dark energy (Haiman et al., 2001), and because of their deep potential wells, they are "matter traps," preventing their internal constituents from escaping. The first aspect, combined with their young age, makes clusters an excellent probe of cosmology, being especially sensitive to dark matter and dark energy. The second makes clusters excellent laboratories for studying key astrophysics problems such as star and galaxy formation. Because of their central importance to both cosmology and astrophysics, clusters are being targeted by a variety of observational programs.

Clusters can be detected optically via starlight from their member galaxies, in X-ray due to thermal emission from hot gas, and using the thermal Sunyaev-Zel'dovich (SZ) effect (Sunyaev & Zeldovich, 1972). The SZ effect arises from the inverse-Compton upscattering of cosmic microwave background (CMB) photons by the hot electrons in a cluster (several keV), leading to an increase of the CMB brightness temperature at frequencies above about 250 GHz and a decrease at lower frequencies. This distortion of the Planck spectrum can be measured by sensitive, high-resolution CMB telescopes from the ground (Hincks et al., 2010; Staniszewski et al., 2009; Vanderlinde et al., 2010), and it is one of the best ways to find clusters at higher redshifts (Brodwin et al., 2010), since the SZ effect is (almost)

[1]This chapter is previously published in the Astrophysical Journal as Yang, H.-Y. K., Bhattacharya, S., & Ricker, P. M. 2010, ApJ, 725, 1124.

redshift-independent.

Upcoming surveys will detect clusters using their SZ signatures. However, instead of mass M, SZ surveys measure Y, the SZ Compton optical depth (the so-called y-decrement) integrated over a portion of a cluster's projected area. To obtain the cluster mass distribution from surveys, we need a so-called mass-observable (Y–M) relation. Using the mass distribution to constrain cosmological parameters requires that we know the errors introduced in this process, so we must also quantify the scatter and the bias in the mass-observable relation as functions of redshift (Lima & Hu, 2004, 2005; Cunha & Evrard, 2010).

Because of the exponential shape of the cluster mass function, scatter in the X–M relation (for any observable X that is positively correlated with M) boosts the number density of clusters observed in logarithmic bins of X, as the overall number of lower-mass clusters scattering to higher values of X far exceeds the number of high-mass clusters scattering in the opposite direction. As shown in Bhattacharya et al. (2011), a few percent systematic error in mass, which can arise due to bias in the X–M relation, leads to a significant difference in the tail of the mass function. Thus, misestimating the scatter and bias in the X–M relation can lead to biases in the cosmological constraints (e.g. Randall et al., 2002; Wik et al., 2008). Moreover, previous work forecasting cosmological constraints based on cluster surveys has assumed the distribution of scatter to be lognormal (Lima & Hu, 2005; Cunha, 2009). If this assumption were invalid, it would also lead to biases in the results (Shaw et al., 2010a).

Understanding the physical sources of scatter can help us to reduce this scatter and improve the mass estimates. For example, the use of core-excised quantities reduces the effects of cool cores in clusters and hence also the large scatter in the X-ray luminosity-temperature (L_X–T_X) relation (Allen & Fabian, 1998) or the L_X–M relation (Mantz et al., 2010a). Using the halo concentration as a third parameter can reduce the scatter in the T_X–M relation (Yang et al., 2009). Combinations of observables with oppositely trending scatter can also help, as shown by the tight correlation between the X-ray counterpart of the Compton y-parameter, $Y_X \equiv M_{\rm gas}T_X$, and mass (Kravtsov et al., 2006). These examples illustrate the possibility of obtaining better mass estimates if our knowledge of the physical origin of scatter can be improved.

Because of spatial resolution constraints, the Y–M relation has been studied using two types of hydrodynamic simulations. One type includes only adiabatic physics but has sufficient statistics to quantify the scatter and the bias in the mass-observable relation (Hallman et al., 2007). The other includes extra physics such as radiative cooling, star formation, and supernova feedback (Nagai et al., 2007a) or feedback from quasars (Bhattacharya et al., 2008), but with limited statistics (16 and 10 halos, respectively, in the cited references). Another approach is to include gas physics using a semianalytic gas prescription in halos

obtained from a dark-matter only (DMO) simulation (e.g. Bode et al., 2007, 2009; Shaw et al., 2010b). In particular, Shaw et al. (2008, 2010a) have quantified the Y–M relation and its non-gaussianity using the "DMO+semianalytic" approach. As pointed out by Shaw et al. (2008), the hydrodynamic simulations tend to show slightly different scatter compared to the "DMO+semianalytic" case especially for overdensities $\sim$500 times the critical density of the universe. These differences need to be understood. Only recently have there been attempts to incorporate extra baryonic physics into a large cosmological simulation to study the intrinsic variances in the scaling relations. For instance, Stanek et al. (2010) have used resimulations from the Millennium Gas Simulation with gas dynamics treated in both gravity-only and cooling plus preheating prescriptions to study the scaling relations and correlations among cluster structural properties and observables in X-ray and SZ.

In this study we begin a systematic investigation of the physical sources of the intrinsic Y–M scatter and their impact on the form of scatter for the purpose of improving our knowledge of both cluster formation and cluster cosmology. We use cosmological simulations to obtain clusters with sufficient statistics and to incorporate hydrodynamic processes including interactions with large-scale environment, variations in cluster structures, and merger-induced shock heating and departure from hydrostatic equilibrium. Since we would like to focus on the scatter driven by gravitational effects only, radiative cooling and heating mechanisms are not included. In this work, we examine the assumption of lognormal scatter, which has important implications for self-calibration studies of cluster surveys. We investigate various sources of scatter, such as halo concentrations, dynamical state, and cluster morphology, by correlating the scatter with quantitative measures of each source. We show that these correlations can be used to reduce the scatter and tighten the scaling relation. We also discuss possible applications and issues when combining SZ and X-ray scaling relations.

The outline of this study is as follows. Since this study is based on the same simulation as in the previous chapter, we will refer the readers to Chapter 2 for details of the simulation and the merger tree analysis. In § 3.2 we will give a brief overview of the SZ effect, and how we create idealized cluster samples to disentangle the sources of scatter. The Y–M relation and the form of its scatter are presented in § 3.3. Possible sources of scatter are investigated in § 3.4. In § 3.5 we explore the possibility of combining SZ and X-ray scaling relations to improve cluster mass estimates. Finally, we discuss our results and give the conclusions in § 3.6.

3.2 Method

3.2.1 Sunyaev-Zel'dovich effect

The thermal Sunyaev-Zel'dovich effect is caused by inverse Compton scattering of CMB photons off the hot electrons inside galaxy clusters. Assuming that relativistic corrections are small, the resulting distortion of the CMB temperature can be written as $\Delta T/T_{CMB} = g_\nu(x)y$ where $g_\nu(x) = x(\coth(x/2) - 4)$ with $x = h\nu/k_B T_{CMB}$, k_B is the Boltzmann constant, ν is the frequency of observation, and T_{CMB} is the mean CMB temperature at the current epoch. Here y is the Compton y-parameter, which can be written as

$$y = \frac{k_B \sigma_T}{m_e c^2} \int n_e(l) T_e(l) dl, \tag{3.1}$$

where $n_e(l)$ is the electron density profile, σ_T is the Thomson scattering cross section, and the integration is along the line of sight, which is defined to be the x-direction in the simulation box.

Note, however, that the observable is the integral of the temperature distortion over the cluster's projection onto the sky. For a cluster at redshift z, it is given by

$$Y(M, z) = \frac{1}{d_A(z)^2} \frac{k_B \sigma_T}{m_e c^2} \int n_e(l) T_e(l) dV, \tag{3.2}$$

where $d_A(z)$ is the angular diameter distance to the cluster, and the integration is over the volume of the cluster. In the literature, sometimes the factor $1/d_A^2$ is omitted from Eq. 3.2. In this study, when we omit the factor $1/d_A^2$, we denote the temperature distortion as $Y(M)$; otherwise it is denoted as $Y(M, z)$. Note that $Y(M, z)$ is dimensionless, while the units of $Y(M)$ are Mpc^2. In the following sections in which we investigate the distribution and origin of intrinsic scatter, we adopt $Y(M)$ unless explicitly stated otherwise.

Following the convention in the literature, we denote Y_Δ as the SZ flux integrated out to certain overdensity radius R_Δ. In the simulation box, cell-averaged information about the gas density and temperature is stored for each grid cell. Thus for each cluster the integrated SZ distortion is calculated using

$$Y_\Delta(M, z) = \frac{1}{d_A(z)^2} \frac{k_B \sigma_T}{m_e c^2} \sum_{i, r_p \leq R_\Delta} n_{e,i} T_{e,i} \Delta V_i, \tag{3.3}$$

where the summation is over all the grid cells across the cluster volume within a cylinder of projected radius R_Δ, and ΔV_i is the volume of each grid cell.

3.2.2 Idealized Cluster Samples

One of our main goals is to investigate the possible sources of intrinsic scatter, including the variations due to concentration, departure from hydrostatic equilibrium, merger boosts, and cluster morphology. In order to distinguish the contribution from each source, we construct a set of idealized cluster samples with different assumptions. Starting from a sample with the most possible constraints, we add one source of scatter at a time. By comparing the scatter of the idealized samples and the simulated sample, we can tell whether the scatter can be successfully reconstructed, or yet other sources still need to be found.

To this end we construct five idealized samples, going from sample A, with the most constraints, to sample E, which includes the most sources of variation. For sample A, only the cluster masses are taken from the simulation. Given the mass, the halo concentration c is computed using the best-fit c–M relation from Shaw et al. (2006). With the mass and halo concentration, the total density and gas density are assigned using the NFW profile (Navarro, Frenk, & White 1995; 1996, hereafter NFW) and a core-softened NFW profile (Sijacki et al., 2007), respectively. In the core-softened NFW profile, the core radius is set to be 0.02 times the virial radius, and the gas fraction, $f_g = 0.12$, is also fixed. The pressure and temperature profiles are then computed assuming hydrostatic equilibrium (HSE). Finally, dark matter particles and zone-averaged cell quantities are assigned according to the profiles, assuming spherical symmetry. They are stored using the same file format as the simulated clusters, allowing them to be analyzed in the same way as the simulated clusters. Any scatter in the resulting Y–M relation can only be due to particle shot noise, finite cell resolution, and the simulated observation procedure.

Sample B is generated using a similar procedure, except that the c–M relation is assumed to have a lognormal distribution with a dispersion of 0.22 (Jing, 2000; Bullock et al., 2001; Dolag et al., 2004; Shaw et al., 2006). In other words, the variation in concentration should be the only additional source of Y–M scatter for sample B.

In addition to the variation in concentration, clusters in sample C are allowed to depart from HSE due to pressure support from random gas motions after mergers. For each cluster, we compute the gas velocity dispersion's radial profile from the simulation and include an extra pressure term, $P_{\rm rand} = \rho\sigma^2$, in the HSE equation for computing the thermal pressure. In this way, we are effectively taking into account the incomplete virialization after merger events as another source of scatter.

With sample D, we model the effect of mergers by including not only incomplete relaxation but also the merger boosts due to shock heating (Ricker & Sarazin, 2001; Poole et al., 2007). Therefore, we extract the time histories of mass and integrated SZ flux during

Table 3.1: Summary of models used for constructing the idealized cluster samples.

Sample	Assumptions/Constraints	Sources of Variation[1]
A	Spherical + f_g + HSE[2] + $c(M)$	None
B	Spherical + f_g + HSE	c
C	Spherical + f_g + No Merger Boost	c + $P_{\rm rand}$
D	Spherical + f_g	c + $P_{\rm rand}$ + Merger Boost
E	Spherical	c + $P_{\rm rand}$ + Merger Boost + f_g
S	Simulated	All
SS	Simulated + Spherical	All - Morphology

[1] All include scatter resulted from particle shot noise, finite cell resolution, and the simulated observation procedure.

[2] Hydrostatic equilibrium enforces no merger boost and no random gas motion.

mergers from the ideal merger simulations in Poole et al. (2007) and apply a boost in Y to each idealized cluster using the actual times since last merger in the simulation and the mass ratios of those mergers. Note that the time evolution of mass from Poole et al. (2007) is measured for overdensity $\Delta = 500$, but the integrated SZ flux is only available for $\Delta = 2500$. Thus the Y–M scatter of sample D should be considered as an upper limit to the effects of merger boosts.

Sample E adds variation in the gas fraction by using the actual gas fraction computed for each simulated cluster. Sample E essentially includes all possible sources of scatter investigated in this study except the effect of cluster morphology. In § 3.4.5 we will compare results from these idealized samples to the simulated clusters (Sample S). Because the idealized samples are all constructed under the assumption of spherical symmetry, we derived another sample (Sample SS) using gas profiles directly extracted from the simulated clusters, such that it includes all sources of scatter except the morphological effect. These models are summarized in Table 3.1.

3.3 The Y–M scaling relation

3.3.1 Normalization and Slope

For each simulation output between $z = 0$ and $z = 1.5$, we derive the $Y_\Delta - M_\Delta$ relation for all clusters with $M_{500} \geqslant 2 \times 10^{13} M_\odot$ (619 clusters at $z = 0$ and 223 clusters at $z = 1$) and

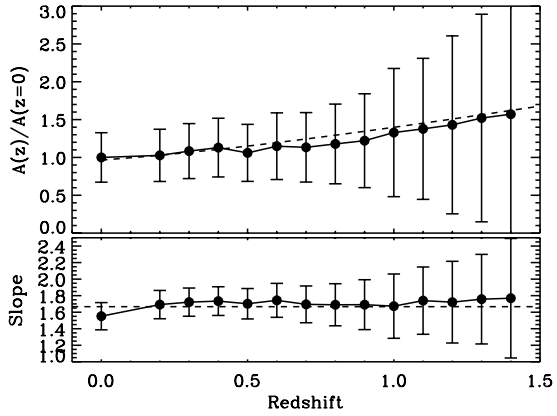

Figure 3.1: Normalization and slope of the Y–M relation as functions of redshift. The dashed lines are the self-similar prediction.

fit it with a power law of the form

$$\bar{Y}_\Delta = 10^{-6} A_{14}(z) \left(\frac{M_\Delta}{10^{14} h^{-1} M_\odot} \right)^\alpha , \tag{3.4}$$

where the normalization at $10^{14} h^{-1} M_\odot$ in units of 10^{-6}, A_{14}, and slope α are found by fitting the data points using a Levenberg-Marquardt algorithm. An overdensity of $\Delta = 500$ is adopted throughout this work.

The normalization (relative to the value at $z = 0$), slope, and scatter as functions of redshift are plotted in Figure 3.1. As also found in previous adiabatic simulations (da Silva et al., 2004; Motl et al., 2005), the evolution of the normalization and slope is consistent with the self-similar prediction, $\alpha = 5/3$ and $A_{14}(z) \propto E(z)^{2/3}$, where $E(z) = [\Omega_{m0}(1 + z)^3 + \Omega_{\Lambda 0}]^{1/2}$, though we cannot rule out the case of no evolution because the small number of high-mass clusters at higher redshift limits the constraining power of the data. We find $A_{14}(z = 0) = 5.43 \pm 0.47$, which is in agreement with the adiabatic runs in Nagai (2006) ($A_{14}(z = 0) = 4.99, f_b = 0.14$) and Shaw et al. (2008) ($A_{14}(z = 0) = 4.07, f_b = 0.11$) after taking into account the differences in the baryon fraction used in the simulations ($f_b = 0.167$ in our simulation).

3.3.2 Scatter in the Y–M relation

The RMS scatter around the best-fit relation is defined for N clusters as

$$\sigma_{YM} = \left[\frac{\Sigma_{i=1}^{N}(\log Y_i - \log \bar{Y}_i)^2}{N-1}\right]^{1/2}, \tag{3.5}$$

where Y_i is the measured flux of the ith cluster, and $\bar{Y}_i$ is the flux predicted by the best-fit relation for that cluster. Hereafter, we use the notation

$$\delta \log Y \equiv \log Y - \log \bar{Y} \tag{3.6}$$

for the deviation from the mean relation for each cluster. For each redshift from $z = 0$ to $z = 1$, we compute the RMS scatter for 5 mass bins and plot the result in Figure 3.2 (the data for some of the redshifts are omitted for clarity). The scatter is $\sim 5 - 15\%$, consistent with previous findings (e.g. Nagai, 2006). Moreover, we find that in general the scatter decreases with both mass and redshift. We fit the scatter using the functional form

$$\sigma(M, z) = A \log M + B \log(1 + z) + C, \tag{3.7}$$

where the best-fit coefficients are $A = -7.06 \pm 0.28$, $B = -11.20 \pm 0.81$, and $C = 7.70 \pm 0.19$. The mass dependence may be due to increasing non-lognormality of the scatter when considering low-mass clusters (see § 3.3.3 for details). The redshift evolution may be understood by considering the self-similar model, in which all quantities for collapsed objects can be expressed in terms of the characteristic mass scale, $M_\star \propto (1+z)^{-6/(n+3)}$, where n is the spectral index of the scale-free primordial power spectrum, $P(k) \propto k^n$ (Kaiser, 1986). Therefore, Eq. 3.7 is equivalent to the expression $\sigma = A' \log(M/M_\star) + B'$. Note that Eq. 3.7 is the first attempt in the literature to quantify the scatter using a functional form of mass and redshift. This expression should be useful for future studies that require assumptions about the form of scatter.

3.3.3 Non-lognormal scatter

Since the SZ flux is only proportional to the first power of gas density, it is sensitive to the contribution from low-density gas clumped along the line of sight to but not associated with a cluster. This is in contrast to the X-ray luminosity, which is proportional to the square of gas density. For this reason the Y–M relation has been found to have a high-scatter tail in the distribution of its scatter (White et al., 2002; Hallman et al., 2007). Since any

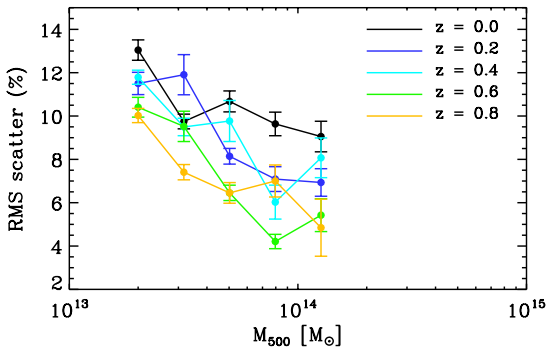

Figure 3.2: RMS scatter as a function of M_{500}. Different curves are for different redshifts. In general, the scatter decreases with both mass and redshift. See Eq. 3.7 for the best-fit relation.

deviations from the lognormal scatter would bias cosmological constraints based on cluster counts (Shaw et al., 2010a), we would like to examine whether the form of the log scatter can be well approximated by a Gaussian distribution, or whether generalizations of the parametrization need to be considered.

A purely Gaussian distribution can be described exactly using only its mean value μ and variance σ^2:

$$G(x) = \frac{1}{\sigma\sqrt{2\pi}} \exp\left[-\frac{(x-\mu)^2}{2\sigma^2}\right]. \tag{3.8}$$

A nearly-Gaussian distribution can be approximated using the Edgeworth expansion (e.g. Bernardeau & Kofman, 1995; Blinnikov & Moessner, 1998),

$$\tilde{G}(x) \approx G(x) - \frac{\gamma}{6}\frac{d^3G}{dx^3} + \frac{\kappa}{24}\frac{d^4G}{dx^4} + \frac{\gamma^2}{72}\frac{d^6G}{dx^6}, \tag{3.9}$$

which is parametrized by four moments – the mean and the variance describing the Gaussian distribution, plus the skewness (γ) and the kurtosis (κ) describing the deviation from gaussianity. The skewness is defined as

$$\gamma = \frac{\langle (x-\mu)^3 \rangle}{\sigma^3} \tag{3.10}$$

and the kurtosis as

$$\kappa = \frac{\langle (x-\mu)^4 \rangle}{\sigma^4} - 3. \tag{3.11}$$

We compute the skewness and kurtosis of the Y–M scatter for clusters at $z = 0$ above different mass thresholds and plot the results in Figure 3.3. The error bars represent the

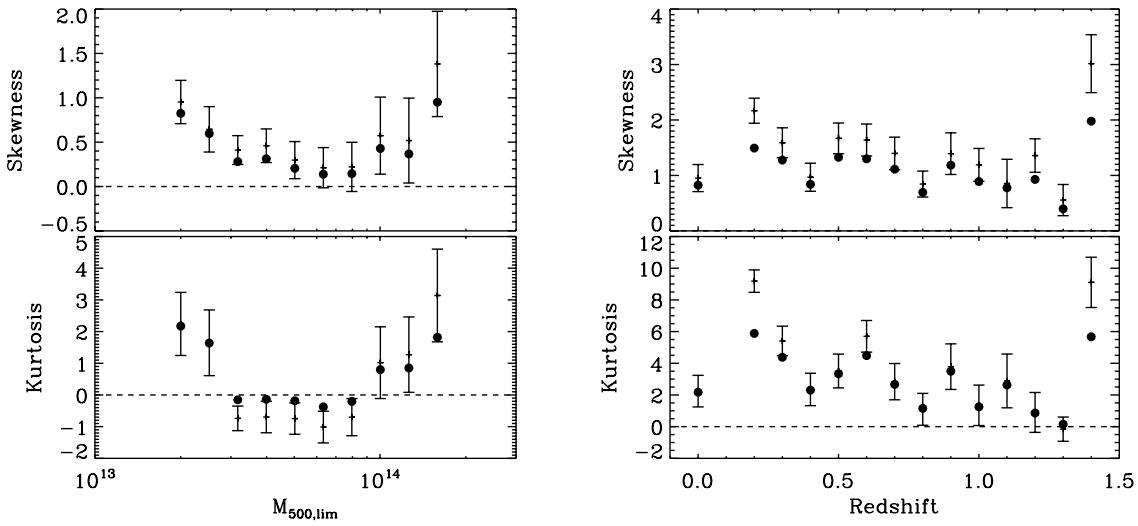

Figure 3.3: Skewness and kurtosis of the Y–M scatter for simulated clusters at $z = 0$ as functions of limiting mass (left) and redshift (right). See the text for the definition of error bars.

uncertainty due to finite sample size and are estimated using 10^3 Monte-Carlo realizations of random sampling from a nearly-Gaussian distribution given the measured skewness and kurtosis as in Eq. 3.9. Note that because of finite sample size the measured skewness and kurtosis would underestimate the intrinsic values of the underlying distribution. This bias is represented by the offset between the data points and the middle points of the error bars.

We find that the scatter is non-lognormal with positive skewness and kurtosis when including only massive clusters ($M_{500,\mathrm{lim}} \gtrsim 10^{14} M_\odot$) or when more and more low-mass clusters are included ($M_{500,\mathrm{lim}} \lesssim 5 \times 10^{13} M_\odot$). Due to the limited number of clusters at the high-mass end, the log scatter there is expected to follow Poisson statistics and deviate from a Gaussian form. For the lower mass range, on the other hand, we find that there is a tail toward positive values in the distribution of scatter, which increases the skewness and kurtosis. By visual inspection of clusters in the tail, we find that these objects happen to have elongated shapes or clumped gas along the line of sight. Since less massive clusters are more likely to be surrounded by gas with mass comparable to their own, this effect becomes more important for lower-mass clusters. We will further address this point in § 3.4.3. For other redshifts, the level of non-lognormality is also non-negligible, as shown in Figure 3.3. The median skewness and kurtosis are 1.43 and 4.21, respectively.

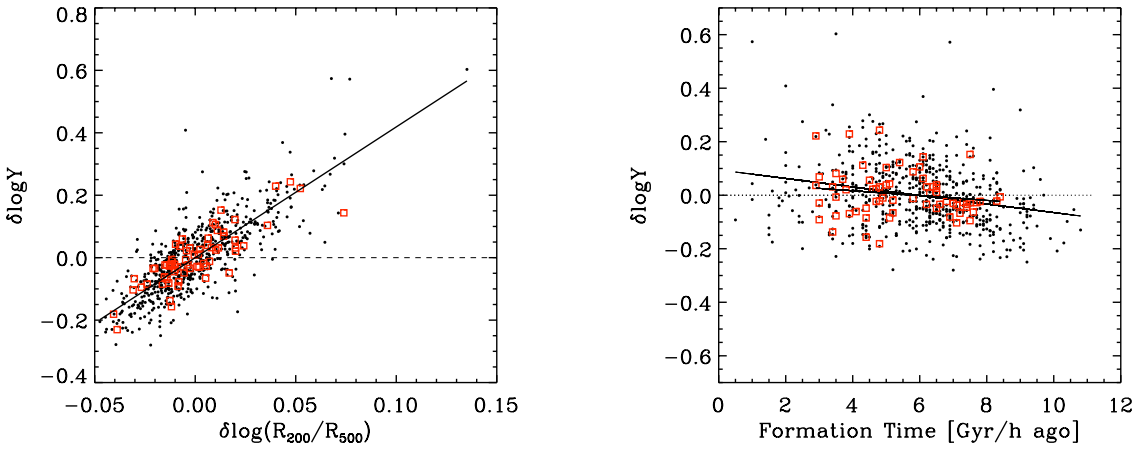

Figure 3.4: *Left*: Y–M scatter versus (R_{200}/R_{500})–M scatter at $z = 0$, where R_{200}/R_{500} is a monotonically decreasing function of halo concentration. Correlation coefficient is 0.775. *Right*: Y–M scatter versus formation time at $z = 0$. Correlation coefficient is -0.244. Clusters with $M_{500} \geqslant 10^{14} M_{\odot}$ are plotted using open squares.

3.4 Sources of scatter

We now investigate the physical origin of the intrinsic scatter for the purpose of understanding the above trends and reducing it for better mass estimates. Possible sources of scatter in our simulation include halo concentration, dynamical state, and cluster morphology. We examine each effect by correlating the scatter with each individual source for clusters at $z = 0$. We show that the scatter can be reduced by choosing appropriate measures of each effect. At the end of this section we compare the percentage contribution from each source using the idealized cluster samples described in § 3.2.2.

3.4.1 Concentration

The concentration of a dark matter halo is usually defined as the ratio between the virial radius and the NFW scale radius, i.e., $c \equiv R_{\rm vir}/R_s$. The concentration parameter characterizes the density inside the core region of a halo and reflects the mean density of the universe when the halo collapsed. Thus halos formed earlier in time tend to be more concentrated (NFW 1997; Wechsler et al. 2002). By testing the correlation of Y–M scatter with scatter in the concentration parameter, we are effectively probing the influence of cluster formation history.

We choose to use the parameter R_{200}/R_{500} instead of the original halo concentration parameter c because it has two advantages. The first is that it avoids introducing the

uncertainty of fitting an NFW profile, especially for less massive clusters, since the fitting is very sensitive to the grid resolution in the central region of a cluster. Moreover, our analyses involve not only relaxed clusters but also merging ones, for which R_{200}/R_{500} is actually better-defined than c, since an NFW profile would yield a poor fit.

Figure 3.4 (left panel) shows a strong positive correlation between scatter in the Y–M relation and scatter in the (R_{200}/R_{500})–M_{500} relation. The correlation coefficient is 0.64, with a probability of zero given by the Spearman Rank-Order Correlation test (Press et al. 1992, §14.6; probability of one means no correlation). To ensure that this result is not biased by the lower-mass clusters whose R_{500} values are close to the resolution of the simulation, we raised the mass threshold to $M_{500} \geqslant 10^{14} M_{\odot}$ and found that the result is robust for these well-resolved systems (shown as the open squares in Figure 3.4). Note that we correlate with $\delta \log(R_{200}/R_{500})$ instead of the raw value of R_{200}/R_{500} because the latter is a function of cluster mass. By doing so we exclude the effect of different cluster masses, focusing on the variation in halo concentrations. R_{200}/R_{500} is a monotonically *decreasing* function of the halo concentration parameter (see Yang et al. (2009) for derivation). Therefore, for clusters with similar masses, more concentrated clusters tend to lie under the mean Y–M relation, while the "puffier" clusters tend to scatter high.

Since halo concentration is related to cluster formation time, we can test the above trend by checking the correlation of Y–M scatter with the formation times derived from the mass assembly histories of our simulated clusters. The formation time here is defined as the time when the cluster first exceeds half of its final mass. As expected, we find that clusters that formed earlier (thus with higher concentrations) tend to scatter low (see right panel of Figure 3.4). The correlation is not as tight as the one with the halo concentrations. This is due to the fact that the correlation between the halo concentration and the cluster formation time itself has a very large scatter, and also that the variation in halo concentrations cannot be fully accounted for by the variation in cluster formation time (Neto et al., 2007). But the direction of the correlation with cluster formation time is consistent with the correlation with halo concentration.

To explain the correlation between the Y–M scatter and the concentration, recall the virial theorem for the simplest case of an isolated system: $2K + U = 0$, where K and U are the total kinetic and gravitational binding energies of the system, respectively. In general one can write

$$\frac{k_B T}{\mu m_p} \propto \frac{GM}{R}, \tag{3.12}$$

where μ is the mean molecular mass of the gas, m_p is the mass of a proton, and T, M, and R are the virial temperature, mass, and radius of the system, respectively. Together with

the definitions of the SZ flux (Eq. 3.2) and $M = \frac{4}{3}\pi R^3 \bar{\rho}$, one can derive

$$Y \propto M_{gas} T \propto f_g M^{5/3}. \tag{3.13}$$

Note that the above relations are for virial quantities of a cluster *as a whole*, but mass-observable relations are often measured using a certain aperture size, R_Δ. The relation between the virial and overdensity quantities depends on individual cluster profiles, which are determined by the halo concentration and how the gas is distributed on top of the dark matter potential (e.g. equation of state of gas). Therefore, the normalization, and thus the scatter, of the Y_Δ–M_Δ relation is a function of halo concentration and gas properties.

It is also important to note that, from the above derivation, the direction of the correlation between the scatter and concentration is dependent on the gas properties. Our result shows that less concentrated clusters tend to scatter high, i.e., have higher pressure than clusters of similar masses. Observationally, Comerford et al. (2010) has also found a similar anti-correlation between the X-ray temperature-mass scatter and strong lensing concentration. This may be attributed to the fact that less concentrated clusters have larger scale radii, and hence when comparing with clusters of the same M_Δ or the same aperture size R_Δ, their ratios R_Δ/R_s are smaller, which means the observable integrated within R_Δ would be greater. However, different simulations can have different directions of correlation depending on the input gas physics. For example, Shaw et al. (2008) also found a correlation between the scatter and concentration, but in the opposite direction. The difference may be due to different gas physics included in their models. In principle, by assuming a particular gas model the constant of proportionality in Eq. 3.13 can be computed exactly. Ascasibar et al. (2006) has done this exercise assuming a polytropic equation of state for the gas. According to their calculation, the coefficient in the T–M relation (as in Eq. 3.12; inverse of the Y_{MT} in their Eq. 17) decreases with concentration for a polytropic index of $\gamma_p = 5/3$. As γ_p decreases, the dependence becomes weaker and then the direction is reversed. Since including extra baryonic physics effectively works to decrease γ_p (e.g. *for fixed mass and concentration*, both changes yield a shallower temperature profile, see also Figures 2 and 3 in Ostriker et al. (2005)), this may explain why the dependence on concentration can be different between models with different input gas physics. Note, however, that in reality the situation can be even more complicated because a constant γ_p may not be valid for all gas models (Kay et al., 2004).

The strong correlation in Figure 3.4 suggests that the variation in halo concentrations contributes a significant amount of the intrinsic scatter in the Y–M relation. Using this strong correlation it is possible to adjust for the dependence of SZ flux on cluster concen-

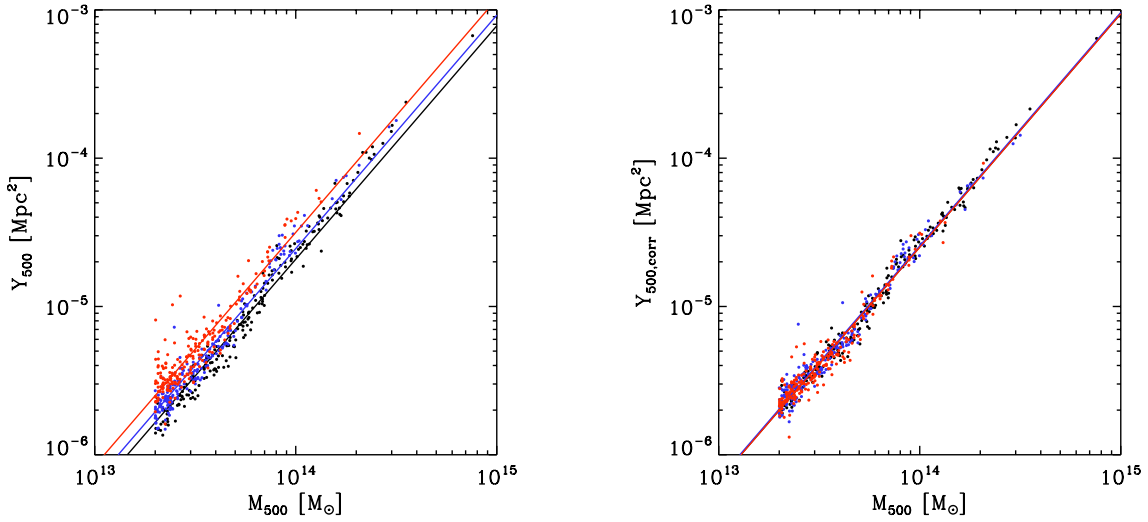

Figure 3.5: *Left*: The Y–M relation plotted for clusters having different values of concentration at $z = 0$. The 1/3 percentiles with the highest, intermediate, and lowest values of concentration are plotted using black, blue, and red symbols, respectively. *Right*: The Y–M relation after correction for the dependence on concentration using Eq. 3.14.

trations. We use $\delta \log(R_{200}/R_{500})$ for each cluster to calculate its expected $\delta \log Y$ from the best-fit relation, $(\delta \log Y)_{\rm exp} = 7.167 \times \delta \log(R_{200}/R_{500})$. We then subtract this $(\delta \log Y)_{\rm exp}$ from the measured SZ flux to obtain a corrected flux,

$$(\delta \log Y)_{\rm corr} = \delta \log Y - (\delta \log Y)_{\rm exp}. \tag{3.14}$$

The Y–M relations before and after correcting for concentration are shown in Figure 3.5. We find that after removing the effect of halo concentration, the RMS scatter decreases from 12.07% to 7.34% (i.e. by 38.9%). This method was proposed by Yang et al. (2009) to tighten the X-ray temperature-mass relation and has been successfully applied to observed strong lensing clusters (Comerford et al., 2010). In addition to strong lensing, the NFW concentration can also be measured via weak lensing, X-ray emission, etc. (Comerford & Natarajan, 2007; Mandelbaum et al., 2008; Buote et al., 2007, and references therein), although one has to be careful about systematics of each method and when combining different measurements. In fact it can be generalized to any observable other than concentration. That is, if there exists any variable X whose mass scatter $\delta \log X$ is known and correlates with $\delta \log Y$, then given the best-fit correlation $(\delta \log Y)_{\rm exp} = \alpha \times \delta \log X$, the Y–M scatter can be reduced in a similar way using Eq. 3.14 to remove the effect of X from the scatter. Therefore, this method can be a powerful way to reduce the observed mass-observable scatter and obtain

better mass estimates.

3.4.2 Dynamical state

Another possible origin of the Y–M scatter is cluster dynamical state. Cluster mergers are among the most energetic events in the universe. Shock heating and departure from hydrostatic equilibrium during mergers can drive clusters away from the mean scaling relations. Ideal merger simulations (Ricker & Sarazin, 2001; Poole et al., 2007) have shown that the effect of shock heating to boost the SZ and X-ray observables to values a few times higher than the pre-merger values. Studies that combine the amount of boosting predicted by these simulations with extended Press-Schechter merger trees (Randall et al., 2002; Wik et al., 2008) show that the boosting effect can bias estimates of cosmological parameters such as σ_8 and Ω_m. The other effect of mergers is departure from hydrostatic equilibrium. Before the gas within a merger is completely virialized, the pressure support from random gas motions can contribute $\sim 10-20\%$ of its thermal pressure (Rasia et al., 2006; Lau et al., 2009). Thus the thermal pressure and hence the SZ flux of unrelaxed systems is expected to be smaller than that of relaxed systems of similar masses. These previous studies are primarily based on small cluster samples. Therefore, our aim is to investigate how merger events *statistically* influence the cluster scaling relations.

If the scatter were dominated by the boosting effect of cluster mergers as described above, then one would expect to find merging clusters to preferentially lie above the mean relation. However, if during mergers the departure from hydrostatic equilibrium due to non-thermal pressure support were dominant, mergers would tend to scatter low. In order to see which effect is more prominent, we correlate the Y–M scatter with the time since last merger (Figure 3.6, left panel). Substructure measures such as centroid offset (Mohr et al., 1995) and power ratios (Buote & Tsai, 1995, 1996) are often used to quantify departures from equilibrium in clusters. We compute the centroid offset and power ratios for the simulated clusters using the same definition as in Yang et al. (2009). The right panel of Figure 3.6 shows the correlation with one of the power ratios, P_2/P_0. Based on the Spearman Rank-Order Correlation test (Press et al. 1992, §14.6), both correlations are weak (with a small correlation coefficient) but significant (with a high probability), in the direction that more disturbed clusters tend to scatter low. This implies that during mergers the incomplete virialization may be the more important factor in driving the scatter than the shock heating effect. However, the fact that these two effects operate in opposite directions may be the reason why there is not a clear trend with merger activities. Moreover, a number of factors can dilute the shock boosting effect, such as the small chance of finding mergers in progress, capturing

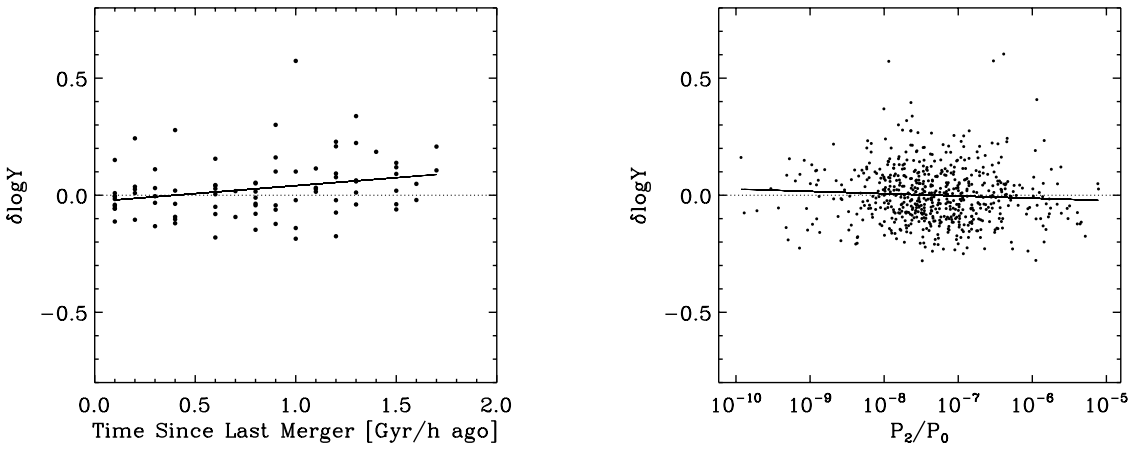

Figure 3.6: *Left*: Y–M scatter versus time since last merger for major mergers at $z = 0$. The correlation is statistically significant but weak (correlation coefficient of 0.299; probability of no correlation of 0.006). *Right*: Y–M scatter versus one of the power ratios, P_2/P_0. Correlation coefficient is -0.091; probability of no correlation is 0.023.

the shocks within an overdensity radius at the right projection and at the right moment during a merger's transient boost, and the fact that merging clusters tend to move along the scaling relations because their masses also increase at the same time their observables increase, as found also by Wik et al. (2008) and Kravtsov et al. (2006) (see Yang et al. (2009) for an extensive discussion).

Do mergers bias the Y–M relation due to incomplete virialization? To answer this question, we plot the normalized distributions of the Y–M scatter for relaxed and merging clusters in Figure 3.7 and use the Wilcoxon Rank-Sum (R-S) test and the F-variance (F-V) test to see whether these two populations have significantly different mean values or variances, respectively. A value smaller than 0.05 (for a significance level of 5%) returned by these tests is commonly adopted to indicate a significant difference between two populations. We find that their mean values do not differ significantly, but mergers have a wider distribution compared to relaxed clusters (with significance 0.014). Therefore, although mergers do not tend to bias the scaling relation, they do have a greater amount of scatter than relaxed clusters. If merging (relaxed) clusters are chosen to be those within the quartile with the highest (lowest) substructure measures, similar trends with significant probabilities are found for 9 out of 21 substructure measures (P_2/P_0, P_3/P_0, and the centroid offset W measured from different viewing directions and varying aperture sizes). We find that including only the merging clusters would result in $\sim 15 - 45\%$ greater scatter than when only relaxed clusters are taken into account, consistent with previous findings (Shaw et al., 2008). Note however

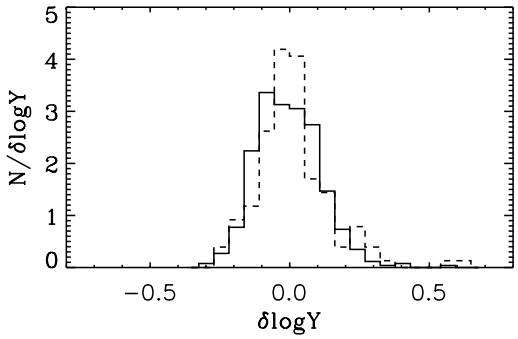

Figure 3.7: Normalized distribution of the Y–M scatter for relaxed (solid) and merging (dashed) clusters at $z = 0$. According to results from significance tests, mergers do not have a bias but do have a larger dispersion with respect to the relaxed clusters.

that separating mergers from relaxed clusters does not reduce the skewness or kurtosis of the scatter distribution, which suggests that the non-lognormality has causes other than mergers (see § 3.4.3).

3.4.3 Morphology

Despite the spherical symmetry that theoretical models usually assume, both simulations (Warren et al., 1992; Cole & Lacey, 1996; Jing & Suto, 2002; Bailin & Steinmetz, 2005; Kasun & Evrard, 2005) and observations (e.g. Basilakos et al., 2000) have shown that clusters are triaxial (or elliptical when projected) rather than simple spheres, even for relaxed clusters. How the gas is distributed in the cluster potential well should vary depending on the axes ratios of the cluster. Moreover, viewing a triaxial cluster from different angles should also yield different observed quantities integrated along the line of sight. Both these factors can contribute to the Y–M scatter.

In order to explore the impact of morphology, for each simulated cluster we find the orientation of the principal axes by diagonalizing the moment of inertia tensor, $I_{\alpha\beta} = m_i \Sigma_i r_i^\alpha r_i^\beta$, where the summation is over all the particles and cells in the cluster, m_i is the mass of a particle or a gas cell, and r_i^α is the x, y, or z component of the distance from the cluster center of mass. The lengths of the major, intermediate, and minor axes, denoted as a, b, and c, are found by finding the intercepts of the axes with the isodensity surface having overdensity $\Delta = 200$. The angles θ_α are defined to be the angles between the major axis and the directions of projection ($\alpha = x, y, z$; note that the x-direction is the projection used for all the analyses in this study).

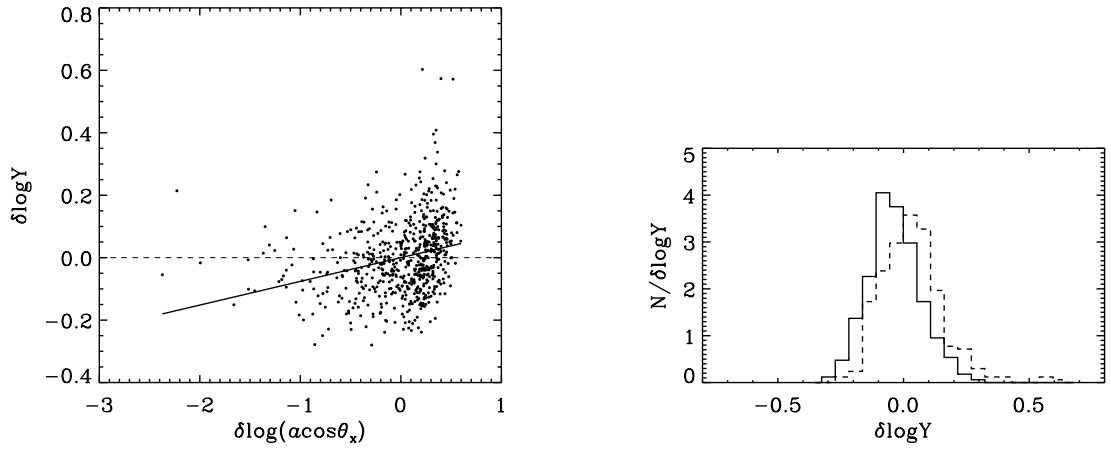

Figure 3.8: *Left*: Correlation between the Y–M scatter and the $a\cos\theta_x$–M scatter at $z = 0$. Clusters that are more elongated along the line-of-sight have larger values of $a\cos\theta_x$. Correlation coefficient is 0.345. *Right*: Normalized distributions of the Y–M scatter for clusters with the morphology measure $a\cos\theta_x$ smaller than the median (solid) and larger than the median (dashed). The scatter distribution for clusters with elongated shape along the line-of-sight (dashed; $\gamma = 1.04$, $\kappa = 2.63$) is much more non-lognormal than that of the remaining population (solid; $\gamma = 0.29$, $\kappa = -0.08$).

Motivated by our results in § 3.3.3 that the non-lognormality may be due to clusters that happen to have elongated shapes aligned with the viewing direction, we invented a measure, $a\cos\theta_x$, to trace cluster morphology along the line of sight. Figure 3.8 shows the Y–M scatter versus the scatter in the $a\cos\theta_x$–M relation. The positive correlation indicates that clusters that are more elongated along the line of sight preferentially have higher Y–M scatter, which is expected because the SZ flux is roughly proportional to the column density of the gas (see Eq. 3.1). Given the best-fit relation, $\delta\log Y = 0.076 \times \delta\log(a\cos\theta_x)$, we can again reduce the scatter by applying a correction as in Eq. 3.14. By doing so we find that the scatter is reduced from 12.07% to 11.63% (i.e. by 3.6%).

We further divide the cluster sample in half using the values of $a\cos\theta_x$ and plot the normalized distributions of the Y–M scatter in Figure 3.8. We find that the scatter distribution of the clusters with larger $a\cos\theta_x$ is non-lognormal ($\gamma = 1.04$, $\kappa = 2.63$), while the skewness and kurtosis of the remaining population are greatly reduced ($\gamma = 0.29$, $\kappa = -0.08$). Therefore, the non-lognormality is indeed caused by the clusters with more elongated shapes along the line of sight.

3.4.4 Projection effects due to large-scale structure

Since the SZ flux is obtained by integrating along the line of sight within a projected radius, it is subject to contamination by gas that lies along the same line of sight, which causes the large number of high-scatter objects in the Y–M relation found in simulations that include light cones (White et al., 2002; Hallman et al., 2007). These outliers and the outliers due to morphology discussed in the previous section can both drive the non-lognormality of the scatter. Since our simulated observations only include isolated clusters and thus do not take the projection effect into account, the skewness and kurtosis estimated from our simulation may be considered to be underestimates of the true values. In this case, it is even more important to adopt the higher moments in the parametrization of the scatter in order to get unbiased cosmological constraints.

3.4.5 Insights from idealized samples

Figure 3.9 shows the percentage contribution of scatter for each idealized cluster sample with respect to the simulated sample. The cluster sample at the bottom has the most constraints on and least freedom in the model parameters, and the assumptions are loosened one at a time from bottom to top (see Table 3.1 for a summary of model descriptions). In general the values are independent of mass, that is, the processes shape the scaling relation in a self-similar way, as expected in the absence of additional baryonic physics. The only exception is the bottom curve for which only the masses of clusters are assigned. In principle this sample should have zero scatter if the resolution of gas cells were infinite, but in reality the finite resolution introduces a nonzero scatter which becomes bigger as more low-mass clusters are included. Because the idealized samples are all constructed under the assumption of spherical symmetry, we derived Sample SS (second line from the top in the figure) using gas profiles directly extracted from the simulated clusters, such that it includes all sources of scatter except the morphological effect. In other words, the difference between the simulated clusters and the spherically-smoothed clusters is solely due to the variation in cluster morphology, which is $\sim 10\%$.

From the differences between the subsequent samples we are able to isolate the contribution of each effect to the total scatter: the variation in halo concentration contributes $\sim 10-20$ % (difference between A and B), the departure from hydrostatic equilibrium results in $\sim 10-15$ % (between B and C), merger boosts add another $\sim 30-60$ % (between C and D), the variation in gas fractions introduces $\sim 0-10\%$ (between D and E), and the rest (between D and SS) due to other unaccounted-for effects is $\sim 0-30$ %. Note that the contribution from variation in concentration quoted here is estimated using sample B,

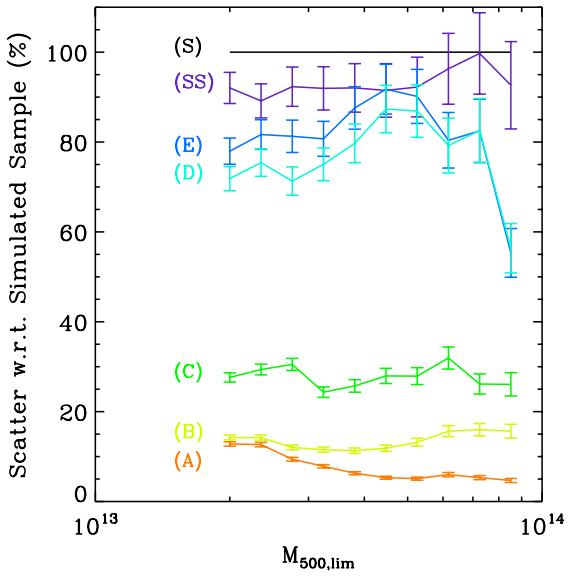

Figure 3.9: The percentage contribution of the scatter for each idealized sample with respect to the simulated sample. The bottom (top) sample includes the least (most) physical sources of variations. See Table 3.1 for a summary of notations and assumptions used to construct each sample.

which assumes spherical symmetry and hydrostatic equilibrium. However, in reality, both changing cluster morphology and including random gas motions (Lau et al., 2009) would further modify the distribution of gas and hence alter the measured value of concentration. In other words, the scatter is driven not only by the variation of concentration in sample B, but also by that due to cluster morphology and departure from HSE. Therefore, the total effect of concentration, as suggested by the correction for concentration in § 3.4.1 (i.e. $\sim 40\%$), would be more appropriately accounted for by also considering the contributions from morphology and random gas motions.

3.5 Combining X-ray and SZ scaling relations

In the previous sections we have discussed various sources of intrinsic scatter in the relation between the SZ flux and the *true* mass. However, observationally cluster masses still need to be measured in some way, such as via X-ray hydrostatic assumptions or optical richness. Cross-calibration across measurements at different wavelengths is important because it provides a consistency check that can minimize the possible systematic effects of each individual measurement (e.g. Plagge et al., 2010), such as the projection effects to which SZ and optical

observations are subjected to. Therefore, high-precision cluster cosmology requires that we combine SZ cluster surveys with X-ray or optical follow-ups (High et al., 2010; Menanteau et al., 2010).

However, one needs to be cautious when combining multiple mass proxies because their errors may be correlated. For example, because both the SZ and optical signals are subject to projection effects, clusters can have consistent mass estimates that are both actually biased with respect to the true mass (Cohn & White, 2009). Since it is impossible for observations to disentangle such correlations, one has to rely on numerical simulations to determine whether these effects are serious for any given pair of mass proxies. Here we would like to explore whether this correlated error exists between the SZ flux and the low-scatter X-ray mass proxy (Kravtsov et al., 2006), Y_X, which is commonly used as a mass proxy in X-ray observations. Note that although individual X-ray properties such as M_{gas} and T_X would be affected by core properties, Stanek et al. (2010) found that the Y_X parameter, which combines the effects of M_{gas} and T_X, is remarkably insensitive to baryonic physics. That is, for their runs with and without the preheating prescription, both the amount and shape of the Y_X–M scatter are almost identical. Therefore, our results below should be robust to additional baryonic physics.

Figure 3.10 shows the mass predicted by the Y_{SZ}–M relation versus that predicted by the Y_X–M relation (M is the true mass). Clusters in the upper panel have less than 2σ deviations from both the mean Y_{SZ}–M relation and Y_X–M relation. The lower panel shows the clusters whose mass scatter is bigger than 2σ for either relation. From the upper panel we can see that clusters that have consistent $M_{Y_{SZ}}$ and M_{Y_X} are mostly faithful tracers of their true masses. But how about the outliers in both the true Y_{SZ}–M and Y_X–M relations? If they give consistent mass estimates, then there would be a similar problem of correlated error as described above. Fortunately, we find that the outliers in both relations (those plotted with both open and filled symbols) would *not* yield consistent mass estimates. This is because while the Y_{SZ}–M outliers are due to cluster morphology, as discussed in § 3.4.3, we find that the Y_X–M outliers are primarily dynamically unrelaxed clusters. Since the errors come from different physical sources, they are not correlated.

This implies the possibility of cutting off the outliers by selecting only clusters whose $M_{Y_{SZ}}$ and M_{Y_X} agree within 1σ. Moreover, applying the same cut will also remove almost all the other Y_{SZ}–M outliers. That is, among the 21 Y_{SZ}–M outliers (15 are 2σ and 6 are 3σ), 19 of them (13 are 2σ and 6 are 3σ) can be ruled out using this method. After applying the cut, we find that the RMS scatter in Y_{SZ}–M is reduced from 12.07% to 8.77% (i.e. by 27.3%), and also the non-lognormality of the Y_{SZ}–M scatter is greatly reduced (skewness reduced from 0.82 to 0.30; kurtosis from 2.17 to -0.07). Therefore, combining mass estimates

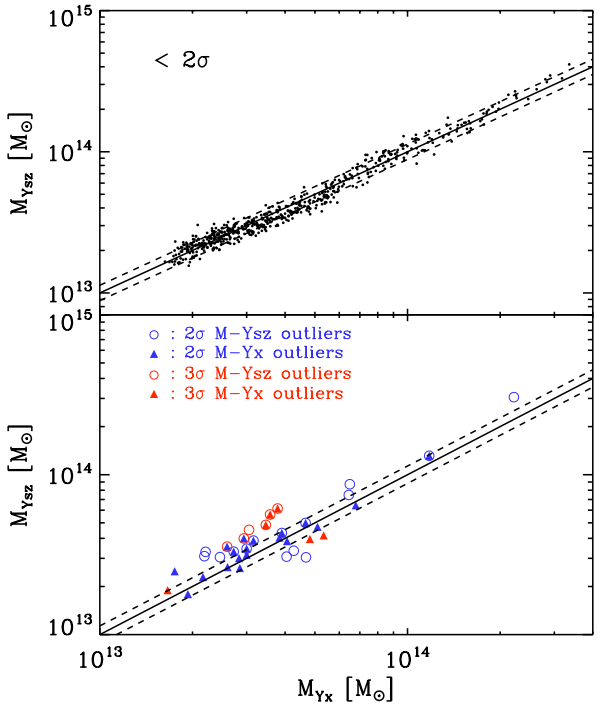

Figure 3.10: Y_{SZ} predicted mass versus Y_X predicted mass. Clusters in the *upper* panel have less than 2σ deviations from both the mean Y_{SZ}–M relation and Y_X–M relation, while clusters whose mass scatter is bigger than 2σ for either relation are plotted in the *lower* panel. Dashed lines show 1σ deviations from the mean $M_{Y_{SZ}}$–M_{Y_X} relation. The fact that clusters that are outliers in both relations (those with overlaying circle and triangle) do not have consistent mass estimates within 1σ indicates that the errors in $M_{Y_{SZ}}$ and M_{Y_X} are not correlated.

from Y_X measurements may be an effective way of both reducing the scatter and removing Y_{SZ}–M outliers. Note that since the projection effect is not included in our simulation, we expect there would be more Y_{SZ}–M outliers in reality, while the Y_X–M relation is relatively insensitive to the projections. Indeed, the contamination by projection errors estimated by Hallman et al. (2007) using a light cone simulation is $\sim 25\%$ (for a projected radius of R_{500}), larger than ours (21 out of 619 clusters). However, because of the fact that the errors in the Y_{SZ}–M and Y_X–M relations are not correlated, clusters that are subject to projection errors can also be removed using the same method.

3.6 Discussion and conclusions

Galaxy clusters are invaluable cosmological probes. Accurate measurement of cluster masses is crucial and often relies on the mass-observable relations. However, to constrain the cosmological parameters at the few percent level, the systematics and scatter in these relations must be thoroughly understood. In this work we investigated the sources of intrinsic scatter in the SZ flux-mass (Y–M) relation using a hydrodynamics plus N-body simulation of galaxy clusters within a cosmological volume. Exploring the origin of the intrinsic scatter not only provides physical insights into the formation of galaxy clusters, but also has two main advantages for using clusters in cosmology. The first is that it allows us to avoid possible systematic biases in the derived cosmological constraints. Do mergers bias the scaling relation? Is the intrinsic scatter lognormal? What are the gains and issues of combining SZ and X-ray scaling relations? Secondly, if we understand the sources of scatter, it is possible to reduce the scatter by removing the contribution from a certain source (see § 3.4.1 for details), and thus tighten the scaling relation to obtain better estimates of cluster masses.

To address these questions, we derived the scatter around the best-fit Y–M relation from the simulated clusters. We first assessed the lognormality of scatter by computing the skewness (γ) and kurtosis (κ) of the scatter distribution. Then we investigated the possible sources of scatter, including halo concentrations, dynamical states and cluster morphology, by correlating the scatter with quantitative measures of each source. We also constructed a set of idealized cluster samples with varied assumptions about the sources of scatter to decompose the percentage contribution from each effect. Finally we compared cluster masses derived from the SZ flux and from the low-scatter X-ray mass proxy, Y_X, and examined whether such consistency checks can help rule out outliers in the true Y_{SZ}–M and Y_X–M relations, or whether issues like correlated errors would affect the accuracy when combining SZ and X-ray scaling relations. Our main results are summarized below.

1. The RMS scatter in the Y–M relation is $\sim 5-15\%$ and decreases with cluster masses and redshifts. We find that the scatter in our simulation can be expressed in the functional form, $\sigma(M,z) = A\log M + B\log(1+z) + C$ (Eq. 3.7), where the redshift evolution is equivalent to re-scaling with respect to the characteristic mass scale in the self-similar model.

2. The distribution of the Y–M scatter is non-lognormal with positive skewness and kurtosis across a wide range of different limiting masses and redshifts, because of the limited number of clusters at the higher-mass end and the tail in the scatter distribution due to morphology at the lower-mass end.

3. There is a strong correlation between the Y–M scatter and the concentration, which can be used to reduce the Y–M scatter from 12.07% to 7.34% (i.e. by 38.9%).

4. The correlation between the scatter and cluster dynamical state is weak. Though merger boosts and departure from hydrostatic equilibrium can partly drive the dispersion, the net effect is that mergers do not cause a significant bias in the scaling relation.

5. There is a moderate trend that clusters that are more elongated along the line of sight tend to scatter high. More importantly, they are the main outliers that cause the non-lognormality of scatter.

6. By decomposing the scatter using the idealized cluster samples, we find the percentage contribution from each source of scatter: $\sim 10\%$ due to variations in morphology, $\sim 10-20\%$ due to variations in concentration (under the assumption of spherical symmetry and hydrostatic equilibrium), $\sim 10-15\%$ due to departure from hydrostatic equilibrium, $\sim 30-60\%$ due to merger boosts, $\sim 0-10\%$ from variations in gas fractions. The remainder (due to unaccounted-for sources) is $\sim 0-30\%$.

7. We find that the RMS scatter in Y_{SZ}–M is reduced from 12.07% to 8.77% (i.e. by 27.3%) when X-ray measurements are combined with SZ.

8. The errors in mass determined using Y_{SZ} and Y_X come from different causes. Therefore, excluding clusters with inconsistent estimates can effectively remove the outliers in both Y_{SZ}–M and Y_X–M relations, especially Y_{SZ}–M outliers that are subject to projection errors.

In our current simulation, radiative cooling and heating mechanisms are not included, since we would like to disentangle the scatter driven by the gravitational effects from other baryonic physics that are not fully understood. Moreover, it has been shown that the integrated SZ flux, and more specifically the scatter, slope, and redshift evolution of the Y–M relation, are generally insensitive to details of cluster gas physics (da Silva et al., 2004; Motl et al., 2005; Nagai, 2006). Since the non-lognormality is mainly caused by the effects of projection and cluster morphology, we could assess the potential impact of baryonic physics on these two sources. Shaw et al. (2008) showed that the influence of different gas physics on the properties of large-scale projections is negligible. Recently Lau et al. (2011) has re-

ported the difference in cluster shapes between simulations with and without cooling and star formation. They found that in the cooling plus star formation simulation clusters are more spherical outside the core ($r > 0.1R_{500}$) but more triaxial inside the core. It is difficult to estimate directly from their results how much this difference in morphology would affect the non-lognormality of the Y–M scatter. However, as pointed out by Lau et al. (2011), their simulation may suffer from the overcooling problem and hence their results can be considered as an upper limit. Moreover, Nagai (2006) used clusters from the same simulations and showed that when the SZ flux is integrated to R_{500}, the Y–M scatter is insensitive to the gas physics included. Therefore, we expect the effect of gas physics on the non-lognormality estimated in this study, if any, is very small. We will present a more detailed comparison in a separate paper.

Our results have several important implications for cluster cosmology. First of all, the strong correlation with halo concentrations can be used for observed clusters to reduce the scatter in the scaling relations for better mass estimates. Potentially this method can be applied to any observable for which such a correlation exists, such as gas fractions (which is expected to play a more important role when including other baryonic physics, see Stanek et al. (2010)). Secondly, the weak influence of mergers is good news for cluster cosmology, because it implies that when deriving observed scaling relations, it is unnecessary to worry much about the selection bias due to the impact of mergers. Finally, the non-lognormality of the Y–M scatter has an impact on cosmological constraint studies. As demonstrated by Shaw et al. (2010a), both positive skewness and kurtosis cause up-scattering of clusters and thus would increase cluster counts above a given limiting mass, which is equivalent to an increase in the amount of scatter. For SZ surveys like the South Pole Telescope (SPT) survey, the skewness and kurtosis of the intrinsic scatter have to be less than 0.5 to ensure that uncertainty in the amount of scatter does not degrade the constraint on the dark energy equation of state w. However, we find that the intrinsic skewness and kurtosis can be much greater than 0.5 across a wide range of limiting masses and redshifts. These values are very likely to be lower limits because the projection effect of large-scale structure is absent in our analysis. Therefore, our results suggest that the assumption of lognormal scatter is inappropriate for scaling relations like the Y–M relation whose scatter is easily skewed by cluster morphology, projection effects, etc. Instead, in self-calibration studies of cosmological constraints that require assumptions about the form of scatter, it is necessary to include the higher-order moments in the parametrization. During the next decade, more and more data from multi-wavelength cluster observations will be available. We expect that more detailed studies of the intrinsic scatter in the scaling relations will continue to yield essential information both for cluster physics and cluster cosmology.

Chapter 4

Sensitivity test of AGN subgrid models

4.1 Introduction

Clusters of galaxies are useful probes of cosmological parameters, provided that their masses can be determined accurately from multi-wavelength observations calibrated based on theoretical models. However, it is still a challenge for current theoretical models to reproduce all the observed properties of the baryonic content in the clusters. Despite the fact that current cosmological simulations with radiative cooling and supernova feedback are able to reproduce profiles of the intracluster medium (ICM) outside the cores, the simulated cluster cores generally suffer from the over-cooling problem, that is, the fraction of cool-core (CC) clusters and stellar fraction in these simulations are too high compared to observed values (e.g. Nagai et al., 2007a). Therefore, some additional forms of heating are required to suppress cooling, among which feedback from active galactic nuclei (AGN) is one of the most promising candidates, as observations of X-ray cavities blown by jets from the central AGN infer power that is comparable to the X-ray luminosity, suggesting a feedback loop might be at work (Dunn & Fabian, 2008).

In terms of theoretical modeling of AGN feedback in cosmological simulations, since a wide range of scales are involved, from the accretion disk of the supermassive black hole (SMBH) on AU scales to clusters on Mpc scales, direct simulation with all relevant physics is beyond current computational power. Thus cosmological simulations with AGN feedback to date have to model its sub-resolution effects by linking the resolvable scale (usually $\sim$kpc) to the SMBH accretion disk scale using some simplified assumptions (Sijacki et al., 2007; Booth & Schaye, 2009; Gaspari et al., 2011b; Dubois et al., 2010). These studies have made much success in explaining the cosmic evolution of SMBH, star formation history, and local scaling relations between the black hole mass and host properties, though current AGN models are still quite phenomenological. One important question to ask is whether these simulations can simultaneous reproduce observed ICM properties as well. Analyses in this direction have started only recently (e.g. Gaspari et al., 2011b) and need to be further addressed.

Predictions of the core properties of clusters from cosmological simulations with AGN

can provide crucial information for cluster cosmology. For instance, the CC fraction as a function of mass and redshift is important for understanding the X-ray selection bias toward CC clusters because of their peaked surface brightness (Allen et al., 2011). For calibrating the scaling relations of multi-wavelength cluster surveys, one may not be comparing apples to apples if such selection bias is not adequately accounted for. Moreover, the core properties may have an impact on the evolution in the slopes, normalizations, and scatter in the scaling relations. In order to put meaningful cosmological constraints using the self-calibration method (Majumdar & Mohr, 2004), the parametrizations of the scaling relations have to be informed by numerical simulations.

However, the uncertainties in the AGN subgrid models are not yet well understood. Since it is still unknown how to link the accretion and feedback across different scales, there is a great degree of freedom to implement and parametrize the AGN subgrid models. The model parameters sometimes do not have a clear connection to observable quantities, and hence constraints from observations cannot be easily applied. Moreover, because it requires large computational power to run these cosmological simulations, it is difficult to perform detailed parameter studies to assess the robustness of the results. But in order to achieve predictions with high precision and controlled systematics, it is necessary to appropriately parametrize our ignorance in the AGN models and quantify the theoretical uncertainties.

The aim of this study is to quantify the current theoretical uncertainties due to model variations in predicting the ICM properties and thus provide a general guideline for cosmological simulations including AGNs. To this end, we implement a subgrid AGN model in FLASH that incorporates several different AGN accretion and feedback models. To study the effect of AGN feedback on cluster observables, we put these models in an idealized cluster and explore the parameter space allowed by available observed constraints. Connections between the model parameters and observable quantities are provided whenever possible. We identify the numerical details and parameters that the results are most sensitive to, as well as the most uncertain aspects in these models.

The structure of this paper is as follows. The analytical and numerical approaches are described in § 4.2. The results of the sensitivity test is presented in § 4.3. Parameters investigated include resolution, strength of accretion, feedback efficiencies, feedback frequencies, sizes of feedback, and the ratio between thermal and kinetic energy. Our findings will be summarized in § 4.4.

4.2 Methodology

4.2.1 Simulation setup

We performed three-dimensional hydrodynamic simulations with radiative cooling and AGN feedback within an isolated cluster sitting in a 2048 kpc box using the adaptive mesh refinement (AMR) code FLASH 3 (Fryxell et al., 2000; Dubey et al., 2008). The cluster is set up in the same way as in Cattaneo & Teyssier (2007) and has properties similar to M87. The cluster gas is initialized assuming a polytropic equation of state (EOS) (Komatsu & Seljak, 2001) and is in hydrostatic equilibrium in an NFW (Navarro et al., 1995) gravitational potential. The cluster has a virial mass of 1.5×10^{14} $M_\odot$, concentration of 5.53, and gas fraction of 0.1. A 3×10^9 $M_\odot$ black hole is placed in the center, which is only used for computing the accretion and feedback quantities and does not contribute to the gravitational potential. The base grid resolution is 32 kpc at cluster outskirts (grid size is 32 kpc), and the region of radius 120 kpc surrounding the central black hole is refined progressively to a maximum resolution of 1.0 kpc for the fiducial run.

The diode boundary condition is used, which is like the outflow boundary condition but not allowing matter to flow into the domain. Radiative cooling is computed using Sutherland & Dopita (1993) assuming 1/3 solar metallicity. Star formation and feedback from supernovae are neglected because themselves have heterogeneous implementations and require detailed comparisons of their own. In this study we intend to investigate the modeling of AGN alone and avoid confusions due to possible interferences with other subgrid physics. The Hubble constant $h = 0.65$ is used. When overdensity quantities are quoted, they are computed using the overdensity radius R_Δ where the enclosed average density is Δ times the critical density of the universe.

4.2.2 AGN subgrid models

In this study we compare several accretion and feedback subgrid models adopted in cosmological simulations in the literature. Since our main goal is to quantity the model uncertainties, the models are chosen to cover very different methods of implementation and parameterization. For estimating the BH accretion rate, we consider the α model (Sijacki et al., 2007) and β model (Booth & Schaye, 2009). The feedback from the AGN is modeled using two different approaches: the bubble feedback (Sijacki et al., 2007) and the jet feedback (Cattaneo & Teyssier, 2007; Dubois et al., 2010; Gaspari et al., 2011b). Here we summarize the important aspects of these models.

To include the accretion onto the SMBH self-consistently in cosmological simulations, the

simplest approach is to estimate the accretion rate using the Bondi-Hoyle-Lyttleton (Bondi, 1952) accretion rate:

$$\dot{M}_{\rm BH} \propto \dot{M}_{\rm Bondi} = 4\pi G^2 M_{\rm BH}^2 \rho / c_{\rm s}^3, \tag{4.1}$$

where $M_{\rm BH}$ is the BH mass, and ρ and $c_{\rm s}$ are the gas density and sound speed, respectively. Cosmological simulations usually do not have sufficient resolution to resolve the Bondi radius, $r_{\rm Bondi} \equiv GM/c_s^2$, as well as the multiphase gas when the density is high enough to trigger star formation. Therefore the density (temperature) at the Bondi radius would likely be higher (lower) than values on the grid. The actual Bondi accretion rate would thus be underestimated, which is reflected by the proportionality in the above equation. The α model assumes a constant coefficient, i.e., $\dot{M}_{\rm BH} = \alpha \dot{M}_{\rm Bondi}$.

However, as pointed out by Booth & Schaye (2009), the value of α is often taken to be ~ 100 in previous works to drive substantial black hole growth (Di Matteo et al., 2005; Sijacki et al., 2007; Bhattacharya et al., 2008). Such large values imply that the Bondi rate actually is not a good approximation in these cases. Moreover, for situations when the Bondi rate is applicable (e.g. for simulations with sufficient resolution, or when densities are low enough), multiplying it by 100 would significantly overestimate the accretion rate. Therefore, Booth & Schaye (2009) proposed the β model as an alternative way to compute the accretion rate:

$$\dot{M}_{\rm BH} = \begin{cases} \dot{M}_{\rm Bondi} & \text{if } n_H < n_H^* \\ (n_H/n_H^*)^\beta \dot{M}_{\rm Bondi} & \text{otherwise} \end{cases} \tag{4.2}$$

where $n_H^* = 0.1$ cm^{-3}. This model is consistent with the Bondi prediction when the Bondi radius is resolvable and is density dependent to account for accretions of the multiphase gas.

For all accretion models, we impose an upper limit on the accretion rate corresponding to the Eddington rate, $\dot{M}_{\rm Edd} = (4\pi G M_{\rm BH} m_{\rm p})/(\epsilon_{\rm f} \sigma_{\rm T} c)$, where $m_{\rm p}$ is the mass of the proton, $\sigma_{\rm T}$ is the Thompson cross-section and $\epsilon_{\rm f}$ is the radiative efficiency.

The region for computing the accretion rate as well as the region to deplete the accreted gas from are typically set to a few zones around the central BH, but their sizes are essentially arbitrary. We denote these two radii as $R_{\rm acc}$ and $R_{\rm dep}$, and will probe several values in § 4.3.2. Since gas in a grid cell can possibly be completely removed during strong accretion and cause unphysical surge of gas around the black hole, gas depletion is not allowed to remove 10% of the gas on a grid cell in one timestep.

The feedback from the AGN to the surrounding gas is then computed according to the accretion rate. There has been growing observational evidences for the anti-correlation between radio loudness and SMBH accretion rate (Ho, 2002; Sikora et al., 2007). That is, radio jets are associated with systems with lower accretion rate, while objects with higher

accretion rate, like quasars at higher redshifts, are radiatively efficient, analogous to states of X-ray binaries (Fender et al., 1999; Gallo et al., 2003). For this reason, we follow the prescription in Sijacki et al. (2007) for switching to the quasar mode when the accretion reaches 1% of the Eddington rate. In the quasar mode, the radiative energy is thermally coupled to the surrounding gas, $E = \epsilon_{\rm r}\epsilon_{\rm f}\dot{M}_{BH}c^2$, where $\epsilon_{\rm r}$ is the quasar heating efficiency. The region to dump the quasar thermal energy is chosen to be four zones in radius, though it is arbitrary. Note that in some other subgrid models (Booth & Schaye, 2009, e.g.) there is no division between the quasar and mechanical feedback since they are both assumed to be purely thermal and spherically distributed. However, we will show that when feedback energy is injected in the thermal form, the size of the region has a significant impact on the results.

At low accretion rates, one can choose either bubble or jet feedback. For the bubble feedback (Sijacki et al., 2007), the feedback energy is distributed in terms of thermal energy within a spherical region around the SMBH. The bubbles are only formed when the BH mass increases by a fraction $\delta_{\rm BH}$ since the last bubble formation. When a bubble is formed, purely thermal energy is injected:

$$E = \epsilon_{\rm m}\epsilon_{\rm f}c^2\delta M_{\rm BH}, \tag{4.3}$$

where $\epsilon_{\rm m}$ is the efficiency of mechanical heating, and $\delta M_{\rm BH} \equiv \delta_{\rm BH} M_{\rm BH}$ is the increase in BH mass since the last bubble was formed. The injected energy is distributed in a mass-weighted sense within a sphere of radius,

$$R = R_0 \left(\frac{E/E_0}{\rho/\rho_0}\right)^{1/5}, \tag{4.4}$$

where the scaling parameter values $R_0 = 30\,h^{-1}$kpc, $E_0 = 5{\times}10^{60}$ erg, and $\rho_0 = 10^6\,h^2{\rm M}_\odot{\rm kpc}^{-3}$ are motivated by observed bubble sizes. The bubble centers are randomly displaced within a sphere of radius $R_{\rm dis}$ in unit of bubble radius centered on the black hole. In the fiducial run $R_{\rm dis} = 1.0$. We will also experiment cases where bubbles are fixed at the central black hole, i.e., $R_{\rm dis} = 0$.

In contrary to the bubble feedback which only injects thermal energy into the surrounding ICM, the jet feedback simulations inject partial or all energy in the kinetic form. The jet models do not intend to simulate the relativistic jet directly but the non-relativistic outflow from the accretion disk (Proga, 2007) or decelerated large-scale jet after it entrained some intergalactic medium during its propagation (Feretti et al., 1999; Laing & Bridle, 2002). The ratio between injected thermal to kinetic energy depend on the parametrization and is different from study to study. While Gaspari et al. (2011b) and Dubois et al. (2010) adopted

purely kinetic jets, in Cattaneo & Teyssier (2007) the injected energy is mostly thermal, depending on the amount of mass loading. Their model is motivated by that more massive, slow jets should couple more thermal energy with the surroundings as they propagate. However, purely kinetic jet in their model would produce relativistic velocities, which cannot be treated adequately in non-relativistic hydrodynamic simulations. In order to make comparisons, we combined their models and use a more general parametrization to allow tuning the thermal to kinetic ratio, while the jet velocities are independently determined by the amount of mass loading.

Our generalized jet model is summarized as the following. The injection rates of the mass, momentum, and energy onto the grid are treated as source terms in the hydrodynamic equations and are calculated by

$$\begin{aligned} \dot{M} &= \eta \dot{M}_{\rm BH} |\Psi|, \\ \dot{P} &= \sqrt{2\eta\epsilon_{\rm f}(1-\epsilon_{\rm m})}\dot{M}_{\rm BH} c \Psi, \\ \dot{E} &= \epsilon_{\rm f} \dot{M}_{\rm BH} c^2 |\Psi|, \end{aligned} \tag{4.5}$$

where η is the mass loading factor, and E is the sum of injected thermal and kinetic energy, i.e., $E = E_{\rm th} + E_{\rm k}$. For non-relativistic jets, $E_{\rm k} = P^2/2M$, thus in this model $\epsilon_{\rm m}$ of the total energy goes into the thermal energy and the remaining is kinetic. Jet velocity is $\sqrt{2\epsilon_{\rm f}(1-\epsilon_{\rm m})/\eta} \times c$, which is $\sim 10^4$ km/s for $\eta = 100$, $\epsilon_{\rm f} = 0.1$ and $\epsilon_{\rm m} = 0$. The function Ψ determines the spatial extent of the jet:

$$\Psi(\mathbf{x}) = \frac{1}{2\pi r_{\rm ej}^2} \exp\left(-\frac{x^2+y^2}{2r_{\rm ej}^2}\right) \frac{z}{h_{\rm ej}^2}. \tag{4.6}$$

The jet is aligned with the z-axis and the feedback is applied to regions with $|z| \leq h_{\rm eq}$ and $r \leq r_{\rm ej}$. We also normalize the window function Ψ so that the total injected energies in the cylinder sum up to E. Note that there is no threshold for injecting the jets and hence the jet feedback is continuous rather than episodic.

Note that our jet model has several modifications to that in Cattaneo & Teyssier (2007). In addition to changes in the parametrization as described above, we normalized the function Ψ as in their subsequent papers based on the same model (Dubois et al., 2010). They fixed the mass of the black hole for computing the accretion rate while our black hole can grow from gas accretion. This has negligible effects since the accretion rate is small in their setup. Also, we allow gas depletion and use a smaller radius for computing the accretion rates. When accounting for the above differences, we are able to reproduce their results.

4.2.3 Model and parameter variations

Since the details of each subgrid model are so different that it is impossible to explore every implementation and parameter, in this study we intend to focus on those aspects of these models which are least constrained. To this end, the bubble and jet feedback models are chosen because they are different in many aspects, including the form of injected energy (thermal vs. kinetic), shape of injection region (spherical vs. jet-like), and periodicity of feedback (episodic vs. continuous). Comparing these two distinct models allows us to understand the extent of current theoretical uncertainties of these AGN models (Chapter 5).

We first explore 'numerical' parameters that are required in the numerical implementations but are essentially arbitrary and often chosen based on numerical considerations. Variations of these parameters are listed in Table 4.1 and Table 4.2 for the bubble and jet model, respectively. The tests are divided into groups, each of which examines one of the numerical parameters. We first do a convergence test by varying the peak resolution for both the bubble model (group B1) and the jet model (group J1). Because the constant α model is motivated by the argument that the accretion rate is under-estimated due to insufficient resolution to resolve the Bondi radius, in group B2 we scale the α parameter with resolution to see if the results are consistent. In the jet model we don't vary α because we will show that the accretion rate is suppressed from the beginning and hence varying α has a minor effect. Since in the jet model the feedback is distributed in the very inner few kpc around the black hole, it is more likely to interfere with the peak resolution and the choices of the region for gas accretion and depletion. Therefore, we experiment on scaling the jet size with resolution in group J2 and varying the accretion and depletion radii in group J3. The impacts from these numerical considerations will be discussed in § 4.3.2. Note that for these jet runs the feedback and thermal efficiency parameters are chosen to be $\epsilon_{\rm f} = 0.1$ and $\epsilon_{\rm m} = 0\%$, as commonly adopted in previous jet models (Gaspari et al., 2011b; Dubois et al., 2010).

Table 4.3 summarizes the model or parameter variations that are more physically motivated. Again they are separated into groups. The effects we investigate here include varying the accretion, the mechanical feedback efficiency, the threshold for triggering a feedback event, the size and center of the feedback region, and the ratio between thermal and kinetic energy. Here we note that despite the difference in the parameterizations used in the bubble and jet models, we do expect their results to overlap when bubbles are injected almost continuously (with a small $\delta_{\rm BH}$) into a small region centered on the black hole (run P4C), and when the jet is purely thermal (run P5C). And the difference between these two runs would mainly be due to the shape of injection. We present the influences of these 'physical'

Table 4.1: Survey of Numerical Parameters in the Bubble Model.

Name	Δx	α
Varying Resolution		
B1A	0.5	1
B1B	1.0	-
B1C	2.0	-
B1D	4.0	-
B1E	8.0	-
Scaling Alpha with Resolution		
B2A	2	2

parameters in § 4.3.3.

When not specifically mentioned, the parameters are fixed to their fiducial values: $\epsilon_{\rm f} = 0.1$, $\epsilon_{\rm r} = 0.005$, $\epsilon_{\rm m} = 0.2$, $R_0 = 30h^{-1}{\rm kpc}$, $E_0 = 10^{55}$ erg, $\rho_0 = 10^4 h^2 {\rm M}_\odot {\rm kpc}^{-3}$, $r_{\rm ej}$ =3.2 kpc, and $h_{\rm ej} = 2.5$ kpc. Note that these values are chosen to match with previous works in their cosmological studies (Sijacki et al., 2007; Dubois et al., 2010), where they are able to successfully reproduce the observed black hole density, star formation history, and L_X–T_X relation. Therefore it is also one of our aims to examine whether the same set of parameters could also recover the properties of the ICM within observational constraints (Chapter 5).

4.3 Sensitivity study

In this section we present a sensitivity study of all the relevant parameters in the AGN subgrid models. Since most of these parameters are not well constrained due to lack of knowledge of the detailed physical processes, we will first start from a relatively large parameter space. Later in Chapter 5 we will examine whether the results are consistent with observational limits. By performing the sensitivity study we would like to identify those variables to which the ICM properties are most sensitive. At the same time, it also provides us with information about which ICM properties are most robust to the uncertainties in the AGN subgrid models.

4.3.1 The fiducial run

Here we show the general features of run P1A as an instructive example. This run uses the bubble model with parameters that are commonly adopted in previous cosmological

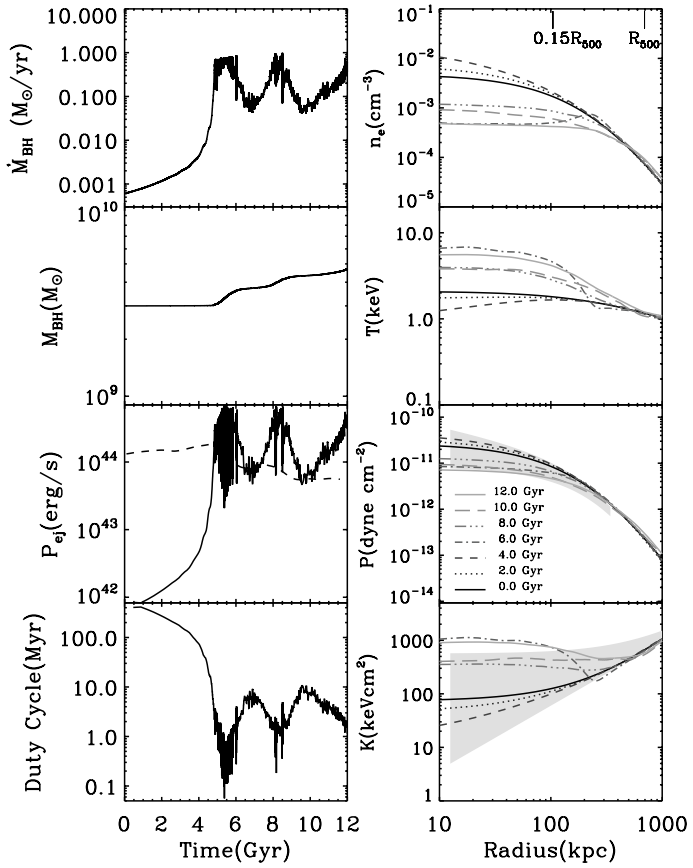

Figure 4.1: Results for the fiducial run P1A. *Left column (from top to bottom)*: Evolution of black hole accretion rate, black hole mass, power of feedback, and duty cycle. The X-ray luminosity inside the core ($R \leq 0.15R_{500}$) is overplotted with the injected power using the dashed line. *Right*: Radial profiles of gas density, temperature, pressure, and entropy. Grey areas are the ranges of pressure and entropy profiles observed by Arnaud et al. (2010) and Cavagnolo et al. (2009), respectively.

Table 4.2: Survey of Numerical Parameters in the Jet Model.

Name	Δx	α	$h_{\rm ej}$	$r_{\rm ej}$ (kpc)	$R_{\rm acc}$	$R_{\rm dep}$ (zones)
Varying Resolution						
J1A	0.5	1	2.0	2.5	2	2
J1B	1.0	-	-	-	-	-
J1C	2.0	-	-	-	-	-
Scaling Jet Size with Resolution						
J2A	-	-	4.0	5.0	-	-
J2B	2.0	-	8.0	10.0	-	-
J2C	4.0	-	16.0	20.0	-	-
J2D	-	-	8.0	10.0	-	-
Varying Radii for Accretion and Depletion						
J3A	-	-	-	-	1	1
J3B	-	-	-	-	4	4
J3C	-	-	-	-	2	0

simulations (Sijacki et al., 2007). The left column of Figure 4.1 shows the evolution of the SMBH accretion rate, the mass of the black hole, the power of feedback (bubble energy divided by the duty cycle), and the duty cycle (time between two feedback events). The right column shows the profiles of gas density, temperature, pressure and entropy ($K \equiv T/n_e^{2/3}$) at different times. For this run, the accretion rate starts from a value of $\sim 6 \times 10^{-4}$ $\rm M_\odot yr^{-1}$. The black hole grows slowly in its mass and generates weak bubbles only every few hundred Myrs for the first ~ 4 Gyr. The injected energy delayed the strong cooling as would occur if there were no feedback. But it is still unable to balance radiative losses, so the accretion rate grows rapidly and reaches the Eddington rate at $t \simeq 5$ Gyr. At this time the accretion rate is held near the value 1 $\rm M_\odot yr^{-1}$ by powerful and frequent ($\sim 0.1 - 1$ Myr) feedback events of both bubbles and quasars, which in turn heat and expand the surrounding gas and caused the accretion rate to drop. The according decrease of feedback then result in another round of strong cooling and feedback events. The cluster then fluctuates with a timescale of ~ 3 Gyr till the end of the simulation.

The gas profiles change according to the AGN activities. In the first ~ 4 Gyr, the central density increases and the temperature decreases due to radiative cooling, similar to the case without AGN feedback. But once powerful feedback from the AGN starts to take place after $t \simeq 5$ Gyr, the gas entropy within the injected bubbles is raised, so that the gas is heated

Table 4.3: Survey of Physical Parameters.

Name	Accretion	Feedback	$\epsilon_{\rm f}$	$\epsilon_{\rm m}$	$\delta_{\rm BH}$	Region
			Varying Accretion			
P1A	$\alpha = 1$ ($\beta = 2$)	bubble	0.1	0.2	0.01%	$R_0 = 30\ h^{-1}$kpc, $R_{\rm dis} = 1.0$
P1B	$\alpha = 10$	-	-	-	-	-
P1C	$\alpha = 100$	-	-	-	-	-
			Varying Mechanical Heating Efficiency			
P2A	-	-	-	0.02	-	-
P2B	-	-	-	0.5	-	-
			Varying Feedback Frequency			
P3A	-	-	-	-	0.001%	-
P3B	-	-	-	-	0.1%	-
			Varying Size of Feedback Region			
P4A	-	-	-	-	-	$R_0 = 15$, $R_{\rm dis} = 1.0$
P4B	-	-	-	-	-	$R_0 = 5$, $R_{\rm dis} = 1.0$
P4C	-	-	-	-	-	$R_0 = 15$, $R_{\rm dis} = 0.0$
			Varying Thermal to Kinetic Ratio			
P5A	-	jet	0.02	0%	0	$r_{\rm ej} = 2.5, h_{\rm ej} = 2.0$
P5B	-	-	-	50%	-	-
P5C	-	-	-	100%	-	-
P5D	-	-	0.1	0%	-	-
P5E	-	bubble	0.1	0.2	0.001%	$R = 2$, $R_{\rm dis} = 1.0$

and pushed outward. After later times the cluster oscillates around a quasi-static profile that is flatter and hotter than the initial profile.

For the pressure and entropy profiles, we overplot our results with the observed profiles recently compiled for a large sample of clusters by Arnaud et al. (2010) and Cavagnolo et al. (2009), respectively. These observed profiles are remarkably uniform and self-similar at outer radii, while the dispersion increases toward the center. We note that despite these energetic AGN outbursts, the pressure profiles at all times lie well within the observed range. The universality of the pressure profiles is maintained because the density and temperature of the bubbles compensate each other to reach hydrostatic equilibrium with the surrounding ICM.

On the other hand, the entropy profiles, though following a standard "power-law plus floor" profile in general, sometimes have contradictions to the observed profiles right after powerful AGN outbursts, e.g., the large floor and entropy inversions at $t = 6$ Gyr and $t = 12$ Gyr. This may be due to the fact that this particular bubble model in this cluster setup generates large bubbles of radii $\sim 100 - 200$ kpc. As we will show in § 4.3.3, this problem is alleviated by reducing the normalization of bubble sizes, R_0.

This run shows that such AGN feedback models can successfully self-regulate black hole growth, as also demonstrated in previous works (e.g. Sijacki et al., 2007). It also produces cluster profiles that are in general consistent with observations. In the following subsections we will start varying the parameters to see how they affect the evolution of the AGN activities and cluster profiles.

4.3.2 Numerical parameters

In this section we present results for varying the numerical parameters both in the bubble model (Table 4.1) and the jet model (Table 4.2). For the bubble model, we study the effect of peak resolution, as well as scaling the α parameter with resolution. For the jet model, we test variations of the resolution, jet sizes, and the radius for computing accretion rate and for removing gas. The definitions and explanations for these parameters can be found in § 4.2.3. We probe the sensitivity to these parameters by examining the evolution of the black hole accretion rate. The cluster profiles are not plotted here since they are closely related to the accretion rate, as seen in the previous section.

The convergence test for the bubble model is shown in Figure 4.2 (left). We allow a large range in variation for the peak resolutions (as large as 8 kpc) because current high-resolution cosmological simulations can typically reach resolutions of a few kpc, but to go beyond that is progressively more difficult due to expensive computational costs. Therefore

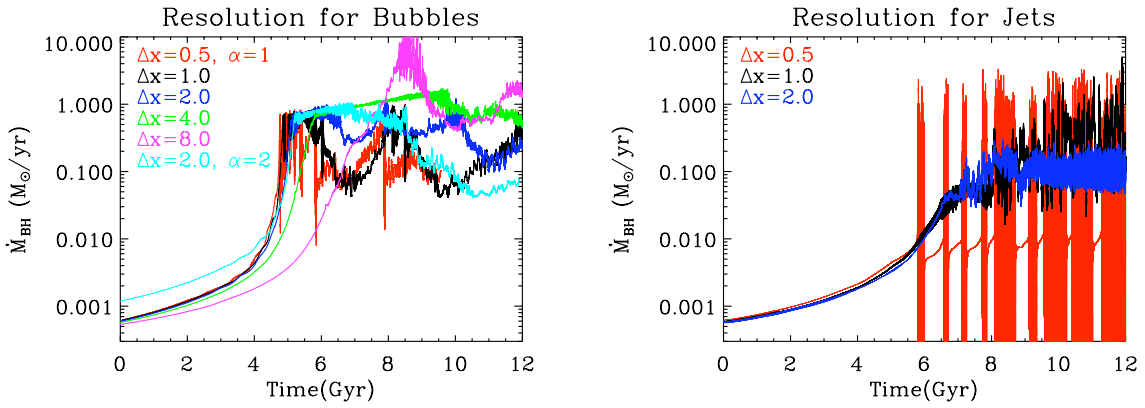

Figure 4.2: *Left*: Black hole accretion rates for varying the peak resolution (group B1) and scaled α with the resolution (group B2) for the bubble feedback model. *Right*: Affecting the accretion rates by varying the peak resolution in the jet feedback model (group J1).

it is important to understand how well such simulations with subgrid AGN models are numerically convergent. We find that as the peak resolution is increased, fluctuations within smaller timescales and with larger amplitudes are captured, whereas for runs with degraded resolutions the accretion rates react more slowly, reach the first peak later, and have less variations. This makes the SMBH in the lower-resolution runs increases its mass at a later time, but grows to a larger value at the end of the simulation by time 12 Gyr. In particular, the final black hole mass for run B1E ($\Delta x = 8$ kpc) differs from run B1B ($\Delta x = 1$ kpc) by about a factor of 2. Therefore simulations with poorer resolutions may underestimate the variations in accretion rate and corresponding ICM properties. They may also find more massive black hole populations when other conditions are held the same.

Since the constant α in the bubble model is often invoked to compensate for the underestimation of the accretion rates due to resolutions, in principle a larger α should be used when the resolution is poorer. In group B2 we test whether such scaling of α would help account for the difference in resolution. As shown in FIgure 4.2, the initial accretion rate for run B2A ($\Delta x = 2$ kpc, $\alpha = 2$) is boosted compared to the run with the same peak resolution (B1C). However, this boost does not help making the accretion rate approach the values of the higher-resolution runs (B1A and B1B), simply because this cluster has a flat initial entropy profile. This points out one problem with the α accretion model, which is that a single constant value of α may not be appropriate for a population of cluster with various core profiles. At later times when cooling and feedback events get stronger, the evolution becomes nonlinear and depends sensitively upon the detailed interactions between the bubbles and quasars with the surroundings. So the outcome of run B2A is neither close

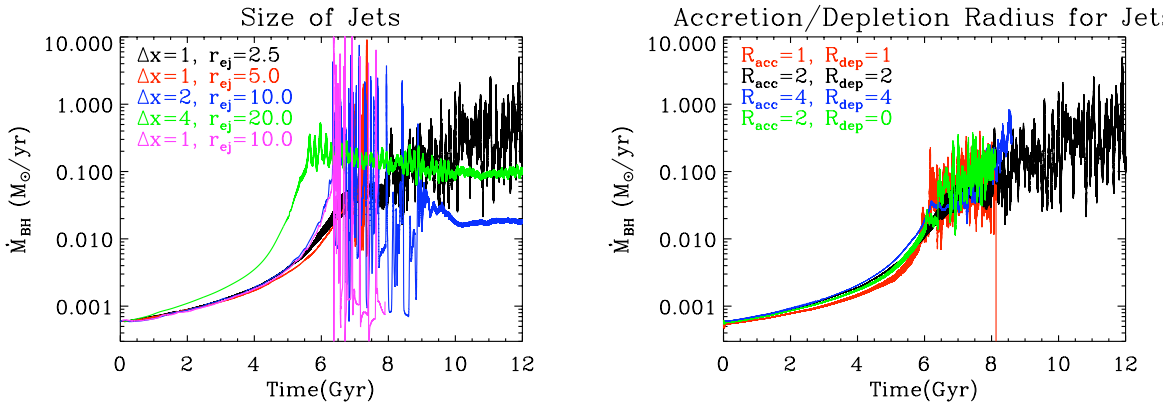

Figure 4.3: *Left*: Black hole accretion rates for different the jet sizes with fixed/scaled peak resolution (group J2). *Right*: Results for changing the radius for computing the accretion rate and the radius for removing the accreted gas in unit of zones (group J3).

to run B1C nor to run B1B. Therefore, simply scaling α by a constant factor does not in general work to compensate for the change in resolution. In fact, we will see in § 4.3.3 that choosing the value of α is nontrivial and has a great impact on the evolution of SMBH and ICM properties.

For the jet feedback model, we also find more variations in the accretion rate for runs with higher peak resolution (Figure 4.2, right). Despite the difference in the amplitude of fluctuations, the mean accretion rates are more robust to the resolution than in the bubble model, at least when the grid size is larger than 1 kpc (run J1B and J1C).

The dramatic change in the accretion rate for run J1A may be understood in combination with the results of scaling jet sizes with resolution (Figure 4.3, left). This problem of large amplitude fluctuations occurs in all the runs where the jet size is much greater than the size of a grid cell (J2A-J2C). Recall that the radius for computing the accretion rate is set to 2 zones. Therefore when the accretion radius is small compared to the region to apply jet feedback, such estimation of accretion rates is picking up the details in the feedback itself more than the actual accretion from the ICM. The only exception is run J2D, which has very extended jets that have essentially the same effects as the bubble feedback. In particular, this run produces results that are comparable to bubbles with high frequencies (run P3A) and small sizes (run P4B) that will be shown in later sections.

Finally we vary the radius for computing the accretion rate, $R_{\rm acc}$, and the radius for removing the accreted gas, $R_{\rm dep}$ (Figure 4.3). We find that either changing the accretion and depletion radii, or removing gas depletion all together, has a minor effect on the results. Note however that run J3A crashed at $t \simeq 8$ Gyr because of a sudden drop in accretion rate.

This may be also caused by the small accretion radius compared to jet sizes. For numerical stability we recommend using an accretion radius larger than the region of jet feedback.

To summarize briefly, we find that increasing the peak resolution generally produces more variable accretion rates. Bubble feedback suffers a greater influence when varying the resolution, whereas jet feedback is more robust, as long as the accretion radius is carefully chosen (larger than the jet sizes).

4.3.3 Physical parameters

Dependence on accretion models

Table 4.3 lists the variations of the physically-motivated parameters under consideration. For the first group of runs we vary the method of computing the accretion rate. Note that the β model is the same as $\alpha = 1$ in the simulations using the bubble model since the feedback is effective in suppressing the central gas density below 0.1 cm^{-3}. Since the cluster has a flat entropy profile at the center, $\alpha = 1$ is justified based on the resolution argument for the Bondi accretion. However, in reality the accretion rate is still likely to be underestimated because of the unresolved multiphase gas. For example, the observed Bondi accretion rate for the SMBH in M87 is estimated to be 0.026 $\mathrm{M}_{\odot}\mathrm{yr}^{-1}$ at its Bondi radius (Allen et al., 2006), which is about 30 times higher than the rate computed from the central entropy of our simulated cluster. Therefore, by choosing α of values ranging from 1 to 100, we expect to cover situations where the actual accretion rate is underestimated as well as where it is overestimated.

Figure 4.4 shows the results of varying the accretion scheme (group P1). As can be seen from the figure, the evolution of the cluster is very different for different accretion models. For run P1A where $\alpha = 1$, the accretion starts from a small value and thus the initial feedback power is small compared to the core X-ray luminosity. Here strong cooling occurs and triggers cycles of feedback events at later times, as described in § 4.3.1. On the other hand, in run P1C ($\alpha = 100$), the feedback power in the beginning is already comparable to the X-ray luminosity, so the cluster never goes through the strong cooling phase and is roughly in equilibrium throughout the simulation time. The cluster profiles respond to the AGN activities in the same way as in the fiducial run, which is the reason why the gas properties have more fluctuations in run P1A than P1C.

The evolution of the cluster core can be further quantified by the entropy floor (Cavagnolo et al., 2009), slopes of the density profile (Croston et al., 2008) and entropy profile (Sanderson et al., 2009), or the cooling time (Mittal et al., 2009). Following the definition in Mittal et al. (2009), we categorize cluster cores into strong cool cores (SCC; $t_{\mathrm{cool}} < 1$ Gyr), weak cool

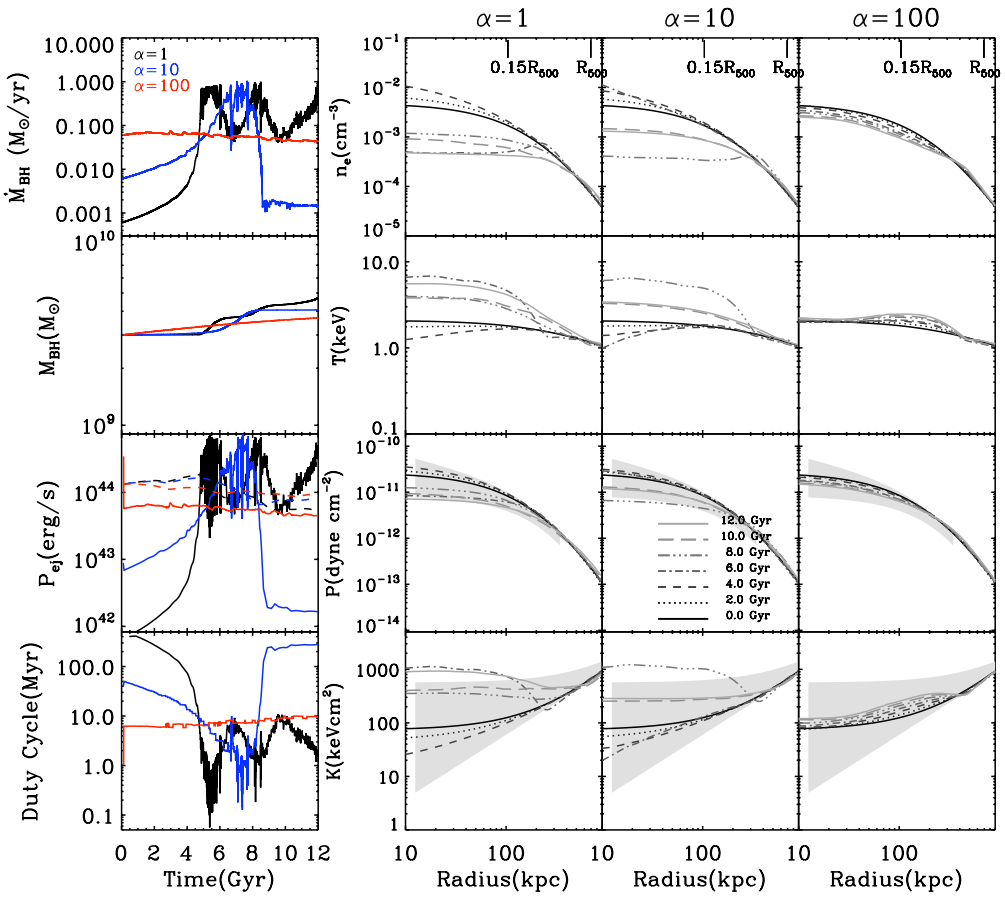

Figure 4.4: Evolution of AGN activity and cluster profiles for different accretion models (group P1). Symbols are the same as Fig 4.1.

cores (WCC; 1 Gyr $< t_{\rm cool} <$ 7.7 Gyr), and non cool cores (NCC; $t_{\rm cool} >$ 7.7 Gyr). Based on this definition, the cluster starts with a WCC with $t_{\rm cool} \sim 7.5$ Gyr. In all the bubble models studied here, the cluster never reaches the SCC state because the overall heating is very effective. For run P1A, the cooling time drops to its minimum of $t_{\rm cool} \sim 2$ Gyr at $t \simeq 4$ Gyr and climbs up to a NCC in the end. Run P1B is similar to P1A. For run P1C, the cooling time instead keeps rising, so the cluster became a NCC soon after the start of the simulation.

The large influence of the assumed accretion model on the evolution history of the cluster poses a great concern for simulations with AGN feedback. It implies that given the uncertainties in the accretion mechanisms, current AGN subgrid models have very limited power to predict the evolution of cluster core properties. That is, simulations with different accretion models can produce very different results, e.g. the fraction of CC versus NCC clusters as a function of time. Note that the cosmological simulation of Sijacki et al. (2007) uses $\alpha = 100$, which is very effective in suppressing the formation of cool cores as we have shown. Indeed their simulations generally overpredict the fraction of NCC clusters at the present day compared to observations.[1] Therefore, in order to produce robust results, accurate modeling of the accretion onto the SMBH is crucial.

Varying the mechanical heating efficiency

The mechanical heating efficiency, $\epsilon_{\rm m}$, parametrizes how much feedback energy is actually converted into thermal energy and used as a source of heating. Observationally the ratio of cavity power to the Bondi accretion rate is estimated to be a few percent (Allen et al., 2006), which motivates previous simulations to adopt similar values for the net efficiency, $\epsilon_{\rm f}\epsilon_{\rm m}$. However, it is still unclear how the cavity power is converted into heat and how long this process takes. If the bubbles do not mix with the ICM efficiently, in principle the mechanical heating efficiency could be much lower. For example, Vernaleo & Reynolds (2007) used purely hydrodynamic simulations and estimated the fraction of injected kinetic energy going into internal energy (i.e. $\epsilon_{\rm m}$) to be only a few percent. But since the actual magnitude of mechanical heating would depend on the details of mixing, simulations with more realistic physical treatment of the ICM are required to pin down this number. Here we probe the range $\epsilon_{\rm m} = 0.02 - 0.5$, which is permitted by current constraints and covers values commonly used in previous simulations.

Figure 4.5 shows the SMBH and cluster evolution with varying $\epsilon_{\rm m}$ (group P2). In general the changes in $\epsilon_{\rm m}$ do not alter the fate of the cluster, in contrast to the variation in the

[1] private communication

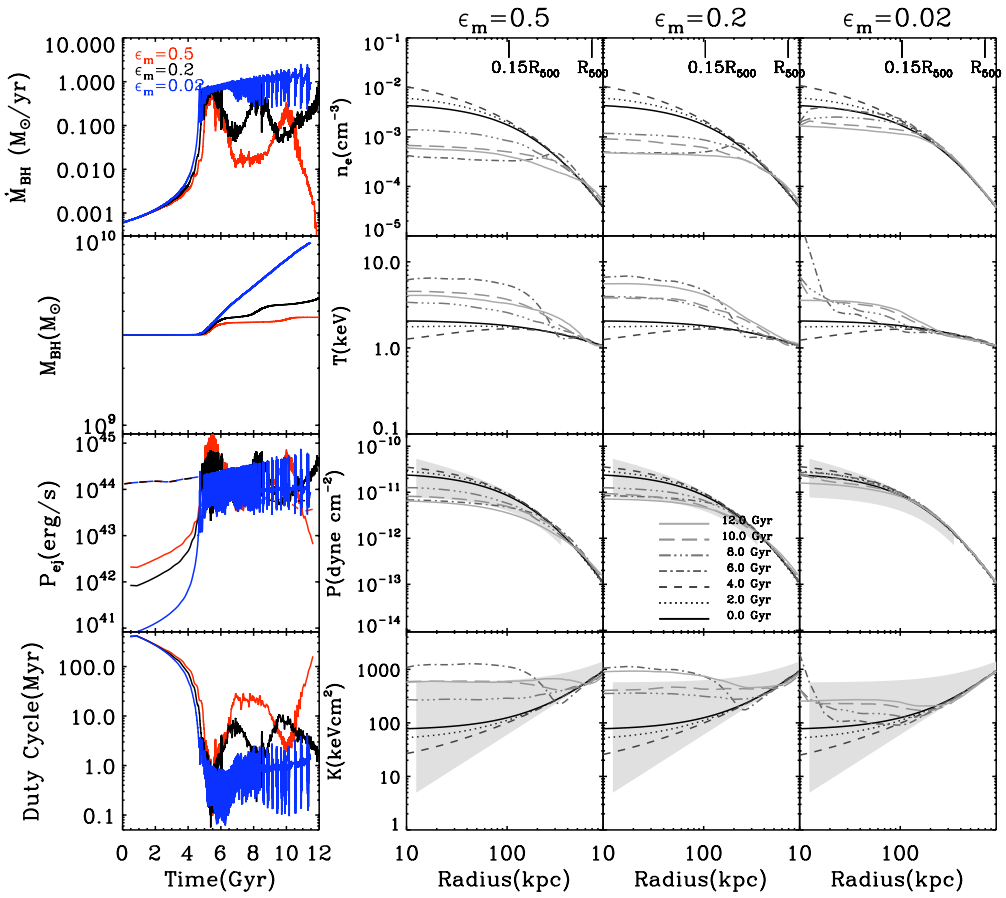

Figure 4.5: Evolution of AGN activity and cluster profiles for different mechanical heating efficiency ϵ_m (group P2 plus the fiducial run P1A).

accretion models discussed in the previous section. For all three runs, the cluster went through gradual cooling for the first 4 Gyr, which eventually grew and triggered a sequence of feedback events, just like the fiducial run P1A. The more powerful bubbles for run P2A ($\epsilon_{\rm m} = 0.5$) only delayed the time of strong cooling a little bit, but for the first 4 Gyr the results are almost indistinguishable. After 5 Gyr, the cluster again starts to oscillate among states that are closely related to the feedback activities. When the mechanical heating efficiency is larger, the feedback is less frequent, more powerful, and more effective in reducing the accretion rate. The reduced accretion rate takes a longer time to grow back to the Eddington rate, so the cluster fluctuates with a timescale of ~ 5 Gyr for run P2A ($\epsilon_{\rm m} = 0.5$), while for run P2B ($\epsilon_{\rm m} = 0.02$) the cluster oscillates with smaller amplitude and timescale.

Despite the overall behaviors are similar, the change in $\epsilon_{\rm m}$ does result in several noticeable trends. First, the growth of the black hole mass is sensitive to the efficiency. For larger efficiencies, the accretion rate is suppressed so that the black hole does not grow as much as when the efficiencies are smaller. Second, efficient mechanical heating produces large entropy floors in the cores. Especially at moments right after an energetic outburst, the entropy profile can have temporary excursions that go beyond observed ranges. This problem may be alleviated by reducing the scaling of the bubble radii (see § 4.3.3). Lastly, for runs with small efficiencies, the temperature profiles sometimes have a peak at the center. This is due to the concentrated thermal energy injection by the quasar mode, which is invoked more frequently in these cases to help the bubbles at high accretion rates. This is an issue shared with all the models which input thermal energy into a small region, such as those jet models with nonzero thermal components (see § 4.3.3). To avoid this undesirable feature of too much quasar-mode feedback, we did a test run identical to P2B ($\epsilon_{\rm m} = 0.02$), but with quasars turned off. We find that pure bubble heating alone with such small efficiencies is insufficient in halting the cooling catastrophe. The accretion rate increases to ~ 100 $\rm M_\odot yr^{-1}$ at $t \simeq 5$ Gyr and generate a huge bubble that essentially blows all the cluster gas away. This puts a lower limit on the mechanical feedback efficiency, as also found by Gaspari et al. (2011b).

Varying the feedback frequency

In the bubble model employed in this paper (Sijacki et al., 2007), the bubbles are inflated when the black hole mass increases its mass by a fraction of $\delta_{\rm BH}$. Therefore, a larger $\delta_{\rm BH}$ corresponds to a longer duration between subsequent bubble events, as can be seen from Figure 4.6.

As shown in Figure 4.6, the amplitudes of variation in the accretion rate and gas proper-

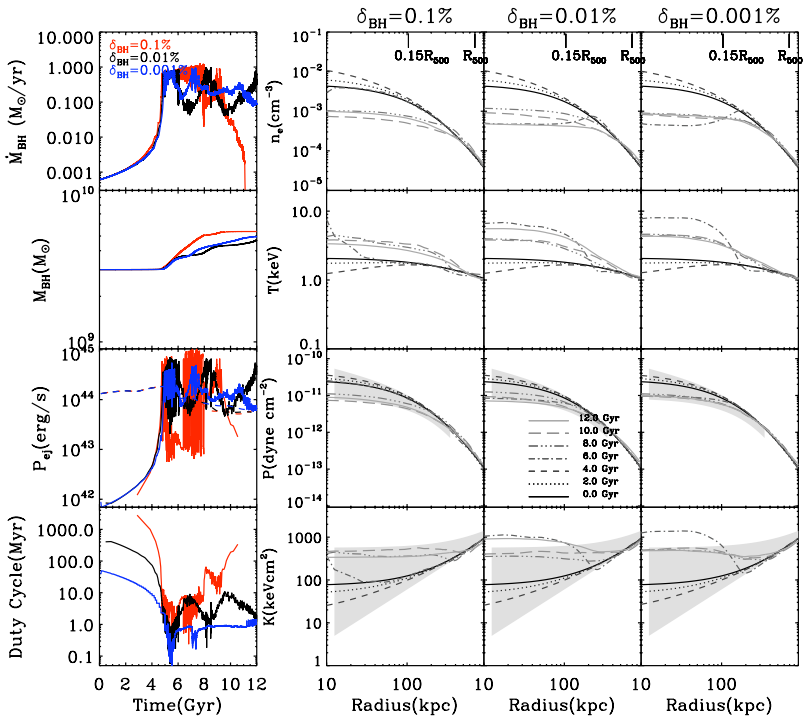

Figure 4.6: Dependence on the threshold for bubble injection (group P3 plus the fiducial run P1A). The threshold, $\delta_{\rm BH}$, is defined to be the minimal fractional increase in black hole mass required to inflate a bubble. Smaller thresholds generate more frequent bubbles.

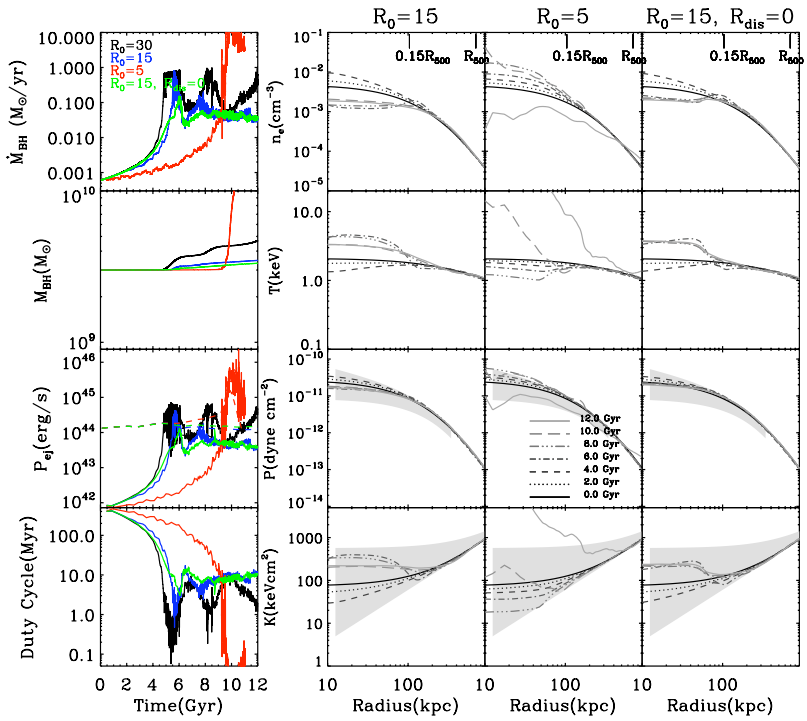

Figure 4.7: Effect of the region for bubble injection (group P4). R_0 is the scaling coefficient for bubble radii as in Eq. 4.4. $R_{\rm dis}$ is the displacement of bubble center from the AGN in unit of the bubble radius. The evolution of SMBH for the fiducial case P1A is plotted using black curves, but its cluster profiles are omitted here (see previous figures).

ties are similar for different $\delta_{\rm BH}$. The increase in temperature and entropy is slightly higher for smaller $\delta_{\rm BH}$, mainly because the injected energy is distributed in a smaller region, as the bubble sizes scale with the injected energy, which is smaller for smaller $\delta_{\rm BH}$ (Eq. 4.3). But compared with the effects of accretion and mechanical heating efficiency, varying $\delta_{\rm BH}$, or the frequency of bubble injection, does not have as large impact on the overall evolution of SMBH and the ICM.

Dependence on the region of feedback

Here we explore the effect of varying the region of bubble injection (group P4), including the scaling coefficient for bubble radii, R_0, as well as the displacement from the central AGN, $R_{\rm dis}$. As in the fiducial case, run P4A and P4B inject bubbles whose centers are randomly displaced within a sphere of radius $R_{\rm dis}$ in unit of the bubble radius, but with smaller bubble

radii. The typical size of bubbles is 100-200 kpc, 50-100 kpc and 20-30 kpc for the fiducial run P1A, run P4A and run P4B, respectively. As shown in Figure 4.7, reducing the bubble sizes is very effective in suppressing the accretion rate because of concentrated heating. The influence on the evolution of cluster core is even more than increasing the heating efficiency (Figure 4.5). In other words, the evolution of SMBH and ICM properties is very sensitive to the choice of bubble radii.

Compared with the fiducial run, the cluster profiles for run P4A ($R_0 = 15\ h^{-1}$kpc) have a smaller flattened core since the energy injection is more concentrated. Note that now the entropy profiles at all times are consistent with the observed range. This implies that the choice of bubble radii is not completely arbitrary. Too large bubbles may produce entropy profiles that are inconsistent with observations.

The size of bubbles cannot be too small either. For run P4B ($R_0 = 5\ h^{-1}$kpc) where small bubbles are randomly injected around the black hole, though concentrated heating greatly slows down cooling and accretion, strong cooling still occurs at $t \simeq 10$ Gyr and generates bubbles that dramatically heat the core. This may be due to the fact that the radius within which the cooling time is less than 10 Gyr is around 100 kpc. So the bubbles only heat a small fraction of gas in the cooling radius, while a substantial amount of gas is still allowed to cool and flow to the center at later times.

We also did one run with bubble center fixed on the central AGN (run P4C, $R_{\rm dis} = 0$). Other parameters are the same as in run P4A ($R_0 = 15\ h^{-1}$kpc, $R_{\rm dis} = 1.0$). From Figure 4.7 we can see that these two runs produce almost identical results, except that fixed bubbles tend to produce less smooth profiles than randomly-positioned bubbles. But these differences are minor. Therefore, as long as the size of bubbles and thus the input energy density are comparable, where around the SMBH to dump the energy has a lesser effect.

In short summary, the size of the region to inject thermal energy (but not so much the displacement from the black hole) is crucial in predicting the evolution of the SMBH and the ICM. Too large bubbles would push too much gas outward and raise the entropy floor to a unrealistic level, while too small bubbles may not be able to heat all the region where it is needed and cause catastrophic cooling. Therefore, for the current bubble model, or any model that requires setting the size of energy injection by hand, it would be difficult to find one parameter or scaling that works for all clusters. And even if the results are permitted by observed limits, the predictions would still be very sensitive to the chosen bubble sizes.

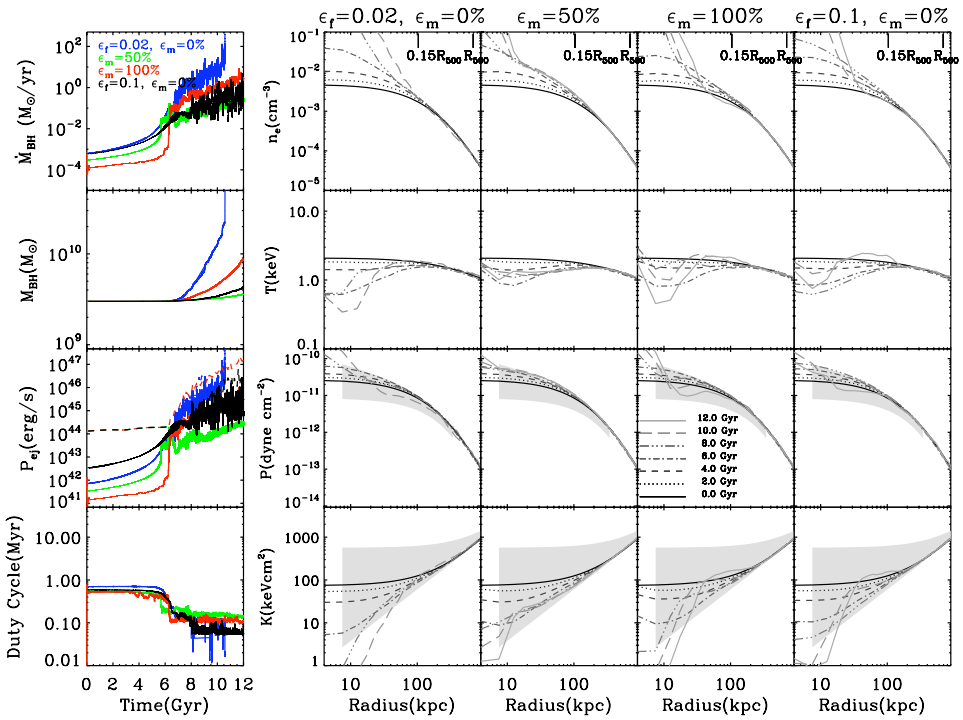

Figure 4.8: Varying the thermal and kinetic efficiencies in the jet feedback model (group P5A-P5D). $\epsilon_{\rm f}$ is the feedback efficiency, i.e., the ratio between total injected energy and the rest mass energy of the SMBH, and $\epsilon_{\rm m}$ is the fraction that goes into thermal energy.

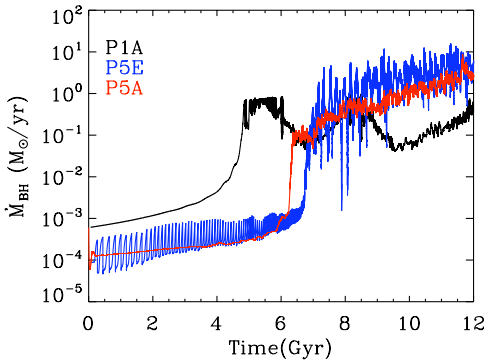

Figure 4.9: Compare the bubble and jet feedback models. Run P1A is the fiducial bubble case, which generates large, randomly-displaced bubbles. Run P5A and P5E have the same net feedback efficiencies, $\epsilon_f \epsilon_m = 0.02$. But run P5A uses purely thermal jets, while run P5E uses tiny, fixed, and almost continuous bubbles to mimic the jet run P5A. This figure demonstrates that the bubble and jet models are numerically consistent when appropriate parameters are chosen. Moreover, their differences are mainly caused by the size of the feedback region.

Effect of thermal to kinetic ratio

In this section we explore the circumstances where the feedback energy is discharged in the form of jet, which has a shape function (Eq. 4.6) aligned with the z-axis, as opposed to spherical bubbles discussed in previous sections. In our generalized parametrization of the jets (Eq. 4.5), the amount of thermal energy and kinetic energy can be tuned by two parameters: ϵ_f, the feedback efficiency or the ratio between total injected energy and the rest mass energy of the SMBH, and ϵ_m, the fraction that goes into thermal energy. The comparison of different thermal to kinetic ratios (group P5A-P5D) is displayed in Figure 4.8.

The first thing to note for the jet models is that the accretion rates are immediately reduced to $\sim 10^{-4} M_\odot yr^{-1}$ as soon as the simulation starts, and it is more so when the thermal efficiency ϵ_m is greater. This suppression is due to the fact that in the jet models, energy is injected within only a few kpc around the AGN, instead of large bubbles that are extended up to tens or hundreds of kpc. As shown in the previous section, decreasing the size of the region to distribute thermal energy can suppress the accretion rate very effectively. Therefore, the jets are just resemblances of tiny bubbles. In order to verify whether the bubble and jet models are self-consistent under similar conditions, we did a run where bubbles with fixed sizes 2 h^{-1} kpc are generated almost continuously (run P5E). Figure 4.9 shows that it indeed reproduces the case P5A of purely thermal jets of identical

net feedback efficiencies, $\epsilon_{\rm f}\epsilon_{\rm m} = 0.02$. The small fluctuations for run P5E just reflect that bubbles are produced every several timesteps rather than perfectly continuous. This test demonstrates that the bubble and jet models are numerically consistent and are degenerate when appropriate parameters are chosen. Moreover, it again emphasizes the point that the choice of the size for energy injection in the AGN subgrid models is nontrivial.

Run P5A-P5C compare different ratios of thermal to kinetic energy, with the total feedback efficiency $\epsilon_{\rm f}$ kept fixed at 0.02. The fraction of energy that goes into thermal energy is 0%, 50%, and 100% for run P5A (purely kinetic), P5B (half thermal half kinetic), and P5C (purely thermal), respectively. As shown in Figure 4.8, all these jet models in general produce similar overall evolution of the accretion rates and cluster profiles. The accretion is halted by concentrated feedback from the beginning so the black hole grows very slowly for the first few Gyr. Since the injected power is smaller than the X-ray luminosity, the cluster gas cools more and more rapidly to a cool-core state at $t \simeq 6$ Gyr, The massive cooling quickly feeds the black hole and grow its mass, which allows the jets to stabilize cooling afterwards. The only exception is run P5A, which fails to overcome catastrophic cooling at $t \simeq 10$ Gyr. So self-regulation of black hole growth may not be achieved by purely kinetic feedback with too small efficiencies.

As expected, the accretion rate is initially more suppressed for higher thermal efficiencies. But interestingly, after $t \simeq 6$ Gyr run P5B ($\epsilon_{\rm m} = 50\%$) becomes the most effective. In other words, the most effective way to stifle cooling is not necessarily dumping all the feedback energy in thermal form, but a combination of thermal and kinetic feedback that facilitates mixing the heated gas with the surroundings.

We also did another run P5D with purely kinetic feedback but higher total feedback efficiency, $\epsilon_{\rm f} = 0.1$. Like run P5A, which is also kinetic but with $\epsilon_{\rm f} = 0.02$, the initial accretion rate is not affected in the beginning since the kinetic energy has not transformed into heat. Their differences become more evident as feedback energy is thermalized and as the jets become more powerful after $t \simeq 6$ Gyr. Note that at later times, the level of suppression is comparable to run P5B. So both raising the total feedback efficiency and tuning the thermal to kinetic ratio can slow down the accretion and black hole growth.

It is also instructive to compare run P5D ($\epsilon_{\rm f} = 0.1$, purely kinetic) with run P5C ($\epsilon_{\rm f} = 0.02$, purely thermal). If their results are comparable, it would imply 20% of the kinetic energy is converted into heat, or a mechanical heating efficiency of 0.2, which is around values commonly assumed in AGN subgrid models using purely thermal feedback (Sijacki et al., 2007; Booth & Schaye, 2009). Recent cosmological simulations also found that either using purely kinetic feedback or purely thermal feedback assuming 15% for the mechanical heating could match the local black hole properties (Dubois et al., 2011). Here we find that

run P5D has somewhat better ability than run P5C to halt cooling, implying possibly a mechanical heating efficiency higher than 20%. Note that small discrepancies are expected because of different sizes of thermal feedback used by different simulations. For our jets the feedback region is confined within the small shape function, whereas simulations mentioned above used either extended bubbles (Sijacki et al., 2007) or the nearest SPH particle (Booth & Schaye, 2009; Dubois et al., 2011). Note also that these arguments are based on simple hydrodynamic simulations, and would change if gas mixing is modified by additional physical effects, such as subgrid turbulence, viscosity, etc.

The resulting cluster profiles again reflects the ability of jets to stop cooling. Since run P5B is the most effective, its temperature decreased and density increased the least. But in general the jets does not expel the gas or heat the gas as much as the bubbles, maintaining the core at the CC state. Note that the density profiles show a dense core of size ~ 10 kpc at later times. This is due to a torus of cold gas formed around the black hole when cooling is happening rapidly. In reality these cold gas should keep condensing to unresolved scales and form stars. This unphysical accumulation of cold gas is treated in previous works using different methods, including removing the cold gas by a sink term in the continuity equation (Gaspari et al., 2011b), or using an effective equation of state appropriate for multiphase gas (Dubois et al., 2010). Since our simulation does not include these treatments, we will avoid deriving quantities that are sensitive to the central densities. For example, we will only use core-excised instead of total X-ray luminosity in Chapter 5 when we discuss cluster observables.

Another thing to note is that any jet with nonzero thermal efficiency (run P5B and P5C) would produce a hot spot surrounding to black hole and hence a peak in the temperature profile near the center, which is also found by Gaspari et al. (2011a) and Dubois et al. (2011). Therefore, we advice simulations using concentrated thermal feedback such as thermal jets or quasar feedback to be cautious about this numerical effect when interpreting results near the region of feedback.

4.4 Summary

In the literature there has been a variety of AGN subgrid models employed in cosmological simulations. However, systematic parameter surveys and comparisons among different implementations are critical for understanding the robustness of their predictions. In this study, we implemented several commonly-adopted accretion and feedback models into FLASH and performed a sensitivity test on these subgrid models to a spectrum of parameters. We

summarize our findings in the following.

1. *Resolution* - The convergence tests show that increasing resolutions generally produces more variable accretion rates. The bubble feedback suffers greater influence by changing the resolution, whereas the jet model is more robust, as long as the radius for computing accretion rates is larger than the sizes of the jets.

2. *Accretion* - The proportionality to relate the Bondi accretion to the actual SMBH accretion rate has a significant impact on the evolution of SMBH and cluster properties. Given the uncertainties in the accretion mechanisms, current AGN subgrid models may have very limited power to predict the evolution of cluster core properties, such as the fraction of CC versus NCC clusters as a function of time.

3. *Efficiency of mechanical heating* - Varying the mechanical heating efficiency does not alter the overall evolution as much as accretion. Feedback with large efficiencies have more variable accretion rates, more suppression in black hole growth, and higher entropy floors. Too small efficiencies would fail to overcome cooling.

4. *Frequency* - Changing the frequencies of injections has a minor effect. Longer duty cycles tend to generate more fluctuations in the accretion rates and cluster profiles.

5. *Region* - The evolution of the SMBH and the ICM is very sensitive to the sizes of energy injections (the displacement from the BH does not matter much). Moreover, too large bubbles would sometimes produce entropy floors that are inconsistent with observations, and too small bubbles may not be able to heat the entire CC and stop catastrophic cooling. Thus for any model that requires setting the feedback sizes by hand, there would be this issue of fine-tuning in order to work for a general population of clusters.

6. *Kinetic feedback* - The jets with varied thermal to kinetic ratios produce very similar results. A combination of thermal and kinetic energy is slightly more efficient than purely thermal feedback. Purely kinetic feedback with too small efficiencies may fail to self-regulate.

Comparing the bubble and jet models, we find that their main difference lies in the sizes of energy injections. They are numerically degenerate when appropriate parameters are chosen, i.e., producing tiny, continuous bubbles to mimic the jets. The jet model is in general more robust to many numerical parameters (e.g. resolution) as well as physical parameters (e.g. sizes of feedback). However, though the jets can maintain the cluster at the CC state, the accumulation of cold gas at the center would need robust treatments. Also, purely thermal concentrated heating, like thermal jets or quasar feedback, would produce a central peak in the temperature profiles. Therefore, one needs to be cautious when interpreting the results in the immediate surroundings of the BH.

Chapter 5

Impact of AGN feedback on global ICM properties

5.1 Introduction

Feedback from active galactic nuclei (AGN) is an important ingredient in the intracluster medium (ICM) of galaxy clusters. Observations of radio jet-inflated bubbles and corresponding X-ray cavities clearly demonstrate interactions between the central supermassive black holes (SMBH) and the cluster atmosphere (McNamara & Nulsen, 2007). Because of their enormous mechanical power and occurrence together with cool cores (CC) (Dunn & Fabian, 2008), AGN feedback has long been proposed to provide extra entropy to explain the self-similar breaking of scaling relations and to remedy the over-cooling problem (see Chapter 1).

Indeed, cosmological simulations including radiative cooling plus stellar feedback, though having reproduced observed cluster profiles outside the cores, still result in density and temperature gradients that are too steep and overproduction of stars at cluster centers (Nagai et al., 2007a). On the other hand, simulations including AGN feedback have shown significant improvements in matching the observed slope of the X-ray luminosity-temperature relation and the suppression of gas fractions (Puchwein et al., 2008).

However, because of our incomplete understanding of the detailed accretion and feedback processes of SMBHs, current AGN models are highly phenomenological, relying on subgrid modeling with simplified assumptions on the accretion and feedback schemes. Furthermore, there have been a variety of different implementations and parameterizations of these subgrid models, such as simulating AGN feedback as thermal energy injections into already-inflated bubbles (Sijacki et al., 2007), or as bipolar jets that carry kinetic energy (Cattaneo & Teyssier, 2007). Uncertainties due to the choices of models and parameters are poorly understood, which substantially limits the predictive power of numerical simulations with AGN feedback. In particular, since cluster integrated properties, including X-ray luminosity, X-ray temperature, and total gas mass, are important mass proxies for deriving cosmological constraints using cluster counts (see Chapter 1), it is essential to quantify the uncertainties of these quantities due to uncertainties in the AGN subgrid models.

In Chapter 4 we have performed a systematic parameter survey for the subgrid models commonly used in the literature and identified the variables to which the models are most sensitive. In this study, we focus on the model predictions for the *global* properties of clusters. In particular, in § 5.2 we first examine whether any model variations produce cluster integrated properties that violate observed scaling relations. Then we quantify the model uncertainties of the observables as functions of overdensity radii. In § 5.3 we analyze the successful models and study the impact of AGN feedback on the scaling relations. We refer the reader to Chapter 4 for details of the subgrid models, and to Table 4.3 for a summary of the simulation parameters used in this study.

5.2 Robustness of integrated properties

As seen in the previous chapter, specific models or parameters chosen can result in quite discrepant predictions for the evolution of the cluster profiles. Although the influence of AGN feedback is strongest in the core region, we may ask whether, under the influence of this feedback, the global cluster properties can still preserve the observed scalings. The robustness of integrated quantities (e.g. measured within R_{500}) is particularly crucial for cluster cosmology. Since current constraints are often derived using calibrations of the mass-observable relations informed by numerical simulations, it is necessary to quantify the systematic uncertainties due to incomplete knowledge of the details of AGN feedback processes.

5.2.1 Consistency with observations

The first question we wish to address is whether any of the model variations explored in the previous chapter predicts global cluster properties that violate the observed scaling relations. To this end we compute several observable quantities integrated within a sphere with radius R_{500}, including the gas mass $M_{\rm g}$, spectral-like temperature $T_{\rm sl}$ (Mazzotta et al., 2004), X-ray luminosity L_X, integrated Compton y parameter due to the Sunyaev-Zel'dovich (SZ) effect (Sunyaev & Zeldovich, 1972), and its X-ray analog $Y_X \equiv M_{\rm g} T_X$ (Kravtsov et al., 2006). Since the spectral-like temperature and the X-ray luminosity are very sensitive to dense and cold gas, we excised the core region ($< 0.15 R_{500}$) in order to avoid numerical effects due to the cold gas accumulated around the SMBH as described in § 4.3.3. For run P4C ($R_0 = 5\ h^{-1}$ kpc) and run P5A ($\epsilon_{\rm f} = 0.02$, $\epsilon_{\rm m} = 0\%$), the evolution after 9 Gyr is not included because these runs encounter cooling catastrophes.

Figure 5.1 compares the trajectories of observables to the scaling relations for the model variations explored in § 4.3.3. Each column compares results for a particular group in

Table 4.3, including variations in the accretion model, mechanical heating efficiency, feedback frequency, region of feedback, and thermal to kinetic ratio. From top to bottom we show the $M_{\rm g}$–$T_{\rm sl}$, L_X–$T_{\rm sl}$, Y_{SZ}–L_X, and Y_{SZ}–Y_X relations and overplot with the observed relations and scatter for the REXCESS sample (Croston et al., 2008; Pratt et al., 2009; Arnaud et al., 2010) for comparison. Note that the offsets in the normalizations compared to the observed relations are partly due to differences in R_{500}. The observed values of R_{500} in these studies are obtained by matching the empirical M_{500}–Y_X relation by Arnaud et al. (2007). As these authors point out, their hydrodynamic mass M_{500} may underestimate the true mass. Therefore it is likely that their R_{500} is smaller than that used in our computation, which lowers the values of $M_{\rm g}$ and L_X, but increases $T_{\rm sl}$, in a direction that could explain the discrepancy. Moreover, the X-ray luminosity in our calculation is bolometric and hence would be higher than the observed values, which are integrated over the energy range $0.1-2.4$ keV.

We find that despite the variation in the predicted cluster profiles produced by different subgrid models, the integrated properties for all the models evolve with amplitudes that are consistent with the observed scatter. In other words, when cooling is regulated, all the subgrid models are able to preserve global cluster properties as observed. This result gives us some confidence in the AGN subgrid models employed in cosmological simulations. However, it also implies that these various models and parameters cannot be distinguished by constraints on the integrated quantities, but must be constrained by observations that are more sensitive to cluster cores.

5.2.2 Model uncertainties

Although none of the individual trajectories in Figure 5.1 violates the observed scaling relations, when compared against each other, the predictions for a particular observable at a particular time can still vary significantly among models. Thus the second question to ask is: how large are the theoretical uncertainties due to different AGN subgrid models and variations in their parameters? Since AGN feedback is expected to have more impact at smaller radii, we compute the observables measured within several commonly-quoted overdensities, including R_{2500}, R_{1000}, R_{500}, and R_{200}, and compare their values with the fiducial runs, i.e., run P1A for the bubble model and run P4D for the jet model. The relative dispersion for a given observable O is computed by $\Delta O \equiv |O - O_{\rm fiducial}|/O_{\rm fiducial}$. The results for five observables ($T_{\rm sl}$, $M_{\rm g}$, L_X, Y_{SZ}, and Y_X) with varied subgrid models are presented in Figure 5.2.

Comparing the five observables, the X-ray luminosity has the largest uncertainties due

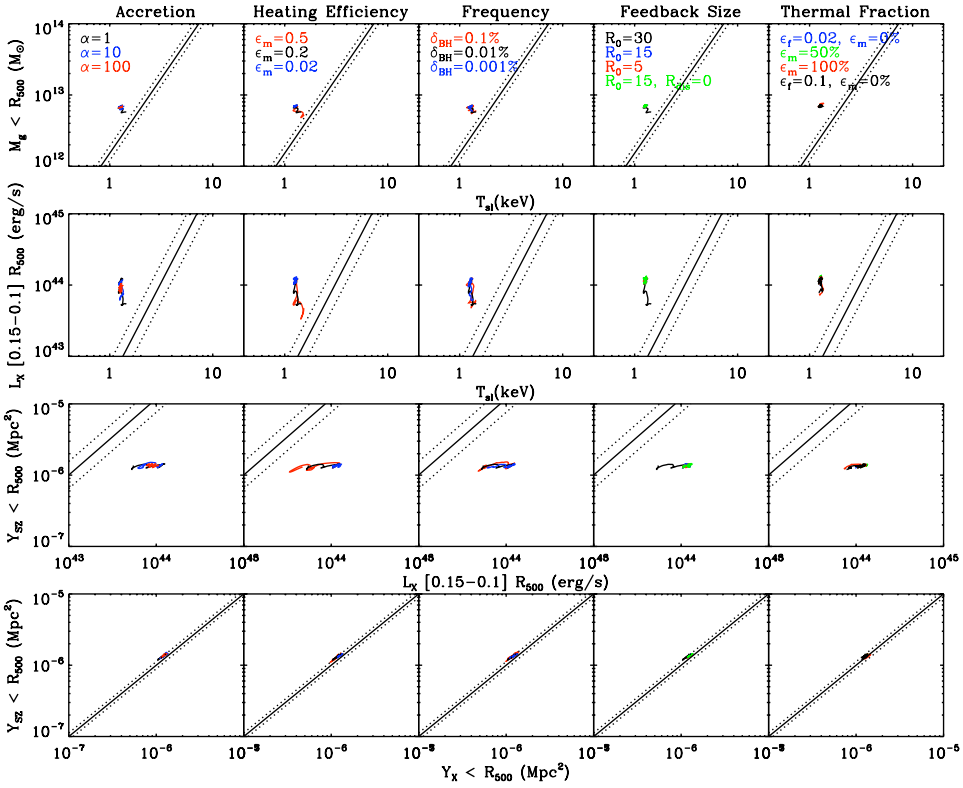

Figure 5.1: Trajectories of integrated observable properties compared to observed scaling relations for variations of physical parameters explored in § 4.3.3. The rows from top to bottom show the $M_{\rm g}$–$T_{\rm sl}$, L_X–$T_{\rm sl}$, Y_{SZ}–L_X, and Y_{SZ}–Y_X relations, respectively (see text for detailed definitions). The columns from left to right plot the runs with varied accretion model (group P1, Figure 4.4), mechanical heating efficiency (group P2, Figure 4.5), frequency of feedback (group P3, Figure 4.6), region of feedback (group P4, Figure 4.7), and thermal to kinetic ratio (group P5, Figure 4.8), respectively. Overplotted are observed relations (solid) and r.m.s scatter (dashed) for the REXCESS sample (Croston et al., 2008; Pratt et al., 2009; Arnaud et al., 2010). This figure shows that, despite the variation in detailed evolution produced by different subgrid models, the integrated cluster observables still evolve with amplitudes that are consistent with the observed scatter.

Table 5.1: Model Uncertainties for Observables Measured within Various Overdensity Radii.

	$\Delta = 2500$	1000	500	200
$\Delta T_{\rm sl}$	40.6%	19.0%	7.1%	4.4%
$\Delta M_{\rm g}$	116.2%	58.5%	24.3%	6.0%
ΔL_X	303.2%	188.6%	136.8%	113.6%
ΔY_{SZ}	48.4%	25.6%	13.2%	8.8%
ΔY_X	46.3%	28.3%	19.6%	7.4%

[1] Model uncertainties correspond to the maximum values across all models shown in Figure 5.2.

to variations in subgrid models (note that its plotting range is $0 - 200\%$), and the gas mass is second. The other three variables ($T_{\rm sl}$, Y_{SZ}, and Y_X) are more robust. When different groups of model variations are contrasted, we find that the mechanical heating efficiency and the size of the feedback region cause the largest variations in the predicted observables. The influence of the accretion models and feedback frequency is smaller, and the thermal to kinetic ratio has the least impact.

As expected, since feedback from the AGN is more influential toward the central SMBH, the model uncertainties are biggest for observables measured within R_{2500}. When quantities are integrated out to R_{200}, the uncertainties become small for all observables except the X-ray luminosity, because a large fraction of the total luminosity still comes from regions near the core. In Table 5.1 we summarize the maximum uncertainties among all models for each cluster observable versus the overdensity radius. We find that in general observables that depend on gas densities are more poorly predicted. The total gas mass predicted by different models has uncertainties ranging from a few percent at R_{200}, to $\sim 20\%$ at R_{500}, to $\sim 100\%$ at R_{2500}. Thus the X-ray luminosity, which is proportional to density squared, can vary by factors of a few for all radii. The level of uncertainties is comparable for $T_{\rm sl}$, Y_{SZ}, and Y_X, ranging from $\sim 40 - 50\%$ at R_{2500}, to $\sim 10 - 20\%$ at R_{500}, to $\sim 5 - 10\%$ at R_{200}.

The integrated Compton y parameter, Y_{SZ}, and its X-ray analog, Y_X, are considered very good cluster mass proxies because previous simulations (without AGN feedback) show that they have very small mass scatter (Kravtsov et al., 2006) and they are relatively insensitive to cluster dynamical states (Poole et al., 2007; Yang et al., 2010). Therefore their scaling relations are often provided by numerical simulations for calibration in observational studies (Arnaud et al., 2010) or for deriving cosmological constraints (Mantz et al., 2008; Vikhlinin et al., 2009; Vanderlinde et al., 2010). However, we find that incomplete knowledge of the processes of AGN feedback puts a limit on the predictive power of current cosmological

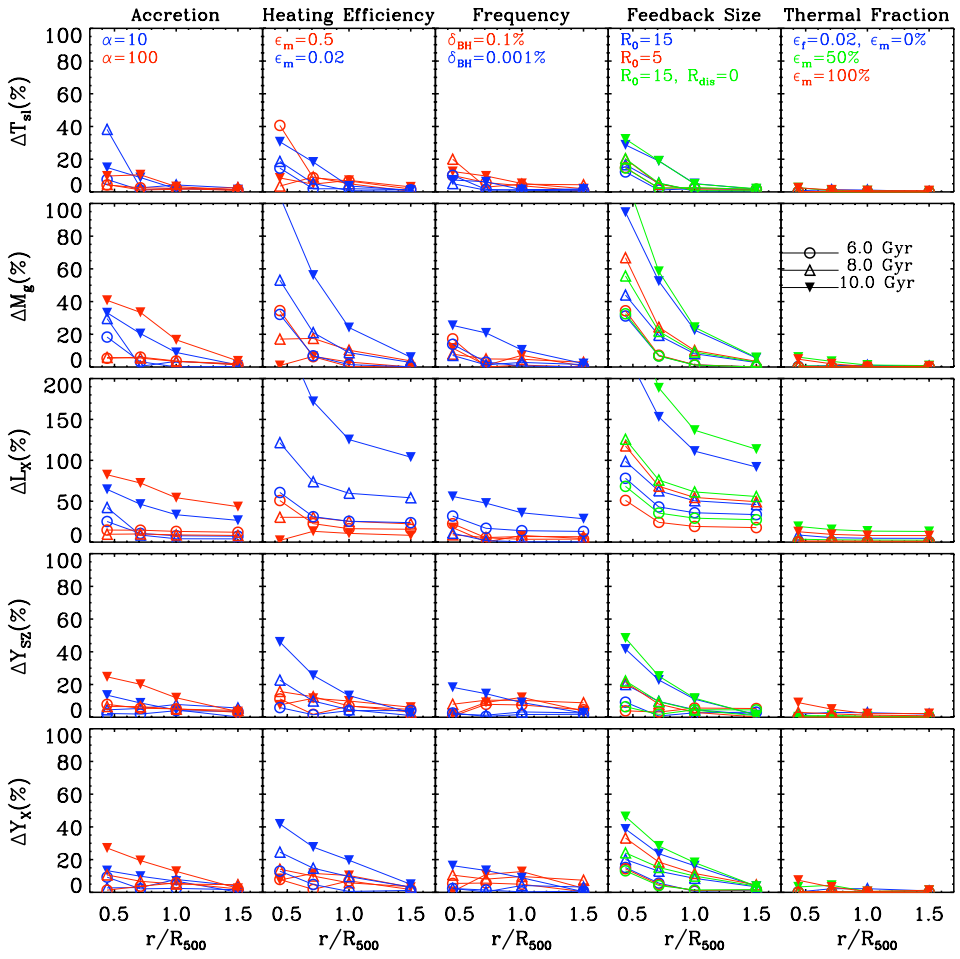

Figure 5.2: Uncertainties in cluster integrated properties due to AGN subgrid model variations (see Figure 5.1 for explanations of the columns). Plotted are the predictions of $T_{\rm sl}$, $M_{\rm g}$, L_X, Y_{SZ}, and Y_X (top to bottom) relative to the fiducial runs as functions of four overdensity radii within which the observables are integrated, including R_{2500}, R_{1000}, R_{500} and R_{200}. Each color corresponds to a specific run, and each line represents the result at a particular simulation time. Note that the plotting range for the X-ray luminosity is $0-200\%$, since it has the largest uncertainty due to model variations. $T_{\rm sl}$, Y_{SZ}, and Y_X are more robust. Comparing different groups of model variations (i.e. by columns), we find that the mechanical heating efficiency and size of feedback region are the most influential, while feedback frequency and thermal to kinetic ratio play a minor role.

simulations. Even for these most robust variables, the theoretical uncertainties are $\sim 10-20\%$ at R_{500} and $\sim 5-10\%$ at R_{200}, comparable to other main sources of systematic errors reported in the literature, such as the bias of hydrostatic mass due to non-thermal pressure support (e.g. Lau et al., 2009). Those variables that depend on gas density (e.g. L_X in particular) are even more uncertain. In order to improve cluster cosmology to the percent level, it is essential for numerical simulations to focus on how to constrain the subgrid physics before making various predictions.

5.3 Impact of AGN feedback on the scaling relations

Keeping in mind the model uncertainties of integrated properties shown in the previous section due to different evolution in each model, next we study some general trends predicted by all the models. In particular, we probe the impact of AGN outbursts on the cluster observables using cross-correlations among them. Note that in this study we focus on the *global* observable properties, that is, whether there will be observable features beyond the core due to the disturbances introduced by the central AGN. The influence on the core properties by AGN has been discussed extensively in previous works (see McNamara & Nulsen (2007) and references therein) and will be a part of our future work.

5.3.1 Correlations between observables and AGN activity

Figure 5.3 (top row) plots the evolution of the AGN power, X-ray luminosity, and spectral-like temperature for all the bubble runs listed in Table 4.3. The jet runs are not shown here because their AGN power cannot be compared directly in the thermal form. However, their results can be well represented by the jet-like bubble run P5E, as discussed in section § 4.3.3 (see also Figure 4.9). For all the models, the black hole self-regulates its growth when its feedback power is sufficient to balance the radiative losses by the cluster. However, the feedback power fluctuates around the mean after $t \simeq 6$ Gyr with different amplitudes depending on the initial configurations and growth at earlier times. These fluctuations are present in the AGN activity as well as in the cluster observables. Taking run P2B (red curve) as an illustration, the strong AGN outbursts at $t \simeq 5-6$ Gyr raise the entropy of the gas and hence induce the decrease in luminosity and increase in temperature at $t \simeq 6-7$ Gyr. Similar effects can be seen for the peak in AGN activity around $t \simeq 10$ Gyr and corresponding fluctuations in the observables at $t \simeq 11$ Gyr.

We therefore compare the AGN power with the luminosity and temperature after $t = 6$ Gyr (bottom row in Figure 5.3) to see whether their fluctuations are correlated. The

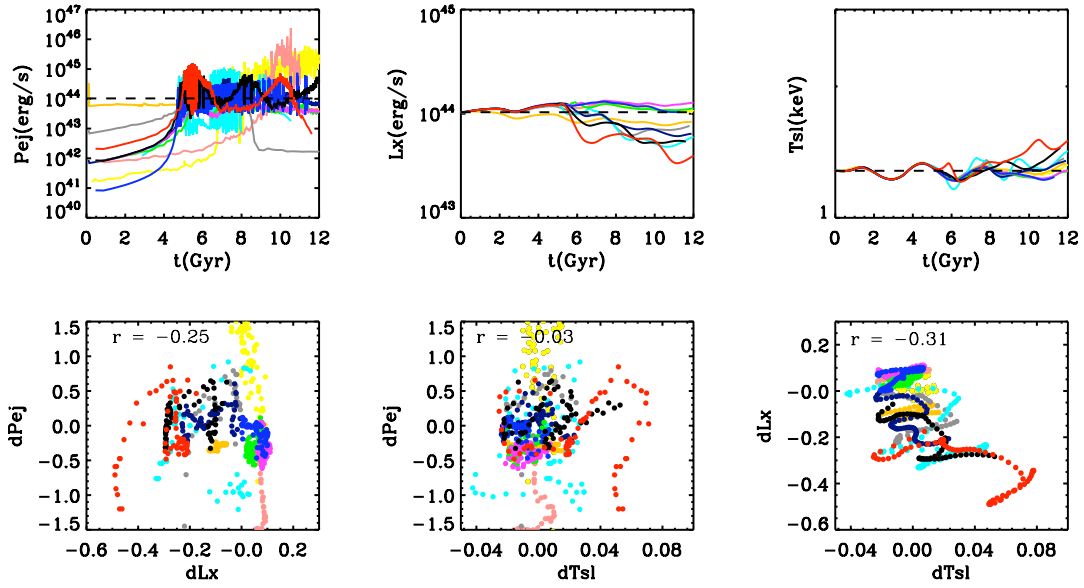

Figure 5.3: *Top*: Evolution of the AGN power, X-ray luminosity, and spectral-like temperature (the latter two measured within R_{500}), respectively. All the bubble runs in Table 4.3 are shown using different colors. *Bottom*: Correlations among these three variables for data points after $t = 6$ Gyr (r is the correlation coefficient). Because AGN outbursts result in delayed reduction of the luminosity and heating of the cluster, the correlations between the AGN power and observables are weak, but the luminosity and temperature are anti-correlated.

luminosity and temperature plotted are logarithmic deviations from their initial values; the feedback power is with respect to the initial luminosity too. The correlation coefficients are given by the Spearman Rank-Order Correlation test (Press et al., 1992). As expected, there is a negative (positive) correlation between the feedback power and the luminosity (temperature). However, the trends are not so obvious visually, perhaps due to the phase shifts between the peak AGN events and the delayed responses of the ICM. Nevertheless, since the luminosity and temperature react to the feedback *in phase*, they have a strong anti-correlation as the system moves in the L_X–$T_{\rm sl}$ plane.

Recall that the ranges of trajectories on the L_X–$T_{\rm sl}$ plane predicted by all the AGN subgrid models are comparable to the observed scatter (Figure 5.1). This implies that AGN feedback can drive a significant amount of the observed scatter in the L_X–$T_{\rm sl}$ relation because of the anti-correlation between luminosity and temperature during the feedback events. This is in contrast to other physical processes such as cluster mergers, which tend to move the clusters along the scaling relations (Yang et al., 2009).

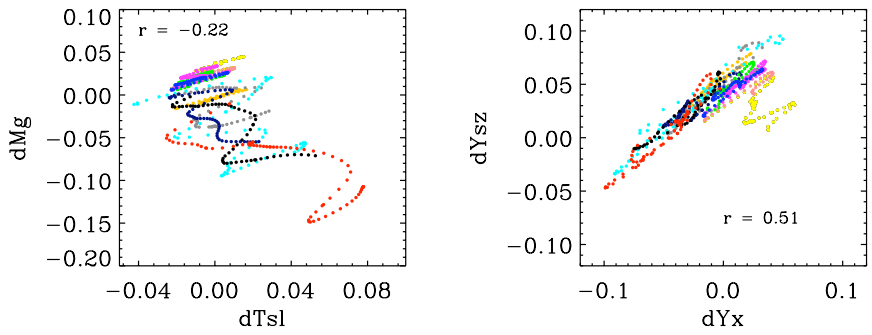

Figure 5.4: Trajectories on the $M_{\rm g}$–$T_{\rm sl}$ (left) and the Y_{SZ}–Y_X (right) planes (r is the correlation coefficient). As with the L_X–$T_{\rm sl}$ relation, variations in $M_{\rm g}$ and $T_{\rm sl}$ are anti-correlated. As a result, there is a tight positive correlation between Y_{SZ} and Y_X.

Similarly, an anti-correlation exists between $M_{\rm g}$ and $T_{\rm sl}$ (Figure 5.4, left panel), which may also contribute to the scatter in the $M_{\rm g}$–$T_{\rm sl}$ relation. But at the same time, it also preserves the tight Y_{SZ}–Y_X relation (right panel) since both Y parameters are essentially the products of $M_{\rm g}$ and $T_{\rm sl}$. Therefore, we find that the Y parameters are robust even under the strong influence of energetic AGN outbursts, which adds another reason why they are excellent tracers of cluster masses.

5.3.2 Scatter in the L_X–T_X relation

Since we have demonstrated that the scatter in the L_X–$T_{\rm sl}$ relation can be induced by feedback events, in Figure 5.5 (right panel) we correlate the L_X–$T_{\rm sl}$ scatter with the AGN power. Since we do not have a sample of clusters to derive the mean scaling relation, the scatter is computed by taking the logarithmic deviation from the observed relation shown in Figure 5.1. As expected from the correlations found in the previous section, a negative correlation exists between the scatter and the AGN power. However, again the trend is not prominent because of the phase shifts (see § 5.3.1).

This result may have implications for observational studies that attempt to connect the L_X–$T_{\rm sl}$ scatter to the AGN radio power. Croston et al. (2005) found that radio loud AGN preferentially lie below the L_X–T_X relation as evidence for AGN heating. However, a more recent study by Jetha et al. (2007) found a weaker relation. For illustration we plot the epochs when the AGN power is 0.5 dex more (less) than the zero-point value in filled (open) symbols (for clarity only data points at multiples of one Gyr are shown). As can be seen in the left panel of Figure 5.5, there is no clear segregation on the L_X–$T_{\rm sl}$ plane between

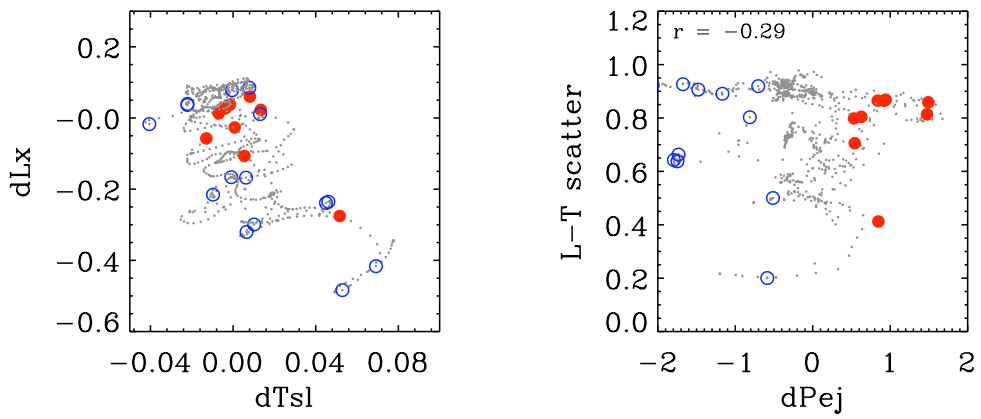

Figure 5.5: Trajectories on the L_X–$T_{\rm sl}$ plane (left) and correlation between its log scatter and the AGN power (right; r is the correlation coefficient). Outbursts that are 0.5 dex more (less) powerful than the mean are marked in red filled circles (blue open circles). More powerful AGN preferentially have smaller scatter (lie below the mean); however, the correlation is diluted by the phase shift between the AGN power and the observables shown in Figure 5.3.

the more powerful and the more quiescent populations, because the correlation between the scatter and AGN power is not strong enough (right panel). If the radio loudness is (roughly) proportional to the power of AGN, this may explain why observationally it is difficult to find a strong correspondence for a sample of clusters.

The scatter in the L_X–T_X relation has long been known to be dominated by the core properties of clusters; excluding the emissions inside the core region can significantly reduce the scatter (e.g. Allen & Fabian, 1998; Pratt et al., 2009). Moreover, CC clusters generally have a higher normalization on the plane than NCC clusters. Here we explicitly show in Figure 5.6 that such a trend can be caused by the effects of AGN. During the AGN feedback events, the L_X–$T_{\rm sl}$ scatter is anti-correlated with the cooling time (right panel). Thus the CC and WCC clusters tend to lie on the upper half of the relation compared to NCC clusters (left panel). Note however that the NCC clusters at later times in the simulations are mostly produced by models in which the AGN are either very powerful (high mechanical heating efficiency) or very extended (large bubble sizes). Therefore the exact amplitude of this segregation of CC and NCC clusters would depend upon the degree of constraints on the subgrid models. Also note that the luminosity and temperature studied here are core-excluded. Therefore, even stronger trends are expected to be found for the core-included L_X–T_X relation.

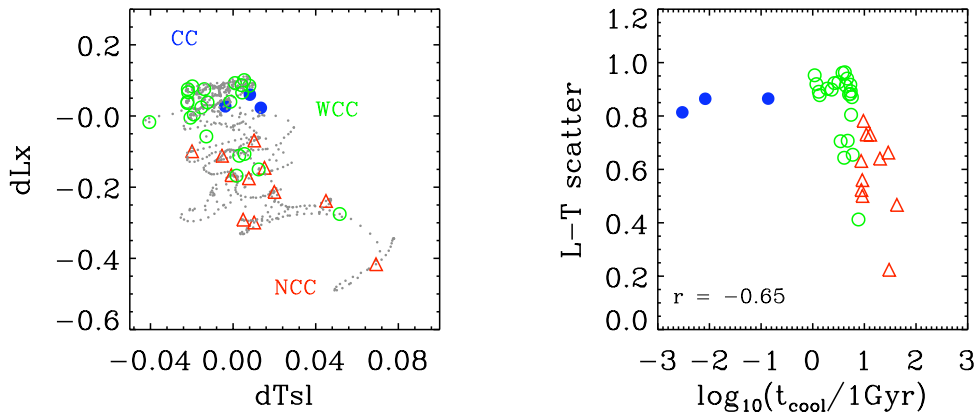

Figure 5.6: Trajectories on the L_X–$T_{\rm sl}$ plane (left) and correlation of its log scatter with the cooling time in the cluster core (right; r is the correlation coefficient). Points for CC, WCC, and NCC clusters are plotted with blue filled circles, green open circles, and red open triangles, respectively. A clear anti-correlation exists between the L_X–$T_{\rm sl}$ scatter and the cooling time, so that CC clusters tend to lie above the mean relation.

5.4 Summary

Outbursts from AGN are energetic events that can greatly influence the observable properties of galaxy clusters. Previous simulations with AGN subgrid models have either studied their impact inside cluster cores (Gaspari et al., 2011b; Dubois et al., 2010), or focused on matching the observed scalings of SMBH evolution and cluster gross properties (Sijacki et al., 2007; Booth & Schaye, 2009; Puchwein et al., 2008). However, whether these models can simultaneously reproduce cluster properties both inside and outside the cores has not previously been demonstrated. In the previous chapter we carried out a detailed study of different models and parameters and identified which can self-regulate and produce profiles consistent with observations inside the cores. In this study, we focus on their predictions of integrated properties. Our findings are summarized as follows.

1. All the subgrid models that successfully regulate cooling in the previous analysis also produce integrated quantities consistent with observed scaling relations, as shown in Figure 5.1.

2. The model uncertainties in $M_{\rm g}$, $T_{\rm sl}$, L_X, Y_{SZ}, and Y_X as functions of overdensity radii are quantified in Table 5.1. Quantities that depend on gas density (e.g. $M_{\rm g}$, L_X) are more uncertain, whereas $T_{\rm sl}$, Y_{SZ}, and Y_X are most robust to model variations, to the levels of $\sim 10-20\%$ at R_{200}, and $\sim 5-10\%$ at R_{200}.

3. Since AGN feedback reduces gas density and raises temperature, anti-correlations exist between L_X and $T_{\rm sl}$ and also between $M_{\rm g}$ and $T_{\rm sl}$, contributing to the intrinsic scatter in these two scaling relations. However, because the ICM reacts to AGN feedback with a delay, correlations between observables and AGN power are weak.

4. Because $M_{\rm g}$ and $T_{\rm sl}$ are anti-correlated, even under the influence of strong AGN outbursts, the Y_{SZ} and Y_X parameters are still robust mass proxies.

Chapter 6

Conclusions

Clusters of galaxies are invaluable cosmological probes, provided that the astrophysical processes underlying their mass-observable relations can be well understood. Studying the sources of the intrinsic scatter in the scaling relations can not only provide valuable insights into the formation of clusters, but also help identify possible systematics and improve mass estimates for better cosmological constraints. In this work we used numerical simulations to investigate the impact of cluster structure, dynamical state, radiative cooling, and feedback from active galactic nuclei (AGN) on cluster X-ray and Sunyaev-Zel'dovich (SZ) scaling relations. The important implications for cluster cosmology are discussed.

We first examined whether cluster merger events would cause a selection bias. Analyzing the X-ray and SZ scaling relations derived from a sample of simulated clusters, we find that *statistically* the effects of mergers are minor. This counterintuitive result is mainly due to a few combined factors: the rareness of major mergers, the partial cancellation of effects of shock heating and incomplete virialization, and the fact that even during major mergers, observables tend to move along the scaling relations.

We then studied the influence of cluster internal structures. We find that the mass-observable scatter strongly correlates with the concentration of clusters, which is expected from expressing the virial theorem in terms of the overdensity quantities. Such strong correlations with a third parameter can potentially be applied to observed signals to reduce the scatter and tighten the scaling relations.

We examined the assumption of lognormal scatter distributions, commonly used in self-calibration studies. Due to the sensitivity of SZ flux to structures along the line of sight, we find that the positive tail in the distribution of the Y_{SZ}–M scatter would cause enough skewness and kurtosis to have non-negligible effects on cosmological parameter constraints. Fortunately, we also find that the errors in X-ray and SZ mass proxies are not correlated. So it is possible to identify the outliers by combining X-ray and SZ mass estimates.

Note, however, that the above results are derived from adiabatic hydrodynamic simulations. Therefore we expect our findings will be most relevant to observed scaling relations for core-excluded quantities, which are dominated by gravitational effects instead of the

complicated baryonic physics inside cluster cores.

Our understanding of the properties of the intracluster medium (ICM) cannot be complete without considering the balance between radiative cooling and heating. In order to provide a firm foundation to cosmological simulations with AGN feedback, we performed a systematic sensitivity study on a variety of accretion and feedback models of supermassive black holes (SMBH) within an idealized cluster atmosphere. We find that the evolution of SMBH activity and ICM profiles is most sensitive to the strength of accretion, the mechanical heating efficiency, and the size of the region used to inject feedback energy, while the frequency of feedback and the ratio between thermal and kinetic energy have minor effects. Feedback using jet injection is generally more robust to parameter variations compared to injecting thermal energy into large bubbles.

These uncertainties in the modeling details translate into theoretical uncertainties in the predictions for cluster global properties. We estimated the model uncertainties for several observables integrated within a few overdensity radii. We find that quantities that are related to gas density, such as the total gas mass and the X-ray luminosity, are poorly predicted. The X-ray temperature, integrated SZ flux, and the X-ray analog of SZ flux are more robust, but the levels of uncertainty are $5-10\%$ at R_{200} and $10-20\%$ at R_{500}, which are comparable to other known sources of systematic errors (e.g. hydrostatic mass bias). Further improvement would thus require more constraints, both theoretical and observational, on the accretion mechanisms and mechanical heating efficiencies in the AGN models.

As for the impact of AGN feedback on the scaling relations, we find that outbursts from AGN can result in anti-correlation between variations in the total gas mass and temperature. This anti-correlation may be a source of intrinsic scatter in the $M_{\rm g}$–T_X relation and L_X–T_X relations. The same anti-correlation also makes the Y parameters robust mass proxies even during energetic AGN events.

Note also that our current knowledge of the ICM is mainly based on inviscid, unmagnetized hydrodynamics. As mentioned in the introduction, magnetic fields and the corresponding transport processes may be important in some circumstances. For example, AGN-injected magnetic field in the ICM may suppress accretion into cluster centers (Sutter, 2011). The jet-ICM interactions would also change in the presence of magnetic fields and/or anisotropic conduction and viscosity. Observational data from radio telescopes in the near future will significantly improve our understanding of the non-thermal components of clusters, which is crucial for properly modeling the ICM.

The study of galaxy cluster scaling relations has been fruitful and will continue to yield more interesting results as the fields of cluster astrophysics and cosmology advance together.

References

Allen, S. W., Dunn, R. J. H., Fabian, A. C., Taylor, G. B., & Reynolds, C. S. 2006, MNRAS, 372, 21

Allen, S. W., Evrard, A. E., & Mantz, A. B. 2011, arXiv:1103.4829

Allen, S. W., & Fabian, A. C. 1998, MNRAS, 297, L57

Allen, S. W., Rapetti, D. A., Schmidt, R. W., Ebeling, H., Morris, R. G., & Fabian, A. C. 2008, MNRAS, 383, 879

Andersson, K., et al. 2010, arXiv:1006.3068

Arnaud, K. A. 1996, in ASP Conf. Ser., Vol. 101, Astronomical Data Analysis Software and Systems V, ed. G. H. Jacoby & J. Barnes, 17

Arnaud, M., Pointecouteau, E., & Pratt, G. W. 2005, A&A, 441, 893

—. 2007, A&A, 474, L37

Arnaud, M., Pratt, G. W., Piffaretti, R., Böhringer, H., Croston, J. H., & Pointecouteau, E. 2010, A&A, 517, A92+

Ascasibar, Y., Sevilla, R., Yepes, G., Müller, V., & Gottlöber, S. 2006, MNRAS, 371, 193

Bagla, J. S. 2002, Journal of Astrophysics and Astronomy, 23, 185

Bailin, J., & Steinmetz, M. 2005, ApJ, 627, 647

Balogh, M. L., Babul, A., Voit, G. M., McCarthy, I. G., Jones, L. R., Lewis, G. F., & Ebeling, H. 2006, MNRAS, 366, 624

Barnes, J., & Hut, P. 1986, Nature, 324, 446

Basilakos, S., Plionis, M., & Maddox, S. J. 2000, MNRAS, 316, 779

Bernardeau, F., & Kofman, L. 1995, ApJ, 443, 479

Bertschinger, E. 2001, ApJS, 137, 1

Bhattacharya, S., di Matteo, T., & Kosowsky, A. 2008, MNRAS, 389, 34

Bhattacharya, S., Heitmann, K., White, M., Lukić, Z., Wagner, C., & Habib, S. 2011, ApJ, 732, 122

Bialek, J. J., Evrard, A. E., & Mohr, J. J. 2001, ApJ, 555, 597

Bîrzan, L., Rafferty, D. A., McNamara, B. R., Wise, M. W., & Nulsen, P. E. J. 2004, ApJ, 607, 800

Blinnikov, S., & Moessner, R. 1998, A&AS, 130, 193

Bode, P., Ostriker, J. P., & Vikhlinin, A. 2009, ApJ, 700, 989

Bode, P., Ostriker, J. P., Weller, J., & Shaw, L. 2007, ApJ, 663, 139

Bondi, H. 1952, MNRAS, 112, 195

Booth, C. M., & Schaye, J. 2009, MNRAS, 398, 53

Borgani, S. 2006, arXiv:0605575

Borgani, S., & Kravtsov, A. 2009, arXiv:0906.4370

Borgani, S., et al. 2004, MNRAS, 348, 1078

Brodwin, M., et al. 2010, ApJ, 721, 90

Brüggen, M., & Kaiser, C. R. 2001, MNRAS, 325, 676

Brüggen, M., Scannapieco, E., & Heinz, S. 2009, MNRAS, 395, 2210

Bryan, G. L., & Norman, M. L. 1998, ApJ, 495, 80

Bullock, J. S., Kolatt, T. S., Sigad, Y., Somerville, R. S., Kravtsov, A. V., Klypin, A. A., Primack, J. R., & Dekel, A. 2001, MNRAS, 321, 559

Buote, D. A., Gastaldello, F., Humphrey, P. J., Zappacosta, L., Bullock, J. S., Brighenti, F., & Mathews, W. G. 2007, ApJ, 664, 123

Buote, D. A., & Tsai, J. C. 1995, ApJ, 452, 522

—. 1996, ApJ, 458, 27

Calder, A. C., et al. 2002, ApJS, 143, 201

Carilli, C. L., & Taylor, G. B. 2002, ARA&A, 40, 319

Cattaneo, A., & Teyssier, R. 2007, MNRAS, 376, 1547

Cavagnolo, K. W., Donahue, M., Voit, G. M., & Sun, M. 2009, ApJS, 182, 12

Churazov, E., Brüggen, M., Kaiser, C. R., Böhringer, H., & Forman, W. 2001, ApJ, 554, 261

Churazov, E., Sazonov, S., Sunyaev, R., Forman, W., Jones, C., & Böhringer, H. 2005, MNRAS, 363, L91

Cohn, J. D., & White, M. 2005, Astroparticle Physics, 24, 316

—. 2009, MNRAS, 393, 393

Cole, S., & Lacey, C. 1996, MNRAS, 281, 716

Colella, P., & Woodward, P. R. 1984, Journal of Computational Physics, 54, 174

Comerford, J. M., Moustakas, L. A., & Natarajan, P. 2010, ApJ, 715, 162

Comerford, J. M., & Natarajan, P. 2007, MNRAS, 379, 190

Conroy, C., & Ostriker, J. P. 2008, ApJ, 681, 151

Cooray, A., & Sheth, R. 2002, Phys. Rep., 372, 1

Croston, J. H., Hardcastle, M. J., & Birkinshaw, M. 2005, MNRAS, 357, 279

Croston, J. H., et al. 2008, A&A, 487, 431

Croton, D. J., et al. 2006, MNRAS, 365, 11

Cunha, C. 2009, Phys. Rev. D, 79, 063009

Cunha, C. E., & Evrard, A. E. 2010, Phys. Rev. D, 81, 083509

da Silva, A. C., Kay, S. T., Liddle, A. R., & Thomas, P. A. 2004, MNRAS, 348, 1401

Dai, X., Bregman, J. N., Kochanek, C. S., & Rasia, E. 2010, ApJ, 719, 119

Di Matteo, T., Springel, V., & Hernquist, L. 2005, Nature, 433, 604

Dolag, K., Bartelmann, M., Perrotta, F., Baccigalupi, C., Moscardini, L., Meneghetti, M., & Tormen, G. 2004, A&A, 416, 853

Dolag, K., Evrard, A., & Bartelmann, M. 2001, A&A, 369, 36

Dolag, K., & Schindler, S. 2000, A&A, 364, 491

Dolag, K., Vazza, F., Brunetti, G., & Tormen, G. 2005, MNRAS, 364, 753

Donahue, M., Horner, D. J., Cavagnolo, K. W., & Voit, G. M. 2006, ApJ, 643, 730

Dubey, A., Reid, L. B., & Fisher, R. 2008, Physica Scripta, T132, 014046

Dubois, Y., Devriendt, J., Slyz, A., & Teyssier, R. 2010, MNRAS, 409, 985

Dubois, Y., Devriendt, J., Teyssier, R., & Slyz, A. 2011, arXiv:1104.0171

Duffy, A. R., Schaye, J., Kay, S. T., & Dalla Vecchia, C. 2008, MNRAS, 390, L64

Dunn, R. J. H., & Fabian, A. C. 2008, MNRAS, 385, 757

Evrard, A. E., & Henry, J. P. 1991, ApJ, 383, 95

Fabian, A. C. 1994, ARA&A, 32, 277

Fabian, A. C., Sanders, J. S., Taylor, G. B., Allen, S. W., Crawford, C. S., Johnstone, R. M., & Iwasawa, K. 2006, MNRAS, 366, 417

Fan, X. 2006, New Astronomy Reviews, 50, 665

Fender, R., et al. 1999, ApJ, 519, L165

Feretti, L., Perley, R., Giovannini, G., & Andernach, H. 1999, A&A, 341, 29

Frenk, C. S., et al. 1999, ApJ, 525, 554

Fryxell, B., et al. 2000, ApJS, 131, 273

Gallo, E., Fender, R. P., & Pooley, G. G. 2003, MNRAS, 344, 60

Gaspari, M., Brighenti, F., D'Ercole, A., & Melioli, C. 2011a, arXiv:1103.5351

Gaspari, M., Melioli, C., Brighenti, F., & D'Ercole, A. 2011b, MNRAS, 411, 349

Guo, F., & Mathews, W. G. 2011, ApJ, 728, 121

Haiman, Z., Mohr, J. J., & Holder, G. P. 2001, ApJ, 553, 545

Haiman, Z., et al. 2005, arXiv:0507013

Hallman, E. J., & Markevitch, M. 2004, ApJ, 610, L81

Hallman, E. J., O'Shea, B. W., Burns, J. O., Norman, M. L., Harkness, R., & Wagner, R. 2007, ApJ, 671, 27

Hansen, S. M., McKay, T. A., Wechsler, R. H., Annis, J., Sheldon, E. S., & Kimball, A. 2005, ApJ, 633, 122

Heitmann, K., Ricker, P. M., Warren, M. S., & Habib, S. 2005, ApJS, 160, 28

Heitmann, K., et al. 2008, Computational Science and Discovery, 1, 015003

High, F. W., et al. 2010, ApJ, 723, 1736

Hincks, A. D., et al. 2010, ApJS, 191, 423

Ho, L. 1999, in Astrophysics and Space Science Library, Vol. 234, Observational Evidence for the Black Holes in the Universe, ed. S. K. Chakrabarti, 157–+

Ho, L. C. 2002, ApJ, 564, 120

Hockney, R. W., & Eastwood, J. W. 1988, Computer simulation using particles

Hopkins, P. F., Hernquist, L., Cox, T. J., Di Matteo, T., Martini, P., Robertson, B., & Springel, V. 2005, ApJ, 630, 705

Hopkins, P. F., & Quataert, E. 2010, MNRAS, 407, 1529

Huang, J., & Greengard, L. 2000, SIAM J. Sci. Comput., 21, 1551

Jeltema, T. E., Hallman, E. J., Burns, J. O., & Motl, P. M. 2008, ApJ, 681, 167

Jenkins, A., Frenk, C. S., White, S. D. M., Colberg, J. M., Cole, S., Evrard, A. E., Couchman, H. M. P., & Yoshida, N. 2001, MNRAS, 321, 372

Jetha, N. N., Ponman, T. J., Hardcastle, M. J., & Croston, J. H. 2007, MNRAS, 376, 193

Jing, Y. P. 2000, ApJ, 535, 30

Jing, Y. P., & Suto, Y. 2002, ApJ, 574, 538

Johnston, D. E., et al. 2007, arXiv:0709.1159

Kaastra, J. S., & Mewe, R. 1993, A&AS, 97, 443

Kaiser, N. 1986, MNRAS, 222, 323

Kasun, S. F., & Evrard, A. E. 2005, ApJ, 629, 781

Kay, S. T., da Silva, A. C., Aghanim, N., Blanchard, A., Liddle, A. R., Puget, J.-L., Sadat, R., & Thomas, P. A. 2007, MNRAS, 377, 317

Kay, S. T., Thomas, P. A., Jenkins, A., & Pearce, F. R. 2004, MNRAS, 355, 1091

Kennicutt, Jr., R. C. 1998, ApJ, 498, 541

Knebe, A., et al. 2011, MNRAS, 819

Koide, S., Shibata, K., & Kudoh, T. 1999, ApJ, 522, 727

Komatsu, E., & Seljak, U. 2001, MNRAS, 327, 1353

Komatsu, E., et al. 2011, ApJS, 192, 18

Kravtsov, A. V., Klypin, A. A., & Khokhlov, A. M. 1997, ApJS, 111, 73

Kravtsov, A. V., Vikhlinin, A., & Nagai, D. 2006, ApJ, 650, 128

Laing, R. A., & Bridle, A. H. 2002, MNRAS, 336, 1161

Laney, C. 1998, Computational Gasdynamics (Cambridge: CUP)

Lau, E. T., Kravtsov, A. V., & Nagai, D. 2009, ApJ, 705, 1129

Lau, E. T., Nagai, D., Kravtsov, A. V., & Zentner, A. R. 2011, ApJ, 734, 93

Levine, E. S., Schulz, A. E., & White, M. 2002, ApJ, 577, 569

Liedahl, D. A., Osterheld, A. L., & Goldstein, W. H. 1995, ApJ, 438, L115

Lima, M., & Hu, W. 2004, Phys. Rev. D, 70, 043504

—. 2005, Phys. Rev. D, 72, 043006

Lin, Y.-T., & Mohr, J. J. 2004, ApJ, 617, 879

Lin, Y.-T., Mohr, J. J., & Stanford, S. A. 2003, ApJ, 591, 749

Lucy, L. B. 1977, AJ, 82, 1013

Lueker, M., et al. 2010, ApJ, 719, 1045

Lukić, Z., Heitmann, K., Habib, S., Bashinsky, S., & Ricker, P. M. 2007, ApJ, 671, 1160

Lukić, Z., Reed, D., Habib, S., & Heitmann, K. 2009, ApJ, 692, 217

MacNeice, P., Olson, K. M., Mobarry, C., de Fainchtein, R., & Packer, C. 2000, Comp. Phys. Comm., 81, 105

Majumdar, S., & Mohr, J. J. 2004, ApJ, 613, 41

Mandelbaum, R., Seljak, U., & Hirata, C. M. 2008, Journal of Cosmology and Astro-Particle Physics, 8, 6

Mantz, A., Allen, S. W., Ebeling, H., & Rapetti, D. 2008, MNRAS, 387, 1179

Mantz, A., Allen, S. W., Ebeling, H., Rapetti, D., & Drlica-Wagner, A. 2010a, MNRAS, 406, 1773

Mantz, A., Allen, S. W., Rapetti, D., & Ebeling, H. 2010b, MNRAS, 406, 1759

Markevitch, M., & Vikhlinin, A. 2007, Phys. Rep., 443, 1

Mathiesen, B. F., & Evrard, A. E. 2001, ApJ, 546, 100

Mazzotta, P., Rasia, E., Borgani, S., Moscardini, L., Dolag, K., & Tormen, G. 2004, arXiv: 0412536

McNamara, B. R., Kazemzadeh, F., Rafferty, D. A., Bîrzan, L., Nulsen, P. E. J., Kirkpatrick, C. C., & Wise, M. W. 2009, ApJ, 698, 594

McNamara, B. R., & Nulsen, P. E. J. 2007, ARA&A, 45, 117

McNamara, B. R., Nulsen, P. E. J., Wise, M. W., Rafferty, D. A., Carilli, C., Sarazin, C. L., & Blanton, E. L. 2005, Nature, 433, 45

McNamara, B. R., Rohanizadegan, M., & Nulsen, P. E. J. 2011, ApJ, 727, 39

Menanteau, F., et al. 2010, ApJ, 723, 1523

Mewe, R., Gronenschild, E. H. B. M., & van den Oord, G. H. J. 1985, A&AS, 62, 197

Mitchell, N. L., McCarthy, I. G., Bower, R. G., Theuns, T., & Crain, R. A. 2009, MNRAS, 395, 180

Mittal, R., Hudson, D. S., Reiprich, T. H., & Clarke, T. 2009, A&A, 501, 835

Mohr, J. J., Evrard, A. E., Fabricant, D. G., & Geller, M. J. 1995, ApJ, 447, 8

Mohr, J. J., Fabricant, D. G., & Geller, M. J. 1993, ApJ, 413, 492

Mohr, J. J., Mathiesen, B., & Evrard, A. E. 1999, ApJ, 517, 627

Motl, P. M., Hallman, E. J., Burns, J. O., & Norman, M. L. 2005, ApJ, 623, L63

Nagai, D. 2006, ApJ, 650, 538

Nagai, D., Kravtsov, A. V., & Vikhlinin, A. 2007a, ApJ, 668, 1

Nagai, D., Vikhlinin, A., & Kravtsov, A. V. 2007b, ApJ, 655, 98

Navarro, J. F., Frenk, C. S., & White, S. D. M. 1995, MNRAS, 275, 720

—. 1996, ApJ, 462, 563

—. 1997, ApJ, 490, 493

Neto, A. F., et al. 2007, MNRAS, 381, 1450

O'Hara, T. B., Mohr, J. J., Bialek, J. J., & Evrard, A. E. 2006, ApJ, 639, 64

Omma, H., Binney, J., Bryan, G., & Slyz, A. 2004, MNRAS, 348, 1105

O'Shea, B. W., Bryan, G., Bordner, J., Norman, M. L., Abel, T., Harkness, R., & Kritsuk, A. 2004, arXiv:0403044

Osmond, J. P. F., & Ponman, T. J. 2004, MNRAS, 350, 1511

Ostriker, J. P., Bode, P., & Babul, A. 2005, ApJ, 634, 964

Parrish, I. J., & Quataert, E. 2008, ApJ, 677, L9

Percival, W. J., et al. 2001, MNRAS, 327, 1297

Perlmutter, S., Turner, M. S., & White, M. 1999, Physical Review Letters, 83, 670

Peterson, J. R., Kahn, S. M., Paerels, F. B. S., Kaastra, J. S., Tamura, T., Bleeker, J. A. M., Ferrigno, C., & Jernigan, J. G. 2003, ApJ, 590, 207

Pfrommer, C., Enßlin, T. A., Springel, V., Jubelgas, M., & Dolag, K. 2007, MNRAS, 378, 385

Pfrommer, C., Springel, V., Enßlin, T. A., & Jubelgas, M. 2006, MNRAS, 367, 113

Pizzolato, F., & Soker, N. 2005, ApJ, 632, 821

Plagge, T., et al. 2010, ApJ, 716, 1118

Ponman, T. J., Sanderson, A. J. R., & Finoguenov, A. 2003, MNRAS, 343, 331

Poole, G. B., Babul, A., McCarthy, I. G., Fardal, M. A., Bildfell, C. J., Quinn, T., & Mahdavi, A. 2007, MNRAS, 380, 437

Poole, G. B., Fardal, M. A., Babul, A., McCarthy, I. G., Quinn, T., & Wadsley, J. 2006, MNRAS, 373, 881

Pope, E. C. D. 2007, MNRAS, 381, 741

Popesso, P., Biviano, A., Böhringer, H., Romaniello, M., & Voges, W. 2005, A&A, 433, 431

Power, C., Nayakshin, S., & King, A. 2011, MNRAS, 412, 269

Pratt, G. W., Croston, J. H., Arnaud, M., & Böhringer, H. 2009, A&A, 498, 361

Press, W. H., & Schechter, P. 1974, ApJ, 187, 425

Press, W. H., Teukolsky, S. A., Vetterling, W. T., & Flannery, B. P. 1992, Numerical Recipes in C (2nd ed.; New York: Cambridge University Press)

Proga, D. 2007, in Astronomical Society of the Pacific Conference Series, Vol. 373, The Central Engine of Active Galactic Nuclei, ed. L. C. Ho & J.-W. Wang, 267–+

Puchwein, E., Sijacki, D., & Springel, V. 2008, ApJ, 687, L53

Randall, S. W., Sarazin, C. L., & Ricker, P. M. 2002, ApJ, 577, 579

Rasia, E., Mazzotta, P., Borgani, S., Moscardini, L., Dolag, K., Tormen, G., Diaferio, A., & Murante, G. 2005, ApJ, 618, L1

Rasia, E., et al. 2006, MNRAS, 369, 2013

Reynolds, C. S., McKernan, B., Fabian, A. C., Stone, J. M., & Vernaleo, J. C. 2005, MNRAS, 357, 242

Ricker, P. M. 2008, ApJS, 176, 293

Ricker, P. M., & Sarazin, C. L. 2001, ApJ, 561, 621

Robinson, K., et al. 2004, ApJ, 601, 621

Rozo, E., et al. 2010, ApJ, 708, 645

Ruszkowski, M., Enßlin, T. A., Brüggen, M., Heinz, S., & Pfrommer, C. 2007, MNRAS, 378, 662

Sanderson, A. J. R., O'Sullivan, E., & Ponman, T. J. 2009, MNRAS, 395, 764

Scannapieco, E., & Brüggen, M. 2008, ApJ, 686, 927

Seljak, U., & Zaldarriaga, M. 1996, ApJ, 469, 437

Shang, C., Crotts, A., & Haiman, Z. 2007, ApJ, 671, 136

Shaw, L. D., Holder, G. P., & Bode, P. 2008, ApJ, 686, 206

Shaw, L. D., Holder, G. P., & Dudley, J. 2010a, ApJ, 716, 281

Shaw, L. D., Nagai, D., Bhattacharya, S., & Lau, E. T. 2010b, ApJ, 725, 1452

Shaw, L. D., Weller, J., Ostriker, J. P., & Bode, P. 2006, ApJ, 646, 815

Sheth, R. K., & Tormen, G. 1999, MNRAS, 308, 119

Sijacki, D., Springel, V., Di Matteo, T., & Hernquist, L. 2007, MNRAS, 380, 877

Sikora, M., Stawarz, Ł., & Lasota, J.-P. 2007, ApJ, 658, 815

Spergel, D. N., et al. 2007, ApJS, 170, 377

Spitzer, L. 1962, Physics of Fully Ionized Gases

Springel, V., et al. 2005, Nature, 435, 629

Stanek, R., Evrard, A. E., Böhringer, H., Schuecker, P., & Nord, B. 2006, ApJ, 648, 956

Stanek, R., Rasia, E., Evrard, A. E., Pearce, F., & Gazzola, L. 2010, ApJ, 715, 1508

Staniszewski, Z., et al. 2009, ApJ, 701, 32

Strang, G. 1968, SIAM J. Numer. Anal., 5, 506

Sunyaev, R. A., & Zeldovich, Y. B. 1972, Comments on Astrophysics and Space Physics, 4, 173

Sutherland, R. S., & Dopita, M. A. 1993, ApJS, 88, 253

Sutter, P. M. 2011, PhD. Thesis

Tinker, J., Kravtsov, A. V., Klypin, A., Abazajian, K., Warren, M., Yepes, G., Gottlöber, S., & Holz, D. E. 2008, ApJ, 688, 709

Trottenberg, U., Oosterlee, C. W., & Schuller, A. 2001, Multigrid (London: Academic Press)

Vanderlinde, K., et al. 2010, ApJ, 722, 1180

Ventimiglia, D. A., Voit, G. M., Donahue, M., & Ameglio, S. 2008, ApJ, 685, 118

Vernaleo, J. C., & Reynolds, C. S. 2007, ApJ, 671, 171

Vikhlinin, A., Kravtsov, A., Forman, W., Jones, C., Markevitch, M., Murray, S. S., & Van Speybroeck, L. 2006, ApJ, 640, 691

Vikhlinin, A., et al. 2009, ApJ, 692, 1060

Voit, G. M. 2005, Reviews of Modern Physics, 77, 207

Voit, G. M., & Bryan, G. L. 2001, Nature, 414, 425

Wadsley, J. W., Veeravalli, G., & Couchman, H. M. P. 2008, MNRAS, 387, 427

Wang, H., Mo, H. J., Jing, Y. P., Yang, X., & Wang, Y. 2011, MNRAS, 413, 1973

Warren, M. S., Quinn, P. J., Salmon, J. K., & Zurek, W. H. 1992, ApJ, 399, 405

Wechsler, R. H., Bullock, J. S., Primack, J. R., Kravtsov, A. V., & Dekel, A. 2002, ApJ, 568, 52

Werner, N., Durret, F., Ohashi, T., Schindler, S., & Wiersma, R. P. C. 2008, Space Science Reviews, 134, 337

White, M., Hernquist, L., & Springel, V. 2002, ApJ, 579, 16

Wik, D. R., Sarazin, C. L., Ricker, P. M., & Randall, S. W. 2008, ApJ, 680, 17

Yang, H.-Y. K., Bhattacharya, S., & Ricker, P. M. 2010, ApJ, 725, 1124

Yang, H.-Y. K., Ricker, P. M., & Sutter, P. M. 2009, ApJ, 699, 315

Zel'Dovich, Y. B. 1970, A&A, 5, 84

Zhao, D. H., Mo, H. J., Jing, Y. P., & Börner, G. 2003, MNRAS, 339, 12

Zu Hone, J. A., Ricker, P. M., Lamb, D. Q., & Yang, H.-Y. K. 2009, ApJ, 699, 1004